Analysis of Vortex-Lifting Surface Interactions

Alasdair D. Thom

A thesis submitted for the degree of

Doctor of Philosophy

School of Engineering

College of Science and Engineering

University of Glasgow

August 2011

Abstract

The interaction of a vortex with a lifting surface occurs in many aerodynamic systems, and can induce significant airloads and radiate impulsive noise. Yet due to their complex nature, the ability to accurately model the important flow physics and noise radiation characteristics of these interactions in realistic situations has remained elusive. This work examines two cases of vortex-lifting surface interactions by enhancing the capabilities of a high fidelity flow solver. This flow solver utilises high spatial discretisation accuracy with a 5^{th} order accurate WENO scheme, and overset meshes to accurately resolve the formation, evolution and interaction of a tip vortex using an inviscid approximation of the fluid.

An existing computational infrastructure is further developed and applied to analyse blade-vortex interactions that occur on a helicopter rotor. An idealised interaction is studied, where an independently generated vortex interacts with a rotor. It is found that through the employment of adequate spatial and temporal resolution, the current methodology is capable of resolving the important details of the interaction over a range of vortex-blade miss distances. A careful study of the spatial and temporal resolution requirements is conducted to ensure that the computed results converge to the correct physical solution. It is also demonstrated that a linear acoustic analysis can accurately predict the acoustic energy propagated from these interactions to the far-field, provided the blade surface pressures are accurately computed.

The methodology is then used to study an idealised propeller wake-wing interaction, which occur behind a tractor mounted turboprop. A computationally efficient method of modelling the wake-wing interaction is developed and the computed surface pressures of the interaction are confirmed to agree well with the experimental data. The analysis is coupled to an optimisation algorithm to determine a novel wing design, and it is found that significant drag reductions can be achieved with small changes in the twist distribution of the wing.

This work confirms that by using a combination of strategies including efficient grids, high order accurate numerical discretisations and a flexible software infrastructure, high fidelity methods can indeed be used to accurately resolve practical cases of vortex-lifting surface interactions in detail while being feasible in a design setting. The

airloads and aeroacoustics from these interactions can be accurately predicted, thus confirming that with the modern advances in computing and algorithms, high fidelity methodologies such as those presented in this thesis are in a position to be used to gain a deep understanding of the relevant flow physics and noise radiation patterns, and their impact on aircraft design.

Declaration

I declare that all the work that is contained within this dissertation has been undertaken by the author.

Signed: .....

Name: .....

Date: .....

Acknowledgements

I would like to acknowledge the help and support of my supervisor, Professor Karthik Duraisamy, who provided continuous support and guidance throughout this project. I would also like to thank Dr Marco Vezza, Dr Emmanuel Benard and Professor Richard Brown for their role in my academic supervision.

In addition, I would like to thank all the members of the Rotorcraft Aeromechanics Laboratory that I worked with. Thanks should also go the Aerospace Design Laboratory at Stanford University, for welcoming me into the group, helping me with the optimisation algorithm, and for introducing me to Frisbee golf.

Finally, I would like to thank my friends and family. Particularly Hazel Morrison, and my parents Linda and William Thom.

Contents

List of Tables

List of Figures

Nomenclature

A	Wing area
C_D	Coefficient of drag = $\frac{drag}{\frac{1}{2}\rho U_\infty^2 A}$
C_L	Coefficient of lift = $\frac{lift}{\frac{1}{2}\rho U_\infty^2 A}$
C_P	Coefficient of pressure = $\frac{p-p_\infty}{\frac{1}{2}\rho U_\infty^2}$
C_T	Propeller coefficient of thrust = $\frac{thrust}{\rho n^2 16 R^4}$
C_d	Sectional coefficient of drag = $\frac{sectional\ drag}{\frac{1}{2}\rho U_\infty^2 c}$
C_l	Sectional coefficient of lift = $\frac{sectional\ lift}{\frac{1}{2}\rho U_\infty^2 c}$
J	Propeller advance ratio = $\frac{U_\infty}{2Rn}$
M	Mach number
R	Rotor radius
Γ	Vortex Circulation
μ	Helicopter advance ratio=$\frac{U_\infty}{U_{Tip}}$
ν	Kinematic viscosity
ψ	Azimuth location
ρ	Density
τ	Pseudo time

$\xi, \eta, \zeta.$	Computational space Cartesian directions
a	Speed of sound
b	Semi-span of wing
c	Chord
e	Total energy per unit volume
i, j, k	Cell indices
n	Propeller revolutions per second
p	Pressure
r	Radial location
r_c	Vortex core radius
t	Time
u, v, w	Velocity in physical Cartesian directions
v_n	Normal velocity
x, y, z	Physical space Cartesian directions

Subscripts

∞	Freestream condition
θ	Swirl condition
eqv	Equivalent azimuth
p	Propeller
tip	Rotor tip condition
v	Vortex
VG	Vortex generator

Acronyms

AVI	Aerofoil-Vortex Interaction
$BDF2$	Second order accurate backward differencing time integration
BE	First order accurate backward Euler time integration
BVI	Blade-Vortex Interaction
CFD	Computational fluid dynamics
CFL	Courant-Friedrichs-Lewy number
dB	Decibel
SPL	Sound pressure level
$WENO$	Weighted essentially non-oscillatory

Chapter 1

Introduction

Over the past 100 years, aircraft design has advanced such that aeronautics and aviation now play a major role in the modern world and are integral to the global economy. Historically, aircraft designers have been successful in driving down fuel burn for economic reasons but designers now face additional challenges. An indication of the current direction of the aviation industry is given in a report published by the European Commission in 2001, *European Aeronautics : A Vision for 2020* [1]. This report laid out a series of research objectives that were aimed at maintaining the competitive position of European civil aircraft manufacturers on the global market. These objectives covered a broad range of topics such as aircraft quality, affordability and safety, and airport management. Additionally, it highlighted that there should be an increased emphasis on the "environmental impact" of the aviation industry, which includes reductions in CO_2 emissions and the perceived noise of an aircraft, setting the the ambitious goal of cutting both of these by 50% by the year 2020. A consequence of this report was the formation of the Advisory Council for Aeronautics Research in Europe (ACARE), where the same environmental research objectives have been maintained in addition to further goals outlined for 2050 [2, 3]. The perceived noise and emissions of an aircraft are largely determined by its propulsion system. For instance, a major source of helicopter aeroacoustic noise originates from the main rotor, and future rotorcraft could potentially alleviate this through advanced rotor design. For

fixed wing aircraft, both noise and fuel efficiency are largely determined by the aircraft engine, and new concepts such as open rotor design could offer significant benefits over current technology.

The design and implementation of novel technology is challenging and will require a combination of technical advances in many areas, as the problem is inherently multi-disciplinary. The ability to accurately model the pertinent aerodynamics is of great importance for this process, as accurate modelling not only helps proper exploration of the design space, but it can also reduce the dependency on relatively expensive flight testing. Traditionally, lower fidelity models such as lifting line/surface theory, or empirical models have commonly been used in the design process. The simplicity and ease of use of these lower order models means that they have seen, and will continue to see, widespread use for aerodynamic design analysis. However, this simplicity comes at the cost of a limitation to their utility. There are invariably design scenarios where the predictions made by these lower fidelity models are not of sufficient accuracy, or cases that are simply too complex for these models to be useful. As a result of this, lower fidelity models could potentially miss the favourable regions in the design space. For these instances, newer and more accurate modelling methods must be sought.

The interaction of vortices with a lifting surface is a prime example of a complex flow where lower order methods could be inaccurate, especially when the vortices impinge on the lifting surface. Vortex-lifting surface interactions occur in many aerodynamic systems such as turboprops, helicopters and vertical axis wind turbines as illustrated in Fig. 1.1. These interactions are of considerable importance to their operation, yet the ability to accurately predict them at the design stage remains elusive.

Vortices arise in many flow regimes [4], but the type of vortex-lifting surface interactions which are of a practical engineering interest in aircraft design typically involve trailing tip vortices which are formed behind the tip of a finite wing. The formation of these vortices can be understood by first considering the generation of lift by an aerofoil. The Kutta-Joukowski theorem states that the lifting force experience by an aerofoil in a uniform flow is equal to the product of the fluid density, the freestream velocity, and the circulation around the aerofoil [5]. This circulation around the aerofoil

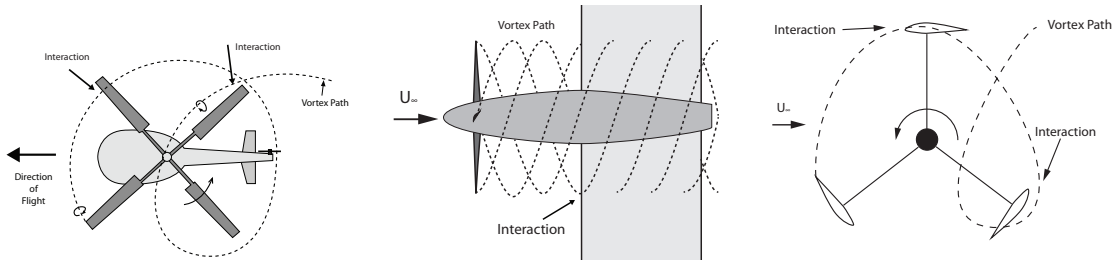

(a) *The main rotor of a helicopter.* (b) *Tractor mounted turboprop.* (c) *Vertical axis wind turbine.*

Figure 1.1: *Examples of vortex-lifting surface interactions*

is a consequence of the viscosity of the fluid and can be represented by a *bound vortex*, which is not attached to any fluid particles but is bound to the aerofoil.

When this description of lift generation is extended to a finite wing, the bound vortex is located across the wingspan. In general, the local lift of the wing will vary across the wingspan, reducing to zero at the wing tips, therefore the strength of the bound vortex will also vary across the wingspan. Helmholtz' vortex theorems state that vortex filaments cannot end in space [5], and so a trailing vortex sheet is formed behind the wing. The local strength of the vorticity in this trailing vortex sheet is proportional to the local change in the circulation strength of the bound vortex:

$$d\Gamma_t(y) = \left(\frac{d\Gamma_w(y)}{dy}\right) dy \tag{1.1}$$

Where $\Gamma_w(y)$ and $\Gamma_t(y)$ are the local bound vortex circulation and trailing vortex sheet circulation respectively, and y is the wingspan coordinate. A wing typically has large gradients of bound circulation close to the wing tips, especially for helicopter rotors and propellers where the local velocity is proportional to the radial location, producing a high concentration of circulation at the edge of the trailed vortex sheet. As the trailing vortex sheet moved downstream of the wing, its edges will roll up to form a pair of tip vortices.

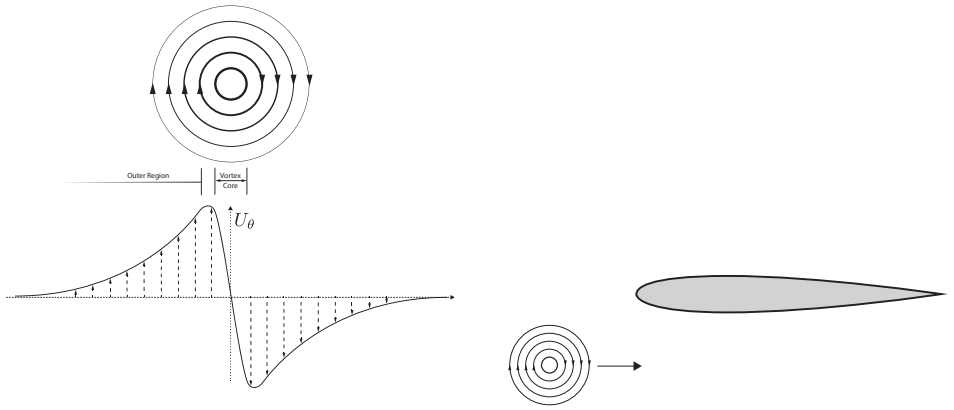

(a) *Typical vortex swirl velocity.* (b) *2D vortex-aerofoil interaction*

Figure 1.2: *Two dimensional aerofoil-vortex interaction*

The structure of a simple symmetric vortex is depicted in Fig. 1.2(a), where the swirl velocity profile is shown. While a real tip vortex will not necessarily have such a well defined symmetric structure, this diagram represents its basic structure, and shows its two distinct regions. At the inner part is the core region, where the velocity is proportional to the radial distance from the vortex centre. In this core region, the flow undergoes near solid body rotation, and the majority of the vorticity is contained in this region. In the outer region of the vortex, the flow is largely irrotational as the velocity decays approximately as the inverse of the radial distance. Between these two sections, there is a transition between the solid body rotation at the vortex core and the outer irrotational flow.

A tip vortex that is trailed from a helicopter or propeller rotor blade will eventually dissipate due to the viscous effects of the fluid, however it can typically take hundreds of chord lengths of vortex convection to dissipate its rotational energy. Vortices can therefore persist in the flow and interact with a lifting surface inducing unsteady loads. To illustrate the fundamental effect of a vortex on a lifting surface, consider the two dimensional case where a vortex passes below an aerofoil, as illustrated in Fig. 1.2(b). To simplify the case, let the vortex pass at a distance below the aerofoil such that its structure and strength remain unchanged during the interaction. The aerofoil has zero steady angle of attack but as the vortex passes an unsteady lift is induced.

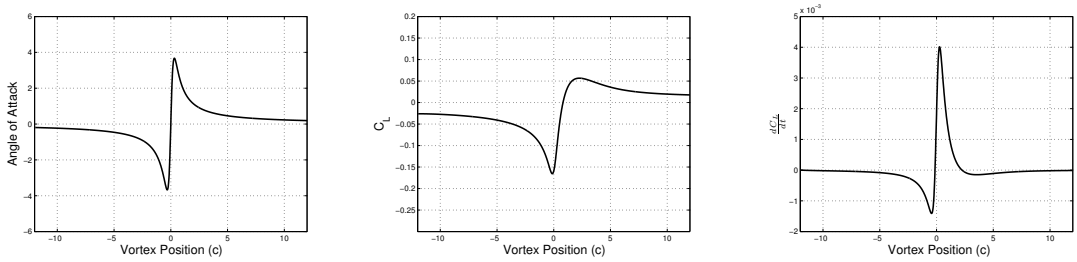

(a) *Angle of attack induced from vortex* (b) C_L *of aerofoil* (c) $\frac{dC_L}{dt}$ *of aerofoil*

Figure 1.3: *Two dimensional aerofoil-vortex interaction*

The angle of attack that the vortex induces on the aerofoil is shown in Fig. 1.3(a). The vortex position relative to the aerofoil is shown in the *x-axis* as the vortex moves in the positive direction. Initially, a negative angle of attack is induced due to the sense of rotation of the vortex. As the vortex approaches the aerofoil, the angle of attack continues to decrease until the vortex passes below its leading edge, where there is a rapid change in angle of attack to its maximum positive value. This decays as the vortex convects further downstream.

The lift of the aerofoil is shown in Fig. 1.3(b). This is similar in distribution to the induced angle of attack, with the additional effect of the shed wake from the aerofoil. This shed wake is the consequence of a change in circulation, and its influence on the lift of an aerofoil is typically an effective delay in the load [6]. Also shown is the change in lift with respect to time in Fig. 1.3(c), which illustrates the impulsive nature of an interaction. This change in lift is important as the far-field noise radiated from an interaction is strongly influenced by this.

The above case is a two dimensional idealisation of a vortex-lifting surface interaction, and corresponds to a case where a straight vortex is parallel to the wing it interacts with. In practical situations, the interactions are seldom completely parallel, as vortices tend to be part of a complex, highly three-dimensional wake system. In addition, when a vortex interacts closely with a lifting surface, its structure is severely altered, especially if the lifting surface passes through the vortex core. The formation and convection of the tip vortex is also difficult to predict and this is especially true

for a helicopter rotor where the path of the tip vortex is highly complex.

A greater insight into vortex-lifting surface interactions can be gained by using high fidelity modelling methods such as computational fluid dynamic models (CFD). In general however, CFD models are difficult to used in practical aircraft design. One reason for this is the relatively high computational costs associated with these models, but as computers become more powerful, and CFD models become more efficient, these computations become more feasible. More fundamentally, there can be a high level of uncertainty in the results that a CFD model produces for complex practical problems. As noted extensively by Hirsch [7], there are many possible sources of error in a CFD solver, such as:

- **Numerical or Discretisation Error:** Errors arising from the space and time discretisation.
- **Convergence Error:** Errors arising from the numerical solution not being full converged for the finite number of mesh point that are used.
- **Round Off Error:** Errors arising from the limited machine accuracy available for representing a numerical value on a computer.
- **Model Uncertainties:** Errors arising from the models used to describe complex flow properties such as turbulence, combustion and multiphase flows.

Additionally, practical problems will usually be multi-disciplinary where additional analysis, such as the structure dynamics of the aircraft, needs to be performed simultaneously, further increasing the complexity.

There is, therefore, a need to test these high fidelity aerodynamic models against problems for which they can be extensively and rigorously validated. This can be achieved by studying idealised problems where the essential physics of the problem are represented in a simplified manner allowing the fidelity of the model to be assessed. While CFD solvers can be adapted to model a range of flows, from inviscid models

to direct numerical simulations of turbulence, it is essential to isolate phenomena that are of engineering relevance and select appropriate modelling strategies to suit one's needs.

This thesis will develop and apply a high fidelity CFD solver to analyse two distinct vortex-lifting surface interaction problems: blade-vortex interactions which occur on a helicopter rotor, and propeller-wing interactions which occur behind a tractor mounted turboprop. These cases were chosen as they represent two very relevant problems that are faced by modern aircraft designers. Previous analysis has shown that lower order modelling methods are not capable of accurately resolving all the essential flow phenomena for these problems, necessitating the application of higher fidelity methods. The problems will be studied in a sub-system framework, thus allowing the modelling approach to be rigorously compared to experimental data

The consequence of this work is to assess if these high fidelity models are capable of accurately modelling the salient physics of a vortex-lifting surface interaction for the problems considered. If confidence is to be gained in these methods, validation studies such at this must be performed. In addition, this work will assess the use of these models coupled with an optimisation algorithm for a specific case. This illustrates the possible utility of these high fidelity methods in a practical design problem. A brief discussion of the two types of interactions considered in this study follows.

1.1 Blade-Vortex Interaction

Blade-vortex interactions (BVIs) are a major source of helicopter aerodynamic noise and arise due to interactions between the rotor wake and the rotor blades. This phenomenon is illustrated in Fig. 1.4 where the wake from a helicopter rotor is shown. A typical tip vortex path is shown in Fig. 1.4(a), where the tip vortices trailed from the helicopter rotor blades will naturally convect backward into a position where they could interact with the rotor blades. In low speed level cruise conditions, these vortices are typically pushed below the rotor plane because of the strong inflow of the rotor.

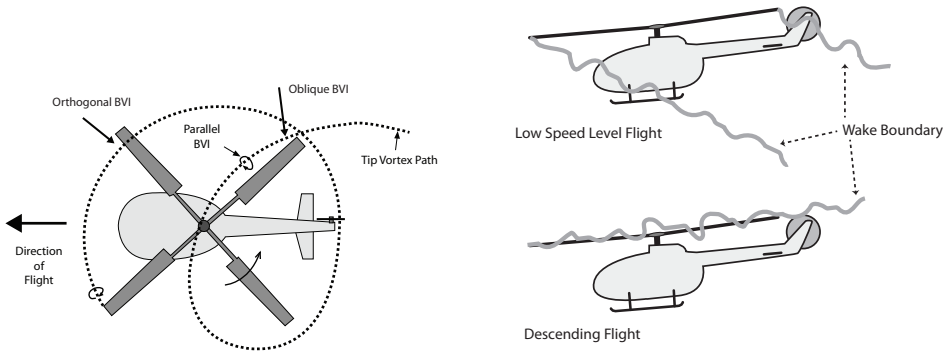

(a) *Top view of tip vortex path from helicopter blades*

(b) *Rotor wake in normal and descending flight.*

Figure 1.4: *BVI occurrence on a helicopter rotor.*

However, certain flight conditions, such as descent or high speed forward flight, or the occurrence of an upward gust can cause the vortices to convect into the rotor plane or very close to the rotor blades, as shown in Fig. 1.4(b).

When the vortices pass close to the rotor blades, blade-vortex interactions occur, inducing rapid changes of lift on the blades and radiating strong acoustic waves from the rotor. The complex geometry of the rotor wake will produce different types of BVIs as the vortices and blade interact at different angles, vertical miss distances and speeds. Orthogonal, oblique and parallel interactions are labelled in Fig. 1.4(a). These are shown here on the advancing side of the rotor, but can also occur on the retreating side. BVI can also arise on tandem rotor helicopter where the wake of one rotor interacts with the blades of the other rotor.

The interaction that will produce the strongest acoustic pulse is one in which the vortex and the blade are near-parallel, with zero vertical miss distance between them. This will produce the largest and most impulsive change in lift, which could occur simultaneously over a large span of the rotor blade. As a result of this impulsive lift change, the strongest acoustic waves are radiated from a parallel BVI [8]. Unlike other forms of aerodynamic noise, such as thickness or high-speed impulsive noise, BVI noise will radiate largely out of plane of the rotor and towards the ground. The noise also

typically occurs in a frequency range which is of particular annoyance to the human ear.

BVIs have been the subject of much research over the past five decades. The following section briefly summarises some important experimental and computational studies.

1.1.1 Experimental Studies

Among the first to study the generation of BVI noise were Leverton and Taylor [9] in 1966, when aircraft annoyance and detection became a prominent issue. This issue was referred to as "Blade-Slap" due to the slap like sound generated by a BVI. The study recreated the interaction by using two jets, positioned above and below a rotor, to approximate the effect of the vortex. They concluded that the slapping noise was most probably caused by the rotor blades passing through the tip vortex structures of the rotor wake.

In-flight measurements of impulsive noise were first made by Schmitz and Boxwell [10, 11]. In this study, a "quiet aircraft" flew in formation with a helicopter. Noise measurements were obtained for various descent and forward flight speeds, both of which were seen to significantly alter the level of BVI noise generated from the helicopter rotor. This variation is largely due to the change in the position of the wake system of the helicopter with respect to the rotor for various flight regimes. The study compared the in-flight measurements to wind tunnel data and showed that the data could be compared favourably, provided the advance ratio, rotor thrust coefficient and tip Mach number were matched.

A recent and prominent example of an experimental study in BVI on a scaled rotor is the Higher Harmonic Control Aeroacoustics Rotor Test (HART) research programme [12, 13, 14] conducted by researchers from the German Aerospace Center (DLR), the French Office National dEtudes et de Recherches Aerospatiales (ONERA), the German-

Dutch wind tunnel (DNW), NASA, and the U.S. Army Aeroflightdynamics Directorate (AFDD). Two HART research programmes were conducted with the aim of increasing the basic understanding of noise generation by rotor blade-vortex interactions and to provide data against which analytic models could be compared. The tests were performed in an anechoic wind tunnel, allowing accurate measurement of acoustics as well as the surface pressures on the rotor blades. In addition, the wake of the rotor was also measured using laser Doppler velocimetry and later the more sophisticated particle image velocimetry, allowing the position of the vortex to be determined.

These studies are useful to understand the occurrence of BVI on a helicopter rotor, but the fundamental aspects of the interaction are often lost in the complexity of the experiment. For instance, the position of the rotor blade in relation to the wake will greatly affect the characteristics of the interaction. The full rotor experiments have a large uncertainty about the position of the rotor wake and the tip vortices during the interaction. In addition, the blade deflections can be large, so the complex aeroelastic response of the blade must also be considered. These complexities make comparisons between experimental data and computational methods difficult, especially when the fidelity of the numerical method is under question.

Some experimental studies therefore focused on idealised BVIs with the hope of gaining a more fundamental insight into the interaction, and also producing experimental data that can be used to rigorously evaluate analytic methods. The work of Lee and Bershader [15] is an experimental study which attempted to reduce the interaction to a two dimensional aerofoil-vortex interaction (AVI), which is an idealised case of a blade interacting with a parallel vortex. This two dimensional experiment was performed by placing an aerofoil at an angle of attack of 30° in a shock tube. The starting vortex generated from this aerofoil convected downstream and interacted with a target aerofoil. This approach revealed the intricate details of the flow as the vortex collides with the leading edge of the aerofoil. For instance, the interaction can induce a small region of separated flow at the leading edge of the aerofoil with opposite vorticity to the interacting vortex. These experiments also provided surface pressure measurements during the interaction for comparison with analytic methods.

Another idealised experimental approach is the "free vortex" method, where an independently generated vortex interacts with the rotor. This allows the properties of the vortex, such as its position, strength and size, to be well determined. These parameters can be adjusted by controlling the position and angle of attack of the vortex generator. The first to use this approach was the work of Surendraiah [16], where the independent vortex is generated upstream and interacts with the rotor at 180° azimuth, to create a near parallel interaction.

This approach has been replicated, such as in the work of Horner *et al.* [17] where the vortex generator was comprised of a split-wing, allowing for better control of the vortex position. The most extensive work using the free vortex approach was performed by Kitaplioglu and Caradonna [18, 19]. The experimental work was performed in connection with the detailed experiments of McAlister *et al.* [20], which studied the structure of a vortex trailed from a NACA 0015 wing. There was therefore a high level of confidence in the properties of the vortex involved in the interaction. The rotor was fitted with spanwise pressure transducers to obtain surface pressure data at various radial locations and the experiment was performed in an $80ft \times 120ft$ acoustically treated wind tunnel. This allowed detailed acoustic data of the interaction to be taken, and acoustic data was obtained in the near-field and the far-field of the interaction. This study provided invaluable data for the validation of analytic methods.

1.1.2 Computational Studies

The computation of the forces generated during a BVI has been an active area of research since the 1970s. The first to compute the unsteady lift distribution was Widnall [21] where linear unsteady aerodynamic theory and an oblique gust model was used to analyse a typical BVI occurring on a helicopter rotor. Since then, various levels of complexity have been used to analyse the aerodynamics of BVI, including indicial methods [22, 23], and full potential methods [24, 25].

As digital computers and numerical algorithms have advanced, the application

of Euler/Navier-Stokes computational fluid dynamic (CFD) solvers has become the prominent approach to model BVIs. The first studies began in the mid to late 1980s when Srinivasan *et al.* [26] and Baeder [27] applied the "vortex fitting" or "prescribed vortex" method to model a two dimensional aerofoil-vortex interaction (AVI), and this method was later extended to model BVI [28]. This approach involved prescribing the effect of the vortex in the flow, the structure and strength of which is obtained empirically. These studies showed that the "vortex fitting" approach can successfully model cases of BVI where the vortex misses the blade. As this method imposes the effect of the vortex, its structure does not decay due to numerical dissipation. The disadvantage of this approach is that a case where the interaction changes the vortex structure cannot be accurately modelled, such as when the vortex passes close to the blade. It is also not easily extended to practical rotor simulations, but is nevertheless a good validation tool.

A vortex can be initiated in the CFD solution as a perturbation in the flow. For an AVI simulation, the vortex is initiated upstream and is then allowed to freely convect and interact with the aerofoil. This method is capable of accurately simulating strong interactions where the vortex is bisected by the blade, but the solver must be capable of preserving the vortex structure with minimal numerical dissipation. Vorticity confinement, where the vortical structures are explicitly preserved against numerical dissipation through an additional term in the governing equations, was used by Morvant *et al.* [29, 30]. Promising results were obtained on relatively coarse meshes, however vorticity confinement is not a mature technology, especially because it requires the specification of empirical confinement parameters. Dynamic mesh clustering has also be used to counter the inherent decay of the vortex structure [31, 32], but this method can be complex to implement, especially if extended to realistic rotor configurations.

Some studies have attempted to simulate realistic rotors undergoing BVI. A prime example is the work of Lim *et al.* [33] and Lim and Strawn [34] where the experimental data from the HART test programme was simulated. This approach cycled information between a CFD flow solver and a closely coupled structural analysis code in an attempt to fully model the aeroelastic response of the rotor blade during BVI. This ambitious study showed promising results, yet largely under-predicted the BVI airloads. This

was attributed to numerical dissipation of the tip vortices in the wake of the rotor, which reduced the subsequent interaction strength.

A study which attempted to counter this numerical diffusion was performed by Kelly [35]. In this work, the vorticity transport equations are solved using a highly compressive flux limiter and a lifting line type model was used as a vorticity source at the rotor blades. This approach can preserve the tip vortices for many rotor revolutions and was shown to accurately recreate the blade forces for certain types of BVI regimes. However, the linear representation of blade aerodynamics means that the interactions where the vortex passes close to the blade cannot be accurately modelled.

1.2 Propeller Wake-Wing Interactions

Since the late 1980s, Turbofan engines have been the preferred propulsion choice for regional aircraft. Turbofan engines offered a faster and quieter alternative to the turboprop, and over the last two decades the use of turboprop engines has declined. However, the trend of rising oil prices and growing environmental concerns has brought increasing emphasis on the fuel efficiency of an aircraft. This has spurred renewed interest in the use of turboprop engines for use in short to medium range transport and cargo aircraft, as turboprop engines offer greater fuel efficiency over turbofans.

Turboprop propulsion is typically used with low speed transport and small commuter aircraft, but currently research is being conducted into the "advanced turboprop" or "open rotor" design [36]. These designs are essentially turboprops intended for medium to large transport aircraft, which operate at Mach numbers typical of a turbofan. The performance of the advanced turboprop design approaches that of a turbofan but with the fuel savings typically associated with the turboprop. Research towards this design was initially conducted in the 1970s when the international energy crisis saw a sudden dramatic rise in the price of oil. As the price of oil dropped, these research projects were abandoned, but have now been restarted by companies such as Rolls-Royce and General Electric [37]. This new generation of turboprop designs are

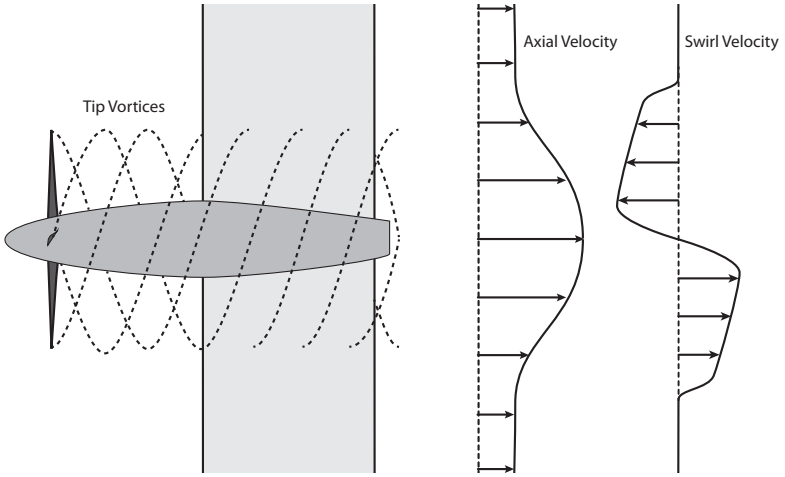

Figure 1.5: *The wake of a propeller impacting on a wing. Shown are typical time-averaged swirl and axial velocities.*

estimated to have as much as a $25\% - 30\%$ improvement in fuel efficiency over conventional turboprops and a reduced acoustic footprint. One issue that is still subject to ongoing research is the integration of these turboprops with the airframe.

A turboprop aircraft is commonly constructed in a tractor configuration, where the propeller is mounted in front of the wing. In this configuration, the wing is immersed in the wake of the propeller producing a propeller-wing interaction. To achieve high cruise speeds, a propeller is typically highly loaded, producing a wake that is dominated by strong tip vortices trailed from the tips of the propeller blades. The wake is characterised by an increase in axial and swirl velocity which is illustrated in Fig. 1.5. The axial and swirl velocities of the propeller wake are comparable in magnitude to the freestream velocity and will convect downstream where they will impact on the wing. This interaction induces a considerable variation in the lift and drag distribution across the wingspan compared to a "clean" wing subject to just freestream conditions. This distortion of the lift and drag has been the subject of much research over the past five decades and an optimal integration of the turboprop and the airframe is ultimately sought.

1.2.1 Previous Work

Among the first to examine this interaction was Jameson [38] for V/STOL aircraft where the propeller slipstream is deflected by the wing to increase the lift at takeoff. Since then various studies have taken different approaches to modelling the propeller wake in their analysis. For instance Miranda *et al.* [39] used a vortex tube model of the propeller slipstream where the influence of the wing on the slipstream was not accounted for. The loads on the wing were subsequently calculated using lifting line theory. Cho and Cho [40] used a more complex vortex lattice representation of the propeller wake and calculated the loads on the wing using a panel method. These studies generally show good agreement with experimental data for certain configurations, but are ultimately limited by the simple representation of the aerodynamics. For instance, the study by Cho and Cho gave poor results when examining propellers at low advance ratios.

The application of Euler/Navier-Stokes CFD analysis to propeller-wing interactions has the potential of resolving all the important flow features of the interaction yet there has been limited research in this area. A prominent study was conducted by Lötstedt [41], where an Euler solver was used to analyse the interaction. In this work, the effect of the propeller was approximated by an actuator disc model that was imposed in the flow as body forces in the momentum equations. This approach greatly simplified the computation, as the complex unsteady flow in the wake of the propeller was not computed. The study showed encouraging comparisons to experimental data, however, there were notable discrepancies. For instance, the wake predicted by the actuator disc model showed large variations from the experimental data, especially in the region at the edge of the wake. This was attributed to the actuator disc model not adequately accounting for the complex flow associated with the tip vortices trailed from the propeller blades. The numerical scheme also used central differencing for the inviscid fluxes where an artificial viscosity had to be prescribed to achieve numerical stability. The wake structure of the propeller was shown to be highly sensitive to the value of the artificial viscosity.

Full CFD studies where the propeller wake is fully resolved are difficult due to the complexity of the problem and the potential computational expense in resolving the wake formation and interaction. Early work performed by Stuermer [42] in 2006 showed promising results, and more recently a study was conducted by Roosenboom *et al.* [43] in 2010. Here, a comparison of particle image velocimetry (PIV) experimental data and CFD computations of the propeller wake as it interacts with a wing were presented. The PIV results revealed the intricate details of the propeller wake as it passed over the wing, and the CFD computations were in good qualitative agreement with this data. However, the study concluded that a major deficit of the CFD computations was numerical diffusion which largely dissipated the vortical flow features. This diffusion occurred even with an inviscid modelling of the flow, despite very fine spatial resolution across the vortex core and fine temporal resolution.

Another experimental study of propeller-wing interactions that was performed primarily to provide data for the validation of computational methods was conducted by Samuelsson [44, 45, 46]. This experiment was performed in the late 1980s by the former FFA, the aeronautical research institute of Sweden, and the results are part of an AGARD report of CFD test cases. The study investigated an idealised experimental setup, in which a propeller was mounted in the centre of an isolated wing. Time-averaged velocity data of the wake of the propeller was obtained for an isolated propeller as well as a case with the wing mounted downstream. For the case with the downstream mounted wing, surface pressure data was taken on the surface of the wing across the region of interaction. The relatively simple setup of this experiment and the data obtained make this ideal for the validation of computational models.

For turboprops mounted in tractor configuration, the section of the wing that is immersed in its wake will experience an increase in axial velocity and either an upwash or downwash depending on its position and the sense of the propeller rotation. It is the combination of this axial and swirl velocity that influences the circulation distribution across the wingspan and its effect can be seen by considering a wing section immersed in either the upwash or downwash region of the wake, as shown in Fig. 1.6. The upwash region increases the local incidence of the oncoming flow to the wing, altering both the magnitude and direction of the local lifting force. The lifting force increases

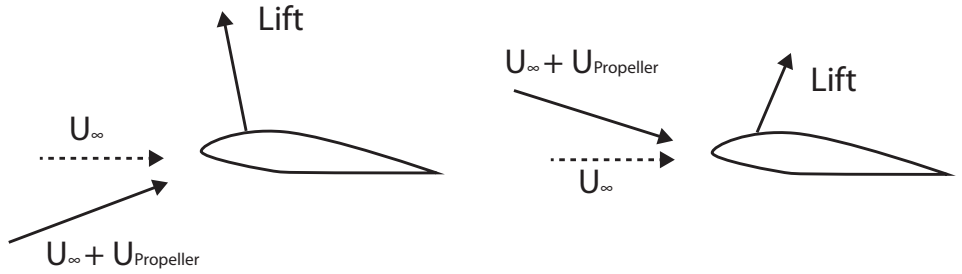

(a) *Wing immersed in propeller upwash region.*

(b) *Wing immersed in propeller downwash region.*

Figure 1.6: *Sectional lift induced by propeller wake.*

and is rotated forward, reducing the sectional drag. In some cases, this vector can be altered such that it faces into the freestream, producing a local thrust on the wing. The downwash region has an opposite effect where the incidence of the wing is decreased and the lifting vector is rotated backward. These effects are coupled to the downwash produced by the wake of the wing.

The design of an optimal wing which accounts for the effects of the propeller wake was first examined by Kroo [47]. This study attempted to calculate the optimal spanwise circulation distribution of the wing to minimise the induced drag for a given lift. This approach involved an extension to lifting line theory to incorporate the influence of the propeller as an interference term. The circulation that produced the minimum induced drag was then determined explicitly using a Lagrangian method. The resulting optimal circulation distribution across the wingspan differs markedly from the classic elliptical loading result of a "clean" wing. The optimally loaded wing acts somewhat like a stator vane in a turbine that recovers some of the rotational energy from the slipstream and reducing the induced drag of the wing. More recently, a similar analysis has been performed by Veldhuis [48], and these studies show the potential benefits of modifying the wing lift distribution. Both these studies concluded that an inboard-up propeller rotation produced the optimal circulation distribution. This is due to the favourable effect of the upwash of the propeller wake being maximised as, in general, the inboard section of the wing has a higher circulation distribution. Outboard up

propeller rotation has less favourable results.

Some studies [39, 49] have examined the effect of propeller spanwise position on the wing. In general, positioning an inboard-up rotating propeller further outboard has a positive effect on reducing the induced drag for a given lift. However, positioning the propellers outboard is undesirable in practical design due to the increased yaw moment generated during single engine flight.

1.3 Objectives

The accurate prediction of vortex-lifting surface interactions is very challenging due to the many complexities previously noted, particularly those associated with the accurate resolution of vortical structures. Computational Fluid Dynamics (CFD) models solve numerically the governing conservation equations of fluid flow and perhaps offer the most rigorous approach to analysing vortex-lifting surface interactions, since the underlying physics is encapsulated within the governing equations themselves. The use of CFD models has been steadily growing as digital computers become more powerful and accessible, and, as previously noted, these models have been applied to the analysis of vortex-lifting surface interactions. CFD models potentially offer significantly more insight and detail when used to analyse these interactions, however for these models to gain widespread acceptance and be of use within a design setting, they must be computationally efficient and be rigorously validated against experimental data.

A common theme among the previous applications of CFD solvers in the analysis of vortex-lifting surface interactions is the inherent numerical dissipation of the vortical structures that leads to inaccurate predictions. There have been many studies of vortex-lifting surface interactions where different novel methods are used to counter this dissipation [30, 31, 35], but there is no clear indication if any will gain widespread use. There is therefore still a need for more research involving CFD methods with the ultimate aim of obtaining an efficient and accurate method of modelling these interactions that can be applied to practical computations and aircraft design.

Recently, high fidelity CFD methods have been successfully used to study tip vortex formation [50, 51, 52]. Through the use of high spatial accuracy and high quality meshes, the numerical dissipation can be sufficiently reduced to accurately compute tip vortices in the solution domain. The tip vortex formation can be accurately resolved, and its structure preserved in the solution over many chord lengths of convection.

The primary aim of this thesis is to develop and assess the application of these high fidelity methods to the analysis of two problems of vortex-lifting surface interactions. These problems are studied in an idealised framework, where the essential physics are represented in a simplified environment. This allows the methodology to be rigorously validated against experimental data and will indicate if this approach is capable of accurately resolving all the important physics of the problem.

Initially, blade-vortex interaction that occurs on helicopter rotors is studied. Many recent studies have focused on resolving a full scale rotor undergoing self-induced induced BVI, but have in general underpredicted the magnitude of the interaction. The present study will therefore attempt to fully resolve an interaction, but in an idealised framework. This framework represents all the important flow physics of the real problem, but will allow the ability of the current methodology to resolve this interaction to be carefully assessed. The acoustic energy radiated from a BVI is a major source of helicopter aeroacoustic noise, and the accurate prediction of this noise, especially in the far-field, is important for the design of quiet rotors. The ability of a linear acoustic analysis to predict this noise using the computed blade surface pressures is also assessed.

The current methodology is then used to study the interaction of a turboprop wake with a wing. Previous studies have shown little emphasis on computing the details of the wake structure and tip vortices during these interactions. Studies that have resolved the wake structure have in general suffered from large numerical diffusion, where the wake structure was significantly diffused as it convected toward the wing. The ability of the current methodology to resolve these interactions is studied, with the aim of resolving the detailed flow dynamics of the wake as it interacts with the wing. This requires that the propeller wake, and the tip vortices contained within

it, are preserved against any significant numerical diffusion as it convects through the solution domain.

This propeller-wing interaction is of interest primarily because the interaction induced significant lift and drag force on the wing, due to the axial and swirl velocity of the propeller wake. A wing design that exploits this interaction and recovers some of the rotational energy imparted to the flow from the propeller is therefore studied in the present work. This analysis is performed by coupling the current CFD solver with an optimisation algorithm, with the aim of studying how simple changes in the wing geometry can alter the efficiency of the wing.

1.4 Synopsis

The computational methodology used in the present analysis is presented in Chapter 2. First, a description of the baseline CFD solver is given, outlining the approach used to solve the governing equations numerically. Enhancements to the solver for the efficient analysis of unsteady flows are then described. These enhancements include the addition of second order accurate backward differencing time integration and dual time stepping, where the solution is advanced in *pseudo* time every timestep. The solution domain is discretised with structured overset meshes, and to facilitate computations where these meshes are in relative motion, a stencil walking algorithm is implemented to update the mesh connectivity. This algorithm produces an efficient method of searching for new donor cell which are needed even timestep to transfer flow information between separate meshes. A linear acoustic analysis is also presented which is based on the numerical solution of the Ffowcs Williams-Hawkings equation.

In Chapter 3, the problem of blade-vortex interaction occurring on helicopter rotors is studied and the current methodology is used to examine an idealised blade-vortex interaction problem. The problem is initially reduced to a two dimensional interaction, which greatly reduces the computational cost and complexity. Then, a full three-dimensional simulation is attempted where the vortex formation and its interaction is

fully resolved. The spatial and temporal resolution requirements are studied, and the results are validated against detailed experimental data. Acoustic wave propagation from the interaction is also computed using a linear acoustic analysis, and the three dimensional directivity of the acoustic waves from the blade surface is examined. This study confirms that the important flow physics of BVIs can be fully resolved using an inviscid representation of the flow, provided that sufficient care is taken to preserve the vortex structure and strength. The numerical diffusion can be sufficiently reduced to allow accurate preservation of the vortex structure with the current high fidelity methods, given adequate spatial and temporal resolution is used.

Chapter 4 studies the problem of a propeller wake-wing interaction in an idealised setup. The flow of an isolated propeller is first resolved and the axial and swirl velocity in its wake are validated against experimental data. Flow data from the isolated propeller wake is then used as an unsteady boundary condition to simulate a propeller wake-wing interaction. The wing-surface pressures in the region of the interaction are validated with experimental data, and the flow dynamics as the wake impacts and convects over the wing are observed. The flow solver is then coupled to an optimisation algorithm, where a wing design that exploits the interaction with the propeller wake is sought. The wing twist is varied to reduced the induced drag of the wing for a given lift. This work shows that the details of the wake-wing interaction can be fully resolved using the current methodology, and that the wake of a propeller and the wing-surface interaction pressures can be accurately predicted.

Finally, Chapter 5 concludes this dissertation with a summary of the work performed and the conclusions drawn. Suggestions for future work are then made based on these conclusions.

Chapter 2

Computational Methodology

The current work utilises and extends the Euler/Navier-Stokes solver CHRONoS (Compressible High Resolution Overset Navier-Stokes Solver) [53] which was developed primarily for the analysis of external aerodynamic flows. This Chapter outlines the baseline flow solver and the extensions developed for the efficient computation of unsteady flow problems involving vortex-lifting surface interactions. Also presented is a linear acoustic analysis that is used to study the acoustic energy radiated from these interactions.

2.1 Basic Flow Solver

2.1.1 The Euler Equations

A primary concern of the present work is to develop a methodology that is of sufficient accuracy to model the vortex dominated flows discussed in Chapter 1, where the formation of a tip vortex and its interaction with a lifting surface is resolved. All the flows considered in this thesis involve thin, attached boundary layers that are influ-

enced by vortex induced velocities. In this scenario, the flow is dominated by inviscid effects and viscosity is of secondary importance, unless the vortex induced velocity field causes separation. For instance, the separation of a viscous boundary layer during the formation of a tip vortex can cause the creation of secondary and tertiary vortices close to the wing surface [50], however these structures have a small effect on the overall vortex structure and strength because they typically merge downstream of the trailing edge of the wing. The viscous no-slip condition will also produce a boundary layer on the lifting surface with which the vortex interacts with, but resolving this has been shown to have a negligible effect of the resulting surface pressures for the interactions studied in the present work [27]. The salient flow features of the vortex-lifting surface interactions that are studied here are essentially inviscid in nature, and therefore the viscous terms in the governing equations have been neglected.

An inviscid description of the fluid is given by the Euler equations, which are a mathematical statement of the conservation of mass, momentum in the three spatial directions and energy. They can be written is conservative form as:

$$\frac{\partial Q}{\partial t} + \frac{\partial F}{\partial x} + \frac{\partial G}{\partial y} + \frac{\partial H}{\partial z} = 0 \tag{2.1}$$

Where Q is the vector of conserved variables and F, G and H are the inviscid fluxes in the x, y and z directions respectively. The vector of conserved variables is given by:

$$Q = \begin{Bmatrix} \rho \\ \rho u \\ \rho v \\ \rho w \\ e \end{Bmatrix} \tag{2.2}$$

The inviscid fluxes are given by:

$$F = \begin{Bmatrix} \rho u \\ \rho u^2 + p \\ \rho uv \\ \rho uw \\ u(e+p) \end{Bmatrix}, \quad G = \begin{Bmatrix} \rho v \\ \rho vu \\ \rho v^2 + p \\ \rho vw \\ v(e+p) \end{Bmatrix}, \quad H = \begin{Bmatrix} \rho w \\ \rho wu \\ \rho wv \\ \rho w^2 + p \\ w(e+p) \end{Bmatrix}, \tag{2.3}$$

where ρ is the fluid density, u, v and w are the velocity components in the three spatial directions and e is the energy per unit volume given by:

$$e = \frac{p}{\gamma - 1} + \frac{1}{2}\rho(u^2 + v^2 + w^2) \tag{2.4}$$

The numerical solutions will involve non-Cartesian geometries, as the meshes on which these equations are solved will have to conform to the physical geometry of the solid bodies in the solution domain. However, it is easier to achieve a higher order of numerical accuracy on a uniformly spaced Cartesian mesh. Therefore the equations have to be transformed from the physical domain of x,y and z to a regularly spaced Cartesian computational domain of $\xi(x, y, z)$, $\eta(x, y, z)$, and $\zeta(x, y, z)$. The transformed equations in conservation form are given by:

$$\frac{\partial \hat{Q}}{\partial t} + \frac{\partial \hat{F}}{\partial \xi} + \frac{\partial \hat{G}}{\partial \eta} + \frac{\partial \hat{H}}{\partial \zeta} = 0 \tag{2.5}$$

where

$$\begin{aligned}
\hat{Q} &= \frac{1}{J}Q \\
\hat{F} &= \frac{1}{J}[F\xi_x + G\xi_y + H\xi_z] \\
\hat{G} &= \frac{1}{J}[F\eta_x + G\eta_y + H\eta_z] \\
\hat{H} &= \frac{1}{J}[F\zeta_x + G\zeta_y + H\zeta_z]
\end{aligned} \tag{2.6}$$

and J is the transformation Jacobian.

2.1.2 Numerical Solution

The flow solver CHRONoS solves the Euler equations numerically on structured grids using a node centred finite volume approach [54]. The governing equations are integrated over each mesh cell, and this approach is preferred as strong flow gradient, such as shock waves, are naturally captured in the solution [55]. For a finite volume approach, the transformation Jacobian J of each cell, given in equation 2.6, is equal to the inverse of the cell volume and the transformation vector $[\xi_x, \xi_y, \xi_z]$, $[\eta_x, \eta_y, \eta_z]$ and $[\zeta_x, \zeta_y, \zeta_z]$ represents the face normals in the ξ, η and ζ directions respectively.

Discretising the spatial inviscid fluxes, the governing equations can be written in the following semi-discrete form:

$$\frac{d\hat{Q}}{dt} = -\frac{\hat{F}_{j+\frac{1}{2}} - \hat{F}_{j-\frac{1}{2}}}{\Delta\xi} - \frac{\hat{G}_{k+\frac{1}{2}} - \hat{G}_{k-\frac{1}{2}}}{\Delta\eta} - \frac{\hat{H}_{l+\frac{1}{2}} - \hat{H}_{l-\frac{1}{2}}}{\Delta\zeta} \tag{2.7}$$

where j, k and l are the indices in the ξ, η and ζ directions respectively. The half values of the indices denote the cell interface position. The space and time derivatives

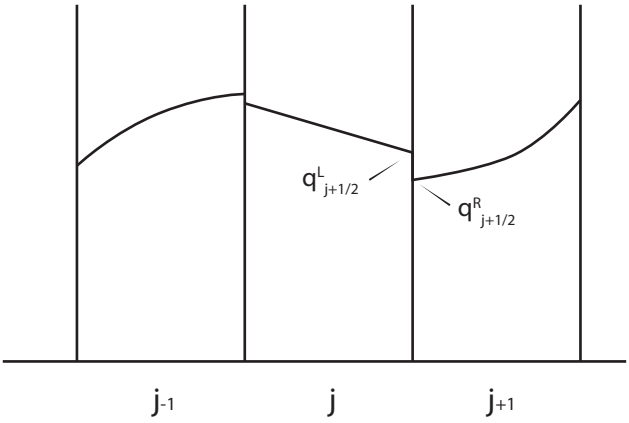

Figure 2.1: *Solution reconstruction within each cell.*

in equation 2.7 have been decoupled allowing it to be solved as a set of ordinary differential equations in time.

The spatial discretisation is therefore reduced to calculating the cell interface values of the inviscid fluxes $\hat{F}_{j\pm\frac{1}{2}}$, $\hat{G}_{j\pm\frac{1}{2}}$ and $\hat{H}_{j\pm\frac{1}{2}}$. These are computed using an upwind scheme [56], which has the advantage of naturally accounting for wave propagation. The evaluation of the interfacial fluxes in commonly done using a solution reconstruction approach. The solution distribution within the cell is reconstructed, giving the value of the solution at the edge of the cell, as illustrated in Fig. 2.1. The spatial accuracy is one order higher than that of the reconstructed solution within each cell and can be generalised to any order of accuracy. The solution is reconstructed in primitive variables:

$$q = \left\{ \begin{array}{c} \rho \\ u \\ v \\ w \\ p \end{array} \right\} \tag{2.8}$$

Each cell interface then becomes a local Riemann problem and the interfacial flux can be obtained using any flux splitting or differencing scheme. In the present work, the approximate linearised Riemann solver of Roe is used [57], where the intercell flux is given by:

$$F(q^L, q^R) = \frac{F(q^L) + F(q^R)}{2} - |\hat{A}(q^L, q^R)|\frac{q^R - q^L}{2} \tag{2.9}$$

where $\hat{A}$ is the Roe-averaged Jacobian [58].

2.1.3 Spatial Reconstruction

The preservation of a tip vortex structure and its strength as the vortex convects through the computational domain is paramount to the success of the present study. A common problem in the simulation of vortex-dominated flows is the diffusion of coherent vortical structures due to the inherent numerical dissipation. In the semi-discrete form of the governing equations shown in equation 2.7, the flux is piecewise reconstructed within each cell. A first order spatial scheme would reconstruct the flow variables as a constant value across the cell, equal to the cell average, and a second order spatial scheme would reconstruct the solution as a linear slope. The slope is calculated from a stencil of the appropriate number of surrounding cells and this approach can be generalised to any order of accuracy.

In general, a numerical scheme with a high order of spatial accuracy is desired when the solution is "*smooth*", where the spatial gradients of the flow variables are small. However, if the solution contains high flow gradients, such as shock waves, then a high order of accuracy spatial reconstruction scheme will tend to generate non-physical spurious oscillations across the high flow gradients. It is therefore required that the spatial order of accuracy drop to first order near high flow gradients, or that a cell stencil is chosen which ameliorates the effect of the sharp gradients.

In the present work, spatial differencing is performed using a 5^{th} order accurate Weighted Essentially Non-Oscillatory (WENO) scheme [59, 60]. WENO schemes are based on the Essentially Non-Oscillatory (ENO) schemes developed by Harten *et al.* [61] and Shu and Osher [62]. Both ENO and WENO schemes use adaptive stencils in the solution reconstruction procedure based on the local smoothness of the solution. The ENO scheme uses only the stencil with the smoothest solution out of the many candidate stencils, while the WENO scheme uses a convex combination of all the candidate stencils, each being assigned a non-linear weight which depends on the local smoothness of the numerical solution. A WENO scheme is in general more robust and has better convergence properties that the ENO scheme of the same accuracy due to the weighted combination of stencils used. For a $(2k+1)^{th}$ order WENO scheme, $(2k+1)^{th}$ order accuracy is approached in the smooth regions of the flow. In regions of the flow with high flow variable gradients such as shocks, the smoothest stencil is given the maximum weight, producing a $(k+1)^{th}$ order accurate reconstruction of the solution.

In general, intercell values at interface $q^L_{i-\frac{1}{2}}$ for a WENO scheme are given by

$$q^L_{i-\frac{1}{2}} = \sum_{r=0}^{k} w_r v^L_r \tag{2.10}$$

where w_r are the weights and v^L_r are the interpolations from the various stencils. Also

$$w_r = \frac{\alpha_r}{\Sigma^k_{s=0}\alpha_s}, \tag{2.11}$$

$$\alpha_r = \frac{d_r}{(\beta_r + \epsilon)^2} \tag{2.12}$$

where d_r is the optimal weight coefficient, β_r is the smoothness indicator. The variable $\epsilon = 10^{-6}$ is used to avoid a singularity. A $(2k+1)^{th}$ order accurate scheme can

be obtained by defining d_r, v_r^L and β_r appropriately. In the present work, a 5^{th} order WENO scheme is used, which has the following definitions,

$$
\begin{aligned}
v_0^L &= \frac{1}{3}\hat{q}_i + \frac{5}{6}\hat{q}_{i+1} - \frac{1}{6}\hat{q}_{i+2} \\
v_1^L &= \frac{-1}{6}\hat{q}_{i-1} + \frac{5}{6}\hat{q}_i + \frac{1}{3}\hat{q}_{i+1} \\
v_2^L &= \frac{1}{3}\hat{q}_{i-2} + \frac{-7}{6}\hat{q}_{i-1} + \frac{11}{6}\hat{q}_i \\
d_0 &= \frac{3}{10}, d_1 = \frac{3}{5}, d_0 = \frac{1}{10} \\
\beta_0 &= \frac{13}{12}(\hat{q}_i - 2\hat{q}_{i+1} + \hat{q}_{i+2})^2 - \frac{1}{4}(3\hat{q}_i - 4\hat{q}_{i+1} + \hat{q}_{i+2})^2 \\
\beta_1 &= \frac{13}{12}(\hat{q}_{i-1} - 2\hat{q}_i + \hat{q}_{i+1})^2 - \frac{1}{4}(\hat{q}_{i-1} + \hat{q}_{i+1})^2 \\
\beta_2 &= \frac{13}{12}(\hat{q}_{i-2} - 2\hat{q}_{i-1} + \hat{q}_i)^2 - \frac{1}{4}(\hat{q}_{i-2} - 4\hat{q}_{i-1} + 3\hat{q}_{i+2})^2
\end{aligned}
\tag{2.13}
$$

2.1.4 Boundary Conditions

2.1.4.1 Wall Boundary Conditions

At the surfaces of a mesh that represents a solid wall, an inviscid wall boundary condition is imposed explicitly. The density is first extrapolated from interior points to the wall points. The contravariant velocity components, U, V and W are also extrapolated from the interior of the mesh. The wall normal velocity is then set to zero such that no fluid penetrates the solid surface. The pressure, p is then obtained from the normal momentum equation [7].

2.1.4.2 Far-field Boundary Conditions

The meshes used in the present study have the mesh boundaries placed far away from the region of interest. Typically, the far-field boundaries will be placed over 30 chords away from the regions containing high flow gradients such as vortices. At the far-field boundary, the spatial resolution is very coarse, in the order of 1 chord. This will quickly dissipate any high flow gradients before they convect to the far-field boundaries and so characteristic-based Riemann invariants are used [63]. This boundary condition allows linear (low amplitude) disturbances to leave the computational domain without spurious reflections. In this approach, based on the sonic velocity, the corresponding Riemann invariants are extrapolated either from the interior or from the freestream.

2.1.4.3 Kutta Condition

To generate a flow solution that approximates attached viscous flow, the Kutta condition is explicitly imposed in the numerical solution. The Kutta condition can be stated as:

A body with a sharp trailing edge in motion through a fluid creates about itself a circulation of sufficient strength to hold the rear stagnation point at the trailing edge [5]

In the numerical solution, this condition is imposed by setting the velocity at the trailing edge of the aerofoil as an average of the velocities at the above and below mesh points. This condition guarantees a rear stagnation point, but is in general not needed due to the finite amount of numerical viscosity that is introduced into the flow from the discretisation of the governing equations. This viscosity causes the rear stagnation point to tend towards the trailing edge in the same manner as a real fluid. The phenomena has been observed in many numerical experiments and is discussed in more detail by Hirsch [63].

2.2 Enhancements to the flow solver

The baseline CHRONoS solver has been extended to accurately model the vortex-lifting surface interaction problems considered in the present work. The time integration accuracy has been improved to second order and dual time stepping is implemented to improve the convergence within each timestep. A stencil walking algorithm has also been implemented to efficiently compute the donor cells and interpolation factors of the overset meshes. These extensions are added to compute unsteady time accurate simulations in an efficient manner.

2.2.1 Time Integration

The time integration is performed implicitly, allowing for less restrictive CFL conditions and increasing the numerical stability over an explicit time integration method. The baseline solver utilised a backward Euler time integration with Newtonian sub-iterations within each timestep [64]. To improve the convergence rate within each timestep, dual time stepping is implemented. This method also improves the robustness of the numerical scheme allowing for larger timesteps. Dual time stepping was originally developed to allow larger timesteps in explicit time integration [65, 66] and has since been adapted for implicit time integration [67]. A *pseudo* time term is added to the governing equations and within each timestep, the solution is advanced in *pseudo* time. As the solution converges within each timestep, this pseudo time term disappears and the time accurate solution is approached.

Equation 2.7 can be discretised in time with dual time stepping as follows, where Δt is the physical timestep and $\Delta \tau$ is the pseudo timestep (in the case of Newton sub-iterations, $\Delta \tau = \infty$):

$$\frac{\hat{Q}^{k+1} - \hat{Q}^k}{\Delta\tau} + \frac{(1+\psi)(\hat{Q}^{k+1} - \hat{Q}^n) - \psi(\hat{Q}^n - \hat{Q}^{n-1})}{\Delta t} = -\hat{F}_\xi^{k+1} - \hat{G}_\eta^{k+1} - \hat{H}_\zeta^{k+1} \tag{2.14}$$

Here, the k superscript denotes the pseudo time counter and n denotes the real time counter. The choice of variable $\psi = 0$ will result in the first order backward implicit Euler scheme, and $\psi = 1/2$ will result in the second order backward difference scheme. As the solution is advanced in pseudo time and as $k \to \infty$, the pseudo time term disappears as $\hat{Q}^k = \hat{Q}^{k+1}$, and $\hat{Q}^{k+1} \to \hat{Q}^{n+1}$. The right hand side of equation 2.14 is linearised in time about $\hat{Q}^k$, such that:

$$\begin{aligned} \hat{F}^{k+1} &\approx \hat{F}^k + \hat{A}^k(\hat{Q}^{k+1} - \hat{Q}^k) \\ \hat{G}^{k+1} &\approx \hat{G}^k + \hat{B}^k(\hat{Q}^{k+1} - \hat{Q}^k) \\ \hat{H}^{k+1} &\approx \hat{H}^k + \hat{C}^k(\hat{Q}^{k+1} - \hat{Q}^k) \end{aligned} \tag{2.15}$$

where

$$\hat{A} = \frac{\partial \hat{F}}{\partial \hat{Q}}, \quad \hat{B} = \frac{\partial \hat{G}}{\partial \hat{Q}}, \quad \hat{C} = \frac{\partial \hat{H}}{\partial \hat{Q}} \tag{2.16}$$

$$\tag{2.17}$$

$\hat{A}, \hat{B}$ and $\hat{C}$ are the Jacobians of $\hat{F}, \hat{G}$ and $\hat{H}$, respectively. The resulting scheme can be written in *Delta Form*, with the unknown states collected on the left hand side.

$$\left[I - \frac{\Delta\tau}{1+\frac{(1+\psi)\Delta\tau}{\Delta t}}(\hat{A}+\hat{B}+\hat{C})\right]\Delta\hat{Q}^{k+1} =$$
$$\frac{\Delta\tau}{1+\frac{(1+\psi)\Delta\tau}{\Delta t}}\left[-\hat{F}^k_\xi - \hat{G}^k_\eta - \hat{H}^k_\zeta - \left(\frac{(1+\psi)(\hat{Q}^k-\hat{Q}^n)-\psi(\hat{Q}^n-\hat{Q}^{n-1})}{\Delta t}\right)\right] \quad (2.18)$$

where

$$\Delta\hat{Q}^k = \hat{Q}^{k+1} - \hat{Q}^k \quad (2.19)$$

The LHS of equation 2.18 is then inverted using a LUSGS factorisation scheme [68]. The real timestep Δt is kept constant across the whole solution domain for a time accurate computation. However, the pseudo time variable $\Delta\tau$ can vary, allowing local time stepping which is a common convergence acceleration technique used for steady state computations. In the present work, local time stepping is used with a constant local pseudo CFL number.

The residual drop for a typical aerofoil-vortex interaction simulation is shown in Fig. 2.2, using dual time stepping and 10 sub-iterations within a timestep. The details of this computation are given in section 3.2. A variety of local pseudo-CFD numbers (CFL_τ) are shown in addition to a timestep with no dual time stepping and using only Newtonian sub-iterations. For CFL_τ values over 2, the convergence rate of dual time stepping is typically an improvement over Newtonian sub-iterations. In all the computations presented in this work, a local CFL_τ of 20 is used. In general, dual time stepping improves the convergence rate within each timestep and is more robust than Newton sub-iterations, allowing for greater physical timesteps.

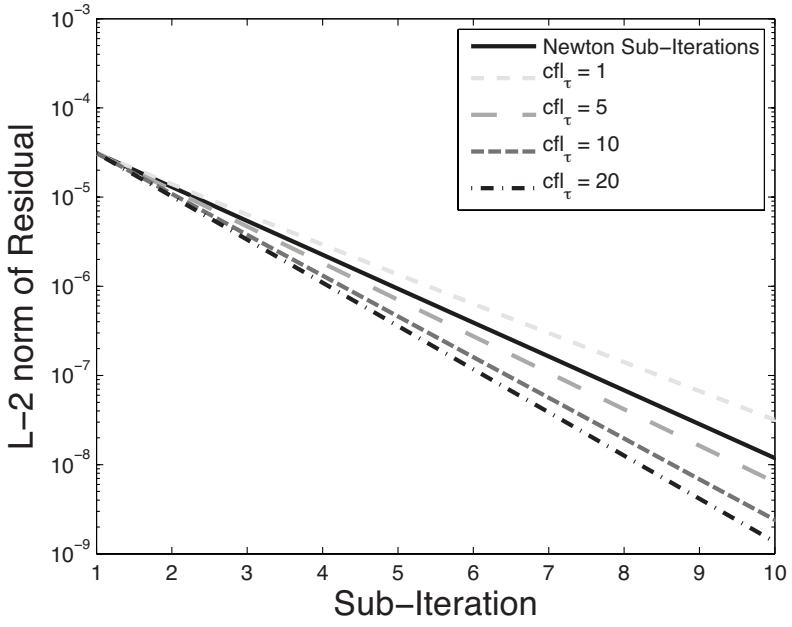

Figure 2.2: *Residual drop within a timestep using dual time stepping.*

2.2.2 Overset Meshes

The geometry of the range of problems investigated in this work is too complex to be represented by a single structured mesh. Complex geometries can be represented by unstructured meshes, but these require more memory and are less computationally efficient compared to structures meshes. Overset meshes allow high quality structured meshes to represent complex configurations. In this approach, different grids are generated independently and are overset in the regions of interest. In the current work, a larger background mesh is used to represent the majority of the solution domain, and within this blade meshes are overset to represent the lifting surfaces. The method of overset meshes was first proposed by Steger *et al.* [69] and Benek *et al.* [70]. This approach allows a high level of flexibility when generating meshes, as the mesh interfaces do not need to align with one another, as with a multi block structured mesh approach. It also allows mesh points to be easily clustered in regions of interest. Additional computations are required to calculate the correct donor cells and interpolation factors to

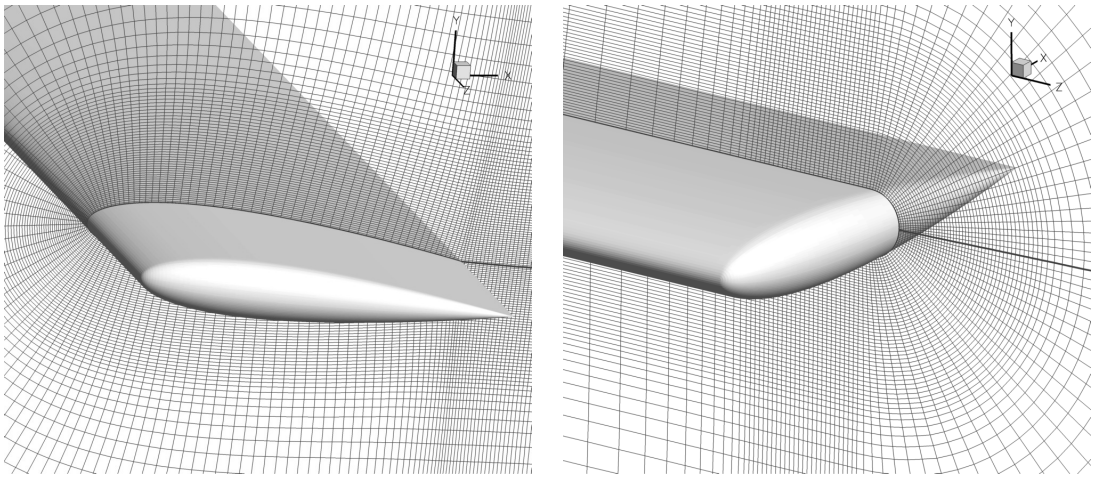

(a) *C topology mesh in chordwise direction* (b) *Mesh wraps around blade tip.*

Figure 2.3: *Discretisation of the near blade domain.*

transfer information between the meshes, however this can be minimised with the use of efficient algorithms. There is also a possible loss of the conservation property of the numerical scheme, but this can be managed by proper selection of mesh structure and placement.

The near blade domain is discretised using a body conforming C mesh topology. The C meshes are then stacked in the spanwise direction of the blade to create a 3D blade mesh as shown in Fig. 2.3. The spanwise planes are collapsed around the tip of the blade, allowing a high quality mesh in the tip region where the tip vortex is formed. The blade mesh is then overset onto a background mesh that represents the majority of the solution domain.

Flow information must then be transferred between the meshes during the simulations. This is transferred from the background mesh to the blade mesh through the so-called *chimera* boundary points. These are located at the exterior boundary of the overset blade mesh, and at these points the solution is interpolated from donor points in the background mesh. The volume inside, and surrounding, the solid surface of the blade is not solved for. This process is known as *iblanking*, and in the present work, the iblanked region is defined explicitly as a cuboid in the background mesh which en-

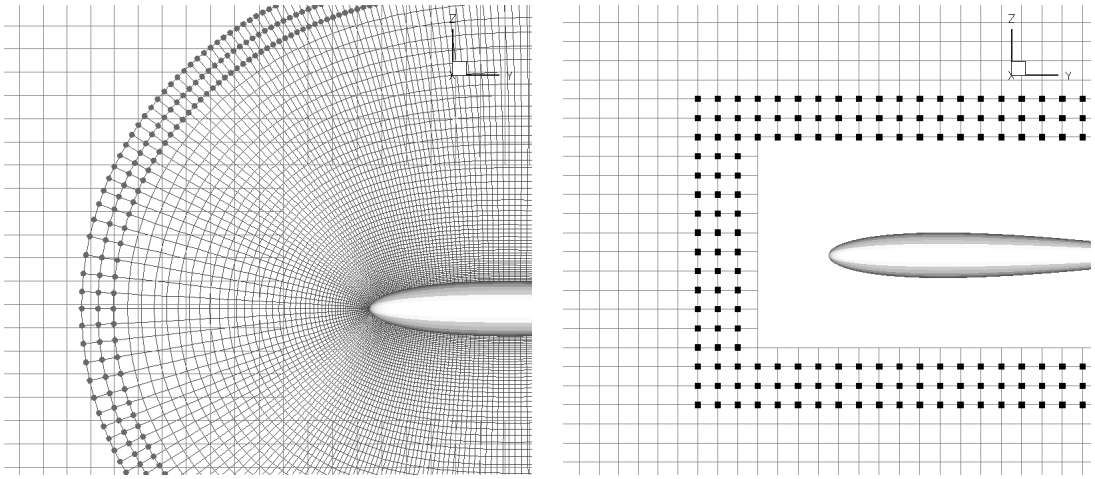

(a) *Chimera points of the blade mesh shown as circles.*

(b) *Fringe points of the background mesh shown as squares.*

Figure 2.4: *Chimera and fringe boundary points used in overset meshes. The iblanked hole surrounding the aerofoil is also shown.*

compasses the blade surface. Explicitly stating the iblanked region is easily performed in the present study where the blades have a simple planform, but a more general hole cutting method is needed to accommodate more complex geometries. At the edge of the blanked region are the *fringe* points and here the flow solution is interpolated from the blade mesh into the background mesh. The number of layers of chimera and fringe points required is determined by the stencil of the numerical scheme. In the present work, a 5^{th} order WENO scheme is used and the stencil requires 3 layers of points. The iblanked points, chimera boundary points and fringe points are shown in Fig. 2.4.

2.2.3 Stencil Walking Algorithm

The additional complexity that overset meshes create is that the donor points and the interpolation factors must be determined for all boundary and fringe points. For a steady mesh system, these must only be determined once at the beginning of the computation. If, however, the overset meshes are in relative motion to one another, new donor points and interpolation factors must be found at every timestep. Therefore,

it is important that an efficient algorithm is used to update the donor points and interpolation factors.

In the present work, a stencil walking algorithm is used to determine the connectivity information between grids. This algorithm is illustrated in Fig. 2.5 where point P is the location of the boundary point, for which information is to be interpolated to, and point D is the centre of an initial guess for the donor cell. The stencil walking algorithm first determines the face of the guess donor cell that is intersected by the vector $\vec{DP}$. This can be determined in the following manner.

The vector $\vec{DP}$ can be written in parametric form as:

$$\begin{aligned} x &= x_P + \phi\ x_{\vec{DP}} \\ y &= y_P + \phi\ y_{\vec{DP}} \\ z &= z_P + \phi\ z_{\vec{DP}} \end{aligned} \tag{2.20}$$

where ϕ is the free parameter and

$$\mathbf{P} = \begin{bmatrix} x_P \\ y_P \\ z_P \end{bmatrix} \tag{2.21}$$

Now, if the triangle **ABC** in Fig 2.5(a) is considered, any point within this triangle can be written as:

$$\begin{aligned} x &= f_1 x_A + f_2 x_B + f_3 x_C \\ y &= f_1 y_A + f_2 y_B + f_3 y_C \\ z &= f_1 z_A + f_2 z_B + f_3 z_C \end{aligned} \tag{2.22}$$

provided that

$$\begin{aligned} f_1 + f_2 + f_3 &= 1 \\ 0 \leq f_i &\leq 1 \end{aligned} \tag{2.23}$$

This leads to 4 equations and 4 unknowns to be solved. Written in matrix form this is:

$$\begin{bmatrix} x_A & x_B & x_C & -x_{\vec{DP}} \\ y_A & y_B & y_C & -y_{\vec{DP}} \\ z_A & z_B & z_C & -z_{\vec{DP}} \\ 1 & 1 & 1 & 0 \end{bmatrix} \begin{bmatrix} f_1 \\ f_2 \\ f_3 \\ \phi \end{bmatrix} = \begin{bmatrix} x_P \\ y_P \\ z_P \\ 1 \end{bmatrix} \tag{2.24}$$

The values of f_1, f_2, f_3 and ϕ are found by solving equations in 2.25 simultaneously and this is done using Cramer's rule. If f_1, f_2, f_3 and ϕ lie between 0 and 1, the vector intersects the triangle. For each guess donor cell, this is evaluated on the two triangles of every face of the cell until the intersected cell face is found. Then the donor cell is updated in the direction of the intersected plane, shown in Fig. 2.5(b). If the vector is found to intersect no cell face, then the final donor cell has been found.

This algorithm is ideally suited to searching within a Cartesian mesh. It can be

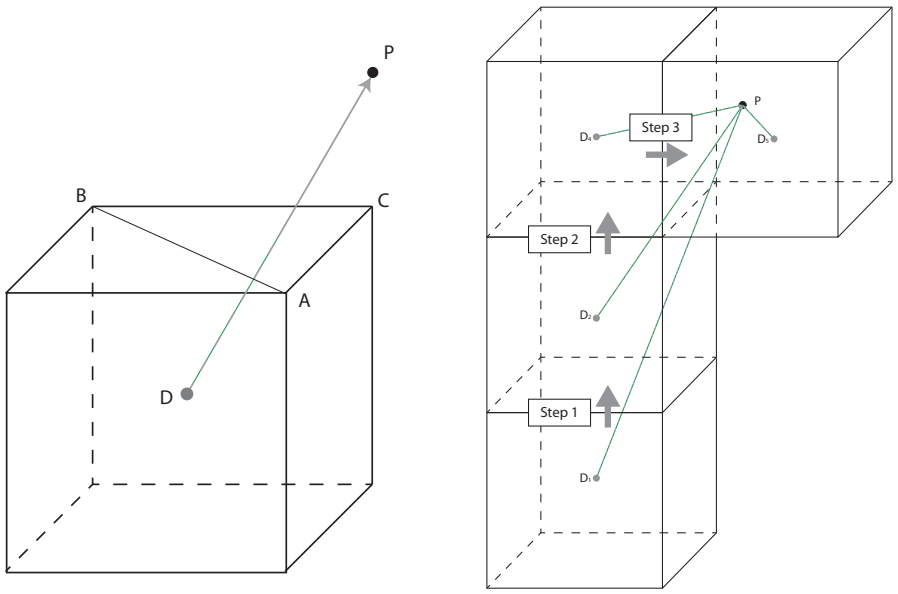

(a) *A vector is constructed from points* **D** *to* **P**, *and the cell face this vector intersects is determined.*

(b) *The algorithm then steps in the direction of the face intersection until the correct donor cell is found.*

Figure 2.5: *Illustration of stencil walking algorithm.* **P** *is the boundary point that information is to be interpolated to,* $\mathbf{D_i}$ *is the centre point of the* i^{th} *guess donor cell.*

adapted to search in more complex geometries, and in the present work the algorithm is used to search within a C-O topology blade mesh. In such a topology, the algorithm can fail if the vector $\vec{DP}$ crosses a solid boundary, or if the cells are highly stretched. However, it was found that all problems encountered in the practical implementation of the algorithm could be overcome be restarting the search from a different initial guess cell.

Once the donor cell is found, the interpolation factors can be calculated. These are given as weights α, β and γ, depicted in Fig. 2.6 for a unit cube. A first order interpolation uses these weights to interpolate a value from the 8 surrounding node points to the point P by:

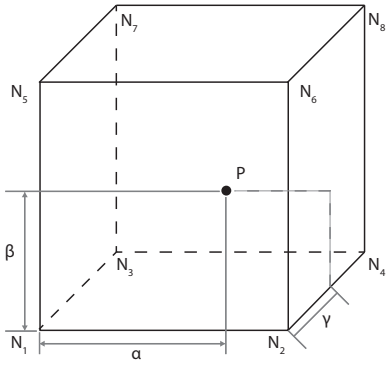

Figure 2.6: *First order accurate interpolation stencil on a unit cube.*

$$\begin{aligned} t_1 &= \beta(\alpha N_8 + (1-\alpha)N_7) + (1-\beta)(\alpha N_6 + (1-\alpha)N_5) \\ t_2 &= \beta(\alpha N_4 + (1-\alpha)N_3) + (1-\beta)(\alpha N_2 + (1-\alpha)N_1) \\ N_p &= \gamma t_1 + (1-\gamma)t_2 \end{aligned} \tag{2.25}$$

The order or accuracy of the interpolation can be increased by increasing the stencil size and interpolating from a greater number of node points surrounding P. A tricubic interpolation scheme utilises the surrounding 64 node points covering a $4 \times 4 \times 4$ stencil to interpolate the solution to P. The effect of the interpolation order of accuracy is studied in Chapter 3.

2.3 Acoustic Modelling

Vortex-lifting surface interactions can generate impulse changes in lift and subsequently radiate strong acoustic waves, and in this work these are studied. The modelling of these acoustic waves has been the focus of much research. Lighthill was among the first to model aerodynamic sources of noise mathematically with what is referred to as

Lighthill's acoustic analogy [71]. In brief, it is a statement of the conservation of mass and momentum in the form of an inhomogeneous wave equation. The source term of this inhomogeneous equation is a volume integral over all the acoustic sources in the flow. Ffowcs-Williams and Hawkings [72] developed this approach in more general terms [72] and defined three source terms. Two of these originate on the surface of a body and are related to the loading and thickness noise of a blade. The third is related to the volume sources that surround the body. This theory was first applied to rotor analysis by Hawkings and Lowson [73] and is now extensively used for rotorcraft aeroacoustic analysis. More efficient formulations have since been developed and the current work utilises the Farassat 1A formulation [74, 75].

Acoustic wave propagation is determined by the wave equation, given by:

$$\frac{1}{a^2}\frac{\partial^2 p}{\partial t^2} - \nabla^2 p = q(\vec{x}_{source}, t) \tag{2.26}$$

Where p is the acoustic pressure, a is the speed of sound and q is the acoustic sources. A description of the acoustic sources is needed and then the above equation can be integrated numerically to find the sound pressure at an observer location, x. For a sound wave emitted after time τ from the source, the wave will reach the observer at time $t = \tau + r/a$.

The Farassat 1A formulation of the Ffowcs-Williams and Hawkings equation is given by the following:

$$p_{linear}(\vec{x}, t) = p_T(\vec{x}, t) + p_L(\vec{x}, t) \tag{2.27}$$

where p_T is the thickness noise and p_L is the loading noise, given by:

$$
\begin{aligned}
4\pi p_T(\vec{x},t) &= \int_{f=0}\left[\frac{\rho_\infty \dot{v}_n}{r(1-M_r)^2}\right]_{ret} dS + \\
&\quad \int_{f=0}\left[\frac{\rho_\infty v_n(r\dot{M}\hat{r}_i + aM_r - aM^2)}{r^2(1-M_r)^3}\right]_{ret} dS
\end{aligned} \tag{2.28}
$$

$$
\begin{aligned}
4\pi p_L(\vec{x},t) &= \frac{1}{a}\int_{f=0}\left[\frac{\dot{l}_i\hat{r}_i}{r(1-M_r)^2}\right]_{ret} dS + \\
&\quad \int_{f=0}\left[\frac{l_r - l_i M_i}{r^2(1-M_r)^2}\right]_{ret} dS + \\
&\quad \frac{1}{a}\int_{f=0}\left[\frac{l_r(r\dot{M}_i\hat{r}_i + aM_r - aM^2)}{r^2(1-M_r)^3}\right]_{ret} dS
\end{aligned} \tag{2.29}
$$

Here ρ is the density of the fluid, v_n is the wall normal velocity at the blade surface, l_i is the lift force in the i direction, a is the speed of sound, M_i is the Mach number in the i direction and r is the distance from the source to the observer. $\dot{M}_i$, $\dot{l}_i$ and $\dot{v}_n$ denote the rate of change of the variable with respect to time. The factor $(1 - M_r)$ present in all the denominators represents the Doppler amplification, and the integration is performed around a closed surface.

The thickness noise sources are a function of $\rho_0\dot{v}_n$ and $\rho_0 v_n$, and this can physically be recognised as a solid body displacing a mass of fluid as it moves. For an aerofoil, the forward section displaces fluid outwards and acts as a pressure source, while the aft part of the aerofoil acts as a pressure sink; this is illustrated in Fig. 2.7(a). The pressure source and sink are separated by a small distance and have different retarded times to an observer. A result of this mass displacement is a pressure change that propagates through the fluid and is strongly radiated in the plane of the rotor. The thickness noise has a far-field component, which has the factor r in the denominator of equation 2.28, and a near-field component, which has r^2 in the denominator.

A typical thickness noise signature propagated from a single bladed rotor is illustrated in Fig. 2.7(b). This is a non-lifting rotor at zero incidence to a freestream Mach number of 0.15 and advance ratio of $\mu = U_\infty/U_{tip} = 0.2$. Contour levels of sound pressure are shown on a plane that is coincident with the rotor plane and the thickness noise is seen to spiral out from the rotor blade tip. A typical acoustic pressure pulse generated by the thickness noise sources is shown in Fig. 2.7(c) and is characterised by a large negative pulse. The magnitude of this pulse is largest in the plane of the rotor, and out of the rotor plane it rapidly diminishes.

The components of the loading noise are dependent on the pressure exerted by the solid body on the fluid and its gradient with respect to time. This noise source is analogous to a pressure dipole on the rotor blade, the strength of which is proportional to the loading on the rotor blade. The loading noise radiates out of plane of the rotor, and its far-field component, which is represented by the first term in equation 2.29, is proportional to the time rate of change of the blade loading. This is the most important noise source for the modelling of vortex-lifting surface interaction noise, and the vast majority of the out of plane noise in the far-field is accounted for with this noise source. Loading noise can also radiate in the plane of the rotor, the origin of which is the drag forces on the blade.

A more complete description of noise sources on a rotor is given by Schmitz [76]. This current approach neglects the quadrupole, or volume noise sources that are located in the fluid that surrounds the rotor blade. The physical origin of this noise can be shockwaves or Reynolds stresses in the region surrounding the body. The prediction of the noise originating from these sources is subject to ongoing research where the goal is to find an efficient and accurate method of accounting for them [77]. However, for the far-field noise computation of the interactions studied in this work, these noise sources are relatively not as important as loading and thickness noise sources [78].

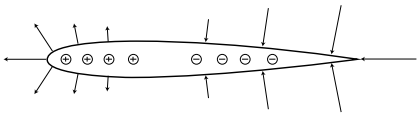

(a) *Thickness noise generated from an aerofoil displacing fluid.*

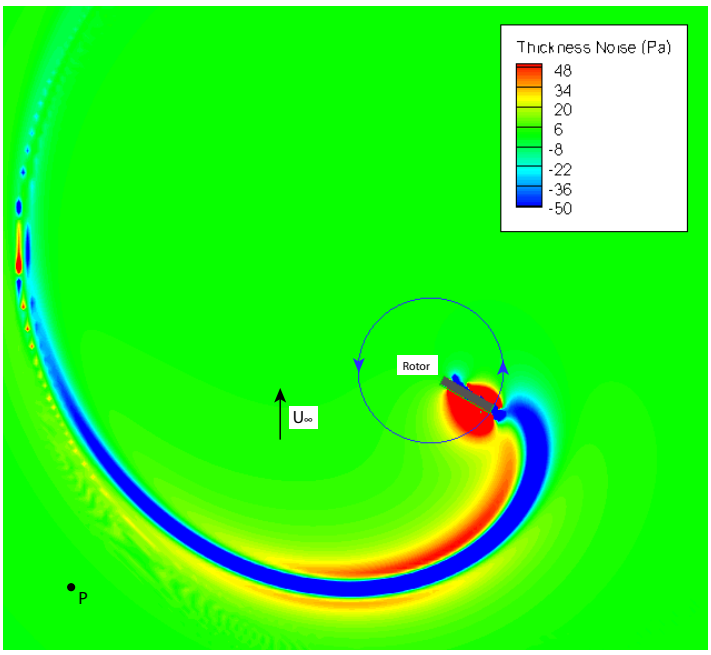

(b) *Thickness noise propagated from rotor blade in the plane of the rotor.*

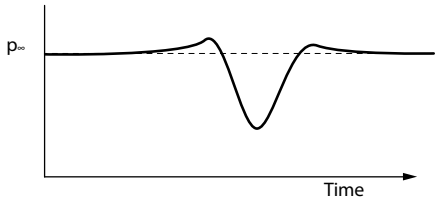

(c) *Typical thickness noise pressures in the rotor plane. Taken at point P in the above figure.*

Figure 2.7: *Thickness noise propagating in the plane of the rotor.*

2.4 Summary

The high-resolution solver CHRONoS has been presented and its important features highlighted. This solver was developed to solve the Euler/Navier-Stokes equations with the aim of resolving the formation of tip vortices and preserving their structure by minimising numerical dissipation. This is achieved through the use of a 5^{th} order accurate WENO discretisation of the inviscid numerical fluxes and high quality overset meshes. Using these methods, the formation of a steady tip vortex can be accurately computed and preserved in the solution domain against numerical diffusion. The vortex-lifting surface interactions that are studied in the present work are largely inviscid phenomena, so viscous effects are neglected. This also allows the numerical diffusion inherent in the flow solver to be assessed.

Extensions made to this methodology for the present work have also been discussed. The order of time integration accuracy has been modified by implementing a second order backward differencing scheme. Also, to increase convergence within each timestep and improve the numerical stability of the solver, dual time stepping with a pseudo timestep is implemented. To facilitate the use of moving overset meshes, a stencil walking procedure is implemented to search and update the donor and interpolation factors of the overset meshes. This algorithm is used to efficiently update the mesh connectivity information every timestep. These extensions are implemented to make the high-resolution simulation of unsteady problems involving meshes in relative motion possible.

A linear acoustic analysis has also been presented and the thickness, loading and volume noise sources were discussed. This analysis is based on the solution of the Farassat 1A formulation of the Ffowcs-Williams and Hawkings equation, where the thickness and loading noise sources of the rotor blade are used to compute the acoustic energy radiated to an observer location. This analysis neglects the volume noise sources that surround the plane, originating from shockwaves or Reynolds stresses in the boundary layer. However, these noise sources are small compared to the loading and thickness sources, and do not contribute significantly to the far-field noise.

Chapter 3

Blade-Vortex Interactions

The present Chapter will study the blade-vortex interactions which arise on helicopter rotors using the flow solver described in Chapter 2. These interactions are a major source of aeroacoustic noise on a helicopter rotor, and the ability to accurately model these interactions is paramount for the design of quiet helicopters.

An idealised BVI is examined as this approach allows the CFD solver to be rigorously evaluated against experimental data. The idealised interaction represents all the important physics of a realistic BVI in a simplified manner, and a brief description of the experimental setup is first given. This idealised interaction is highly two-dimensional so the problem is first modelled as a two-dimensional aerofoil-vortex interaction (AVI). The current methodology is used to resolve two distinct cases of AVI, and the results are compared with experimental data and a lower fidelity indicial model.

The method is then extended to perform a three-dimensional simulation where the vortex formation and interaction are fully resolved. Initially, the formation of an isolated vortex from a static vortex generator is studied and compared with experimental data. The ability of the moving overset meshes is then assessed, where the tip vortex must be passed between moving meshes accurately. Finally, a fully three dimensional interaction is resolved and compared to experimental data.

The interaction generates strong acoustic waves, and these are studied here using a linear acoustic analysis. The linear acoustic results are compared with experimental data in the near-field and the far-field. This analysis is also used to study the directivity of the acoustic waves propagated from the interaction.

3.1 Experimental Data

The experiments of Caradonna *et al.* [19] studied several idealised interactions of a vortex with a rotor blade. The vortex was generated by a static vortex generator wing placed upstream of the rotor. This wing was composed of a NACA 0015 aerofoil with an untwisted rectangular planform. The incidence and position of the vortex generator could be varied, allowing the position, strength and rotational sense of the vortex to be controlled accurately. A two bladed rotor was placed downstream of the vortex generator. The rotor blades were composed of a straight untwisted NACA 0012 rectangular planform with an aspect ratio of 7.125, and a chord (c) a third of the size of the vortex generator chord (c_{VG}). The blades were stiffened to minimise any aeroelastic effects and were inclined at zero angle of attack to minimise the creation of its own tip vortices.

The experiments were performed at a freestream Mach number of 0.142. A static vortex formed at the vortex generator, which then convected approximately 3 c_{VG} downstream to the rotor. The vortex axis was aligned with the quarter chord of the rotor blade at an azimuth of 180°. Chordwise surface pressures were collected at 3 radial locations on the rotor blade, over a period of 32 rotor revolutions. This data was ensemble averaged, and it was verified that this averaging process did not degrade the data. The test chamber was acoustically treated allowing sound pressure measurements to be taken. Seven microphones were used; 5 in the far-field and 2 in the near-field, and acoustic data was taken over a period of 30 rotor revolutions and averaged. This averaging caused no significant smear of the acoustic pulses. The experimental setup is illustrated in Fig. 3.1 & 3.2, and the experimental parameters are summarised in Table 3.1.

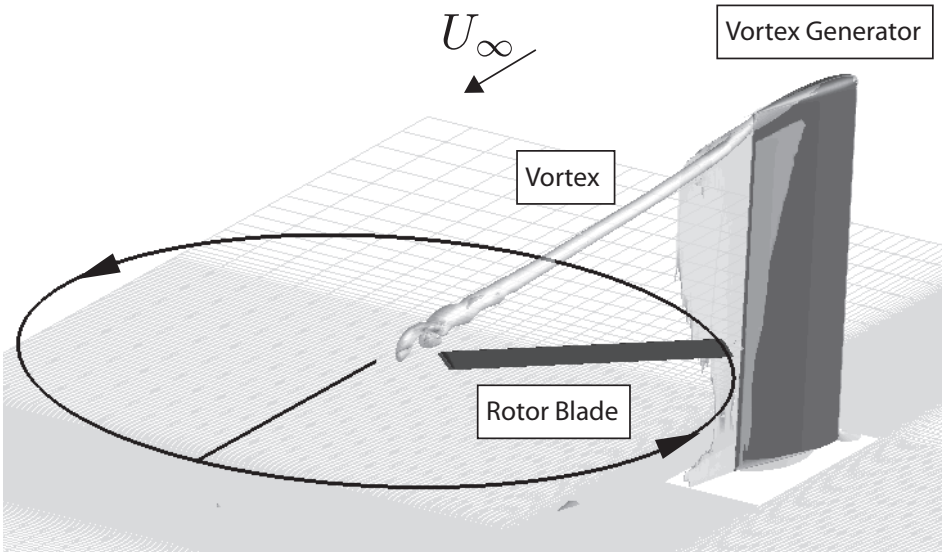

Figure 3.1: *3D view of the experimental setup of Caradonna* et al.

An experimental study performed by McAlister [20] studied the detailed creation and development of the tip vortex trailed by a static NACA 0015 wing under the same conditions as the vortex generator used in the BVI experiments of Caradonna *et al.* [19]. This study included detailed velocity measurements of the vortex, and at the point of interaction with the rotor blade the vortex was found to be best represented by the empirical expression given in equation 3.1.

$$\bar{V}_\theta(r) = \frac{\bar{\Gamma}}{2\pi} \frac{\bar{r}}{\bar{r}_v^2 + \bar{r}^2} \tag{3.1}$$

Here, $\bar{\Gamma}$ is the circulation of the vortex, $\bar{r}$ is the distance from the vortex centre and $\bar{r_v}$ is the vortex core size. These quantities are normalised by:

$$\bar{V} = \frac{V}{a_\infty}, \qquad \bar{\Gamma} = \frac{\Gamma}{a_\infty c}, \qquad \bar{r} = \frac{r}{c} \tag{3.2}$$

For the wing at an angle of attack of 12°, the best overall fit for the vortex was

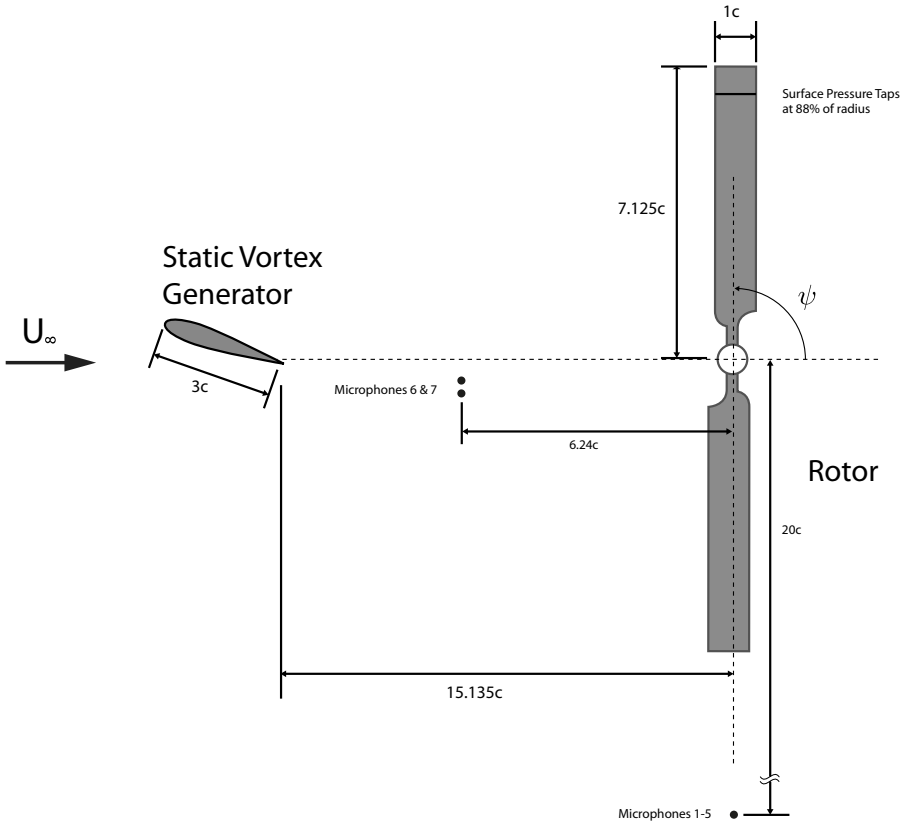

(a) *Experimental Setup of rotor and static vortex generator*

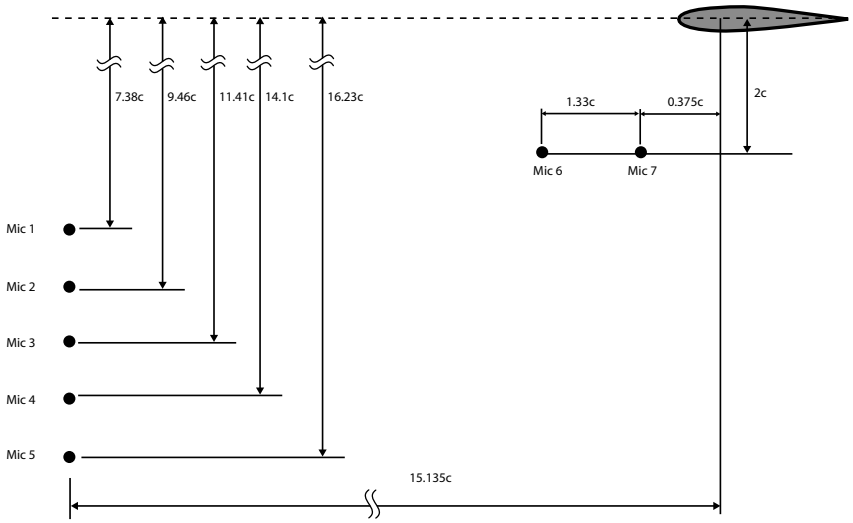

(b) *Location of microphones, blade shown at* $\theta = 180$

Figure 3.2: *Experimental setup of Caradonna* et al.

Propeller Conditions	
M_∞	0.142
M_{tip}	0.715
μ	0.198
Rotor Aerofoil	NACA 0012
Rotor Chord (c)	6"
Rotor Aspect Ratio	7.125
Vortex Generator Aerofoil	NACA 0015
Vortex Generator Chord (c_{VG})	18"
Reynolds number (Vortex Generator)	$600,000$

Table 3.1: *Summary of experimental conditions*

found to be $\bar{\Gamma} = 0.15884$, and $\bar{r}_v = 0.162$ [78].

This experiment is ideal for comparison with analytic methods due to the availability of both surface pressure and acoustic data in both the near-field and the far-field. Also, because the rotor is interacting with a steady tip vortex, details about the the location, structure and strength of the vortex are well defined by experiment. In contrast, the tip vortex system generated by more realistic rotor undergoing self-induced BVI more complex.

The experimental study collected data from a variety of vortex strengths, and vortex-blade vertical miss distances. The present computational work will focus on the interaction of a vortex trailed from a vortex generator at 12° angle of attack. This vortex had the largest circulation in the experimental work, which will produce a strong interaction. Two vortex-blade miss distance cases will be studied; a case where the vortex passes below the camber-line of the rotor blade by $0.25c$, denoted as the "weak" interaction, and a case where the vortex impacts directly on the leading edge of the blade, denoted as the "strong" interaction. The blade-vortex miss distance and the vortex rotational sense is illustrated in Fig. 3.3. These cases represent two distinct interactions. During the weak interaction, the core of the vortex passes below the rotor blade, which causes little distortion to the vortex structure. The blade surface pressures of a weak interaction can be accurately predicted using a prescribed vortex

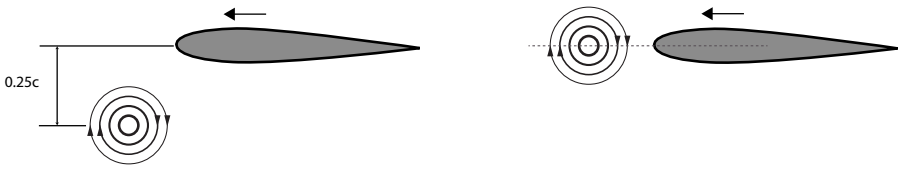

(a) *Weak interaction* (b) *Strong interaction*

Figure 3.3: *Blade-vortex miss distance and vortex rotational sense.*

approach. Conversely, during a strong interaction the vortex structure is severely distorted by the rotor blade as it impact directly with the vortex core, and this distortion must be fully resolved to accurately predict the interaction [78].

It should be noted that the miss distance between the vortex and the rotor blade is a random parameter due to the "vortex wander" or "vortex meander" during the experiments. Vortex wander is the random transverse motion of the vortex about its average path and is a well known phenomena that is strongly related to the freestream turbulent of the flow. The original experimental study did not attempt to quantify the vortex wander, however it can be estimated from the experimental work of Bailey and Tavoularis [79]. From this experimental study, the standard deviation of the amplitude of the vortex wandering can be estimated to be approximately $0.5r_c$. As will be shown in section 3.2.5, this variation in the vortex-blade miss distance will have a small effect on the interaction strength for both weak and strong interactions.

3.2 2D Aerofoil-Vortex Interaction Study

The highly two dimensional nature of the parallel BVI involved in the experiments performed by Caradonna *et al.* allows the interaction to be approximated by a two dimensional simulation of an aerofoil-vortex interaction (AVI). This approximation allows a CFD solver to be evaluated on a problem that retains much of the features of a three dimensional BVI, but on a much simpler configuration that is significantly less

computationally expensive.

3.2.1 Vortex Modelling

To simulate an AVI, the vortex must be accurately introduced into the solution. For the present problem, the vortex will be introduced into the flow as a perturbation from the freestream conditions using equation 3.1. The pressure and density are calculated using the approximation to the Euler equations $\frac{dp}{dr} = \rho\frac{v_\theta^2}{r}$ and the adiabatic relation $h(r) + \frac{v_\theta^2}{2} = h_\infty$. The computational solver must be able to convect the vortex with minimal diffusion from the numerical scheme. As the present work is restricted to the solution of the Euler equations, the correct result is the steady convection of the initial vortex profile with zero dissipation.

To assess both the ability of the flow solver to convect the vortex accurately and the grid resolution required, a computation of a freely convecting vortex is performed. This is performed on Cartesian meshes of three different resolutions, where the spatial resolution in the region of vortex convection is varied. The resolutions are summarised in Table 3.2, and are defined as mesh points across the vortex core. The vortex is initiated at the beginning of the computation using the perturbation from the free stream conditions described in equation 3.1 and convects at the freestream velocity. The timestep and sub-iterations within each timestep, have been refined such that the error from time integration is negligible, allowing the error from the 5^{th} order accurate WENO spatial discretisation scheme to be assessed. The boundary of the mesh is placed over $100r_c$ away from the convecting vortex, and at these boundaries freestream conditions are applied. The vortex convects at Mach 0.626, which is the relative velocity between the blade and the vortex at 88% of the blade span in the experimental setup.

The peak-to-peak velocity and core size of the vortex is shown in Fig. 3.4 as the vortex convects through the solution domain for the three mesh resolutions. The peak-to-peak velocity and vortex core size are both normalised by their respective initial

Resolution	Points Across Vortex Core Diameter
Low	4
Medium	8
High	20

Table 3.2: *2D mesh spatial resolution*

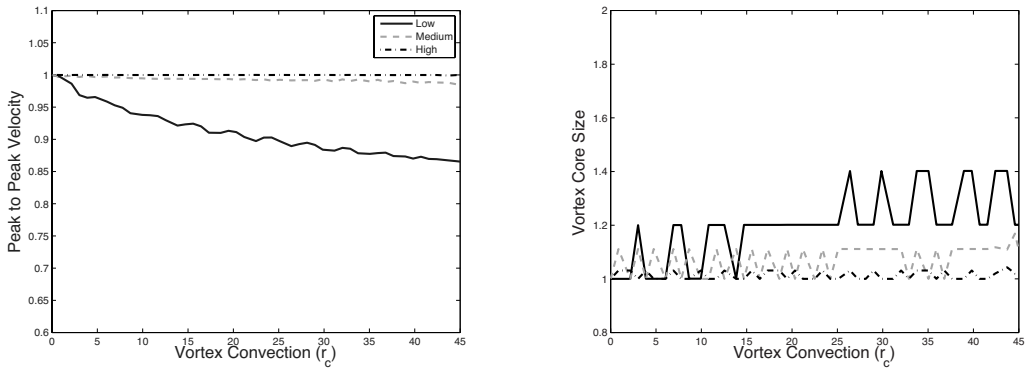

(a) *Peak-to-peak vortex velocity.* (b) *Vortex core size.*

Figure 3.4: *Vortex properties as vortex convects through domain on a high, medium and low resolution mesh.*

values. It can be seen that the high resolution mesh maintains the vortex profile throughout computation with negligible diffusion, and the medium resolution mesh is approximately at 99% of the initial value after convecting $45r_c$. The low-resolution mesh has insufficient resolution to maintain the vortex profile accurately, as the vortex profile diffuses as it convects through the solution domain. Similar results can be seen for the core size of the vortex, where both the high and medium resolution meshes maintain the initial structure of the vortex, and the low resolution mesh shows the vortex structure to be highly diffusive. These results indicate that for this WENO scheme to preserve the important features of a vortex, a minimum resolution of approximately 8 mesh points across the vortex core must be used.

In a real fluid, a convecting vortex will decay due to laminar and turbulent diffusion, causing the vortex core to expand. An expression for the laminar diffusion of a vortex was derived by Lamb [80], and further modified by Squire [81] to approximate the

turbulent effects. The growth of the vortex core, r_c, is given as:

$$r_c(t) = \sqrt{r_0^2 + 4(1+\delta)\alpha\nu t} \tag{3.3}$$

Where ν is the kinematic viscosity, r_0 is the initial vortex core size and $\alpha = 1.25643$ is Lamb's constant. The effects of the turbulent diffusion is represented by the parameter $\delta > 0$, which is dependent on Reynolds number. The corresponding decay in vortex swirl velocity can be found by combining equation 3.3 with equation 3.1. It has been shown that the above framework can represent experimental data of vortex diffusion well [82] for different Reynolds numbers. For the present flow conditions the diffusion of the vortex is small, where equation 3.3 gives a core expansion of just 0.43% after $45r_c$ of steady convection (9.3% of this is laminar diffusion, while the remaining in caused by turbulence, approximating $\delta = 8$). Therefore, the vortex decay caused by the numerical diffusion is potentially far greater than the natural laminar and turbulent diffusion for these flow conditions.

3.2.2 Aerofoil Surface Pressures

The simulation of a 2D AVI is performed on a 2-mesh system. The mesh system is comprised of a Cartesian background mesh with an overset C topology blade mesh. The Cartesian mesh has dimensions of 325×156 in the freestream and cross-stream directions respectively. In the region of vortex convection, mesh points are clustered to a resolution of approximately 8 points across the vortex core, and the spacing is increased towards the mesh boundaries. At the boundary the mesh spacing is large, such that any strong flow features will diffuse before propagating there, and the characteristic freestream boundary condition can be applied. The blade mesh is overset onto this Cartesian mesh, around which a hole in the background mesh is "iblanked",

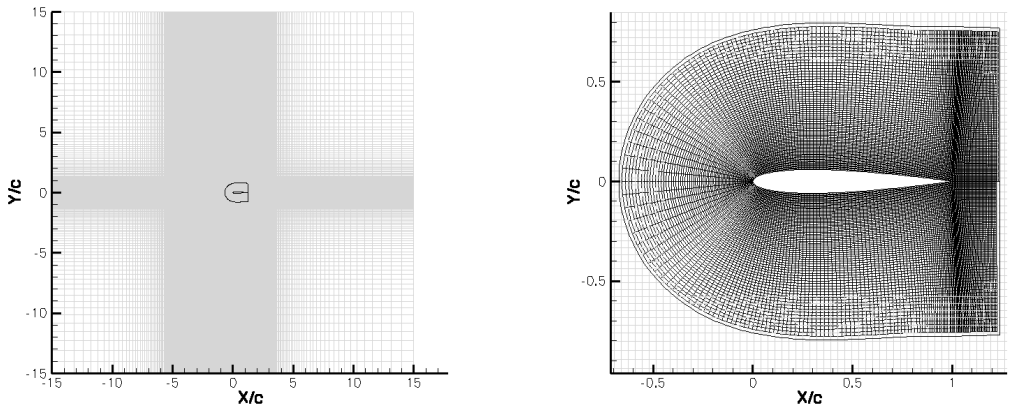

(a) *Full AVI mesh system.* (b) *Overset aerofoil mesh detail.*

Figure 3.5: *Details of AVI mesh.*

and at these points the flow equations are not solved. Information is cycled between the two meshes though the blade mesh boundary points and the Cartesian mesh fringe points. The dimensions of the blade mesh are 261×73 in the chordwise and wall normal directions respectively. The mesh system is shown in Fig. 3.5.

The flow parameters for the 2D AVI simulation are an approximation of the blade-vortex interaction that occurs at 88% span of the rotor blade in the Caradonna *et al.* experiments. This location was chosen due to the availability of pressure transducers, allowing for a direct comparison of experimental and computational results. The freestream velocity used in the simulation is Mach 0.626, which is the velocity of the 88% span section of the experimental rotor blade at azimuth of 180°. The steady flow around the aerofoil at this speed is initially computed. The vortex is then introduced into the flow upstream of the aerofoil and allowed to freely convect. The upstream position at which the vortex is initiated was found to have a negligible effect on the interaction results for distances greater than $3c$ upstream, and for the present simulations the vortex is initiated $5c$ upstream.

Two vortex-blade miss distance cases are performed; a weak interaction where the vortex misses the blade by $\frac{1}{4}c$, and a strong interaction where the vortex impacts

directly onto aerofoil. The weak interaction case can be successfully modelled using lower order methods [8, 78] as the vortex core passes well below the blade and the vortex structure is subject to minimum distortion. The direct impact case is harder to simulate accurately due the vortex deformation as it encounters the aerofoil, which must be accurately resolved.

The aerofoil surface pressure results are shown in Fig. 3.6 for the weak interaction, and Fig. 3.7 shows the surface pressures for the strong interaction. The results show the surface perturbation C_p for both the upper and lower surface of the aerofoil at various chordwise locations, where the upper surface C_p is offset by +0.6 for clarity. An equivalent azimuth, ψ_{eqv} is used for comparison with the experimental data. At some chordwise locations experimental data was not available, and at these points the computational results are not presented.

The characteristic surface pressure jump is captured well for the interaction in both cases. This is most prominent at the leading edge of the aerofoil, at a location of $\frac{x}{c} = 0.02$, and the magnitude of the jump decays towards the trailing edge. Both the strong and weak interaction cases are well captured in both magnitude and shape of the pressure pulse. These results indicated that the important features of the interaction are being accounted for, and that an inviscid approach will yield an accurate representation of the surface pressures. It also indicates that the deformation of the vortex is being accurately modelled.

A greater insight into the details of the interaction can be gained by examining the surface pressures across the chord of the aerofoil. The surface pressures on the lower surface of the aerofoil are shown in Fig. 3.8(a) for the weak interaction and Fig. 3.9(a) for the strong interaction. These figures reveal the convection and propagation events that occur as the vortex passes over the blade, which are labelled in Fig. 3.8(c) and Fig. 3.9(c). As the vortex approaches the blade, the pressure on the lower surface begins to reduce due to the induced velocity of the vortex. When the vortex reaches the leading edge of the blade, the lower surface pressures rises sharply. This sudden change in pressure travels rapidly from the leading to the trailing edge of the aerofoil, with the greatest rise occurring at the leading edge. This propagation is known as the

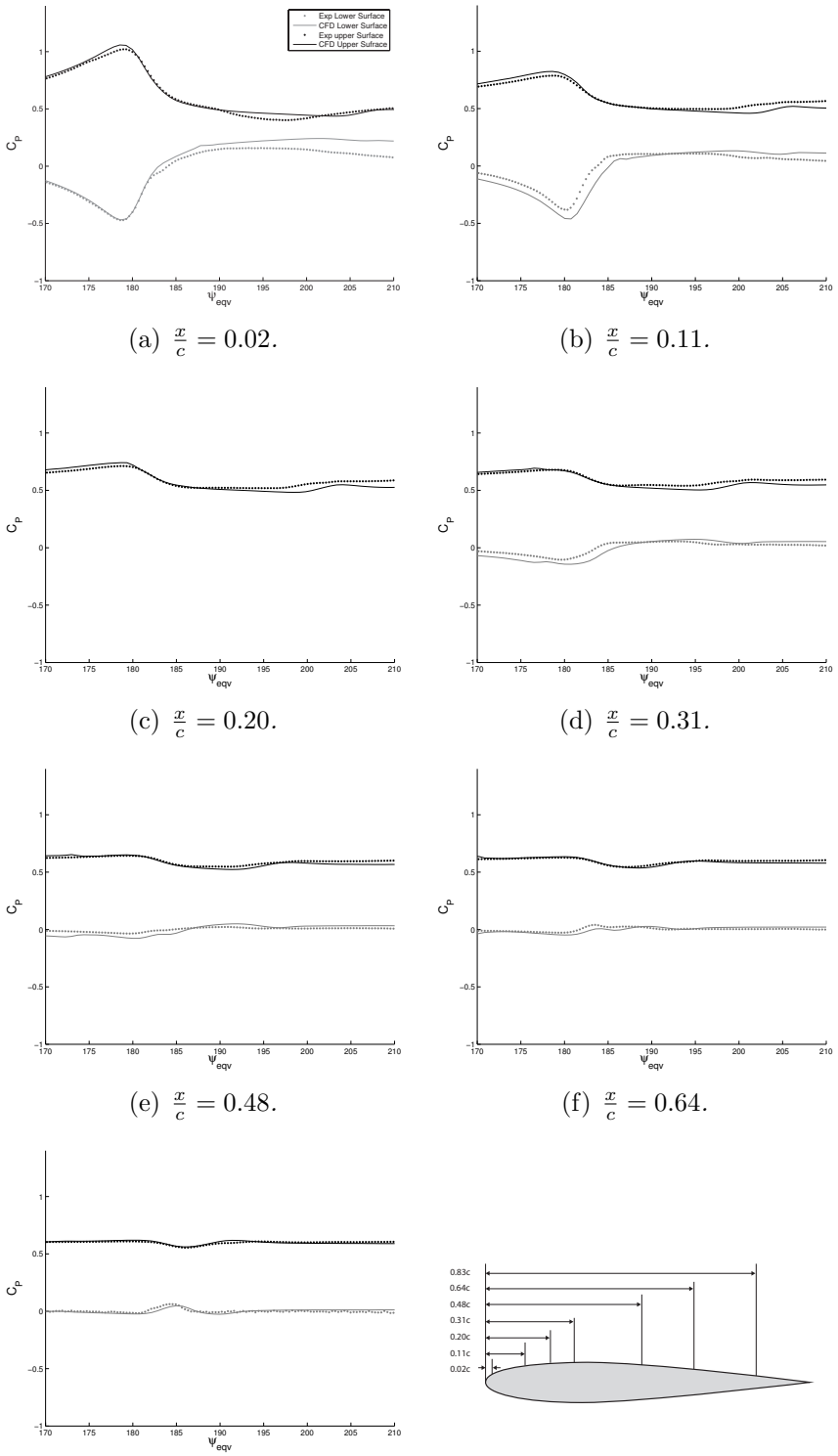

(a) $\frac{x}{c} = 0.02$. (b) $\frac{x}{c} = 0.11$.

(c) $\frac{x}{c} = 0.20$. (d) $\frac{x}{c} = 0.31$.

(e) $\frac{x}{c} = 0.48$. (f) $\frac{x}{c} = 0.64$.

(g) $\frac{x}{c} = 0.83$. (h) *Surface pressure locations.*

Figure 3.6: *Aerofoil Surface C_P during a weak AVI for various chordwise location on the upper and lower surface.* $\frac{y_v}{c} = -0.25$. *Upper surface C_P offset by* $+0.6$

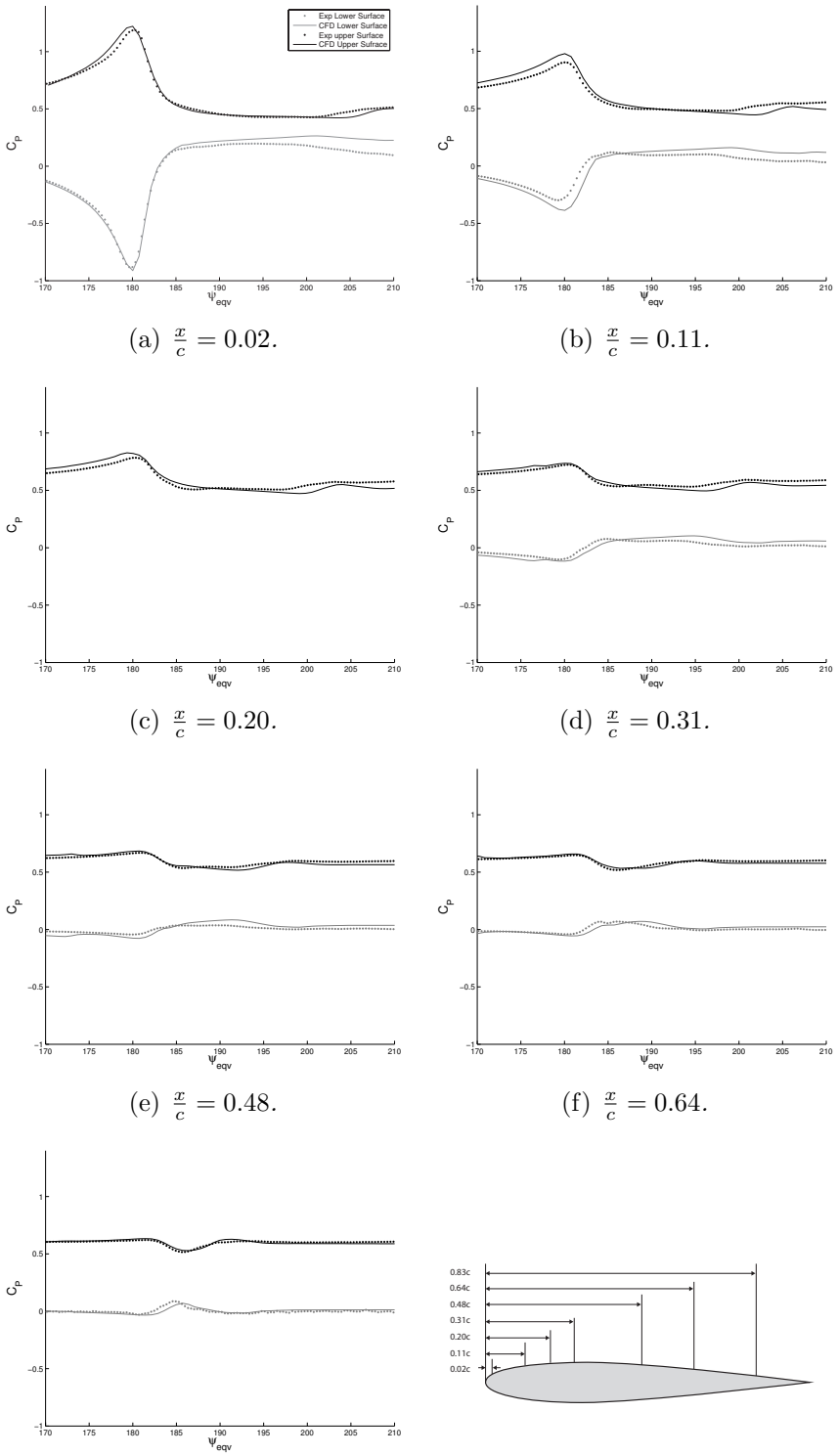

(a) $\frac{x}{c} = 0.02$. (b) $\frac{x}{c} = 0.11$.

(c) $\frac{x}{c} = 0.20$. (d) $\frac{x}{c} = 0.31$.

(e) $\frac{x}{c} = 0.48$. (f) $\frac{x}{c} = 0.64$.

(g) $\frac{x}{c} = 0.83$. (h) *Surface pressure locations.*

Figure 3.7: *Aerofoil Surface C_P during a strong AVI for various chordwise location on the upper and lower surface.* $\frac{y_v}{c} = 0.0$. *Upper surface C_P offset by* $+0.6$

primary BVI wave, and travels at approximately the sum of the local rotor speed and the speed of sound.

Shortly after the primary BVI wave, the *convective event* is seen. This is associated with the chordwise passage of the vortex structure as it moves from the leading edge to the trailing edge of the aerofoil, and is seen in both the upper and lower surface of a strong interaction, but only the lower surface of the weak interaction. This is due to the vortex passing below the blade for the weak interaction, closer to the lower side, which shields the upper side.

When the vortex core passes the trailing edge, a new wave is seen to propagate from the trailing edge to the leading edge of the aerofoil. This wave is likely the result of the re-establishment of the Kutta condition, and is commonly known as the *secondary BVI wave*, or sometimes the *Kutta wave* [83]. Located between the primary and secondary BVI waves is a plateau of relatively steady pressure. The propagation of the waves has been noted in the analysis of the experimental data previously [83] and in the present analysis, these events are accurately represented.

3.2.3 Flow Field

The flow field of the 2D AVI reveals the distortion of the vortex and the propagation of the acoustic waves from the blade surface. The simulation of the weak interaction is shown in Fig. 3.10 where the perturbation pressure is shown as contour colours, and the position of the vortex is revealed with contour lines of vorticity. As the vortex approaches the blade, the vortex induced lift increases. When the vortex passes below the leading edge of the blade, this lift rapidly diminishes as the primary acoustic wave propagates along the aerofoil. As this occurs, a strong acoustic pulse is radiated into the flow. The vortex then passes the trailing edge of the aerofoil where the secondary Kutta wave propagates from the trailing edge to the leading edge of the aerofoil. As this reaches the leading edge of the aerofoil, a secondary acoustic wave is radiated. The vortex structure remains largely intact during this interaction as the core passes well

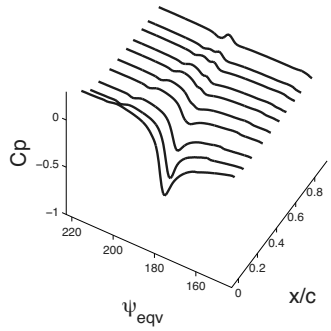

(a) *CFD results of lower surface pressure.*

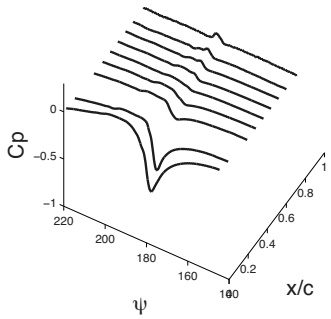

(b) *Experimental results of lower surface pressure.*

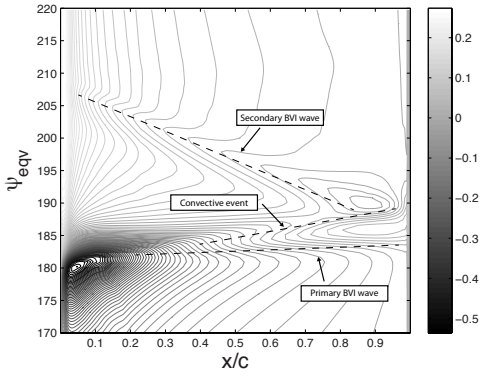

(c) *CFD results detailing the wave propagation on the lower surface of the aerofoil.*

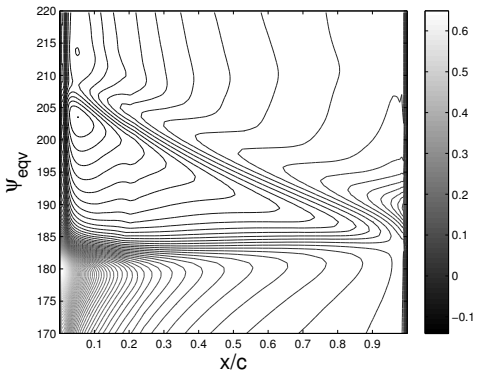

(d) *CFD results detailing the wave propagation on the upper surface of the aerofoil.*

Figure 3.8: *Surface pressures during weak AVI.*

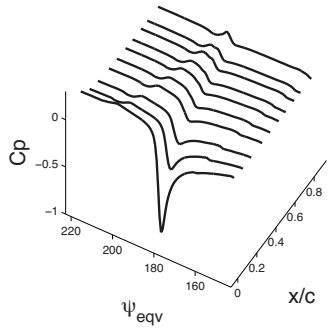

(a) *CFD results of lower surface pressure.*

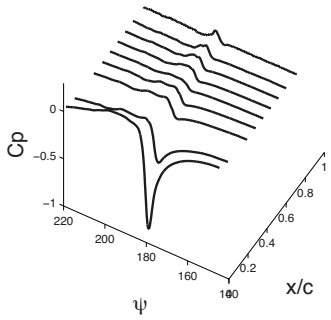

(b) *Experimental results of lower surface pressure.*

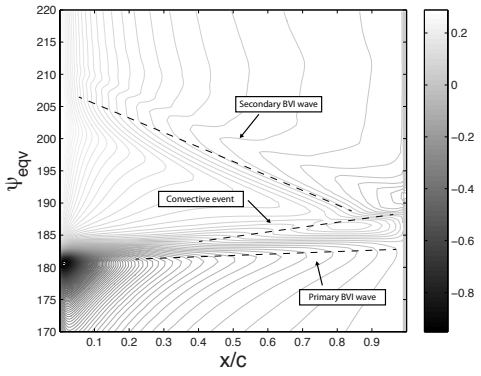

(c) *CFD results detailing the wave propagation on the lower surface of the aerofoil.*

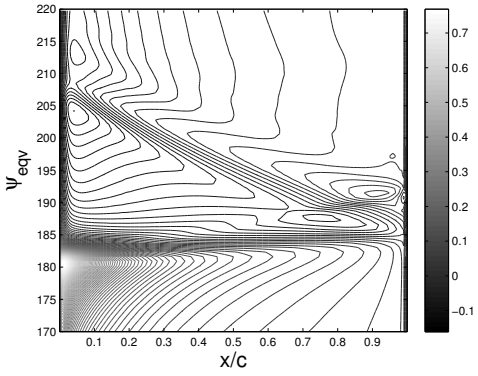

(d) *CFD results detailing the wave propagation on the upper surface of the aerofoil.*

Figure 3.9: *Surface pressures during strong AVI.*

below the blade surface.

The flow field of the strong interaction is shown in Fig. 3.11. The mechanisms of the interaction are the same as the weak interaction, but the induced lift and the acoustic waves radiated are stronger. The vortex core is also bisected during the interaction with the aerofoil and the passage of the vortex cores is responsible for the convective wave seen in Fig. 3.9. Due to the sense of rotation in the vortex, the two halves of the vortex core pass over the aerofoil at different speeds and leave the trailing edge of the aerofoil at separate times. However, these two sections of the core can be seen to reform a vortex structure after the interaction.

3.2.4 Grid Convergence

To confirm grid convergence for the AVI computations, the strong interaction simulation is performed on three different meshes of varying resolution as shown in Table 3.2, where mesh points across the vortex core are used as a convenient measure of mesh resolution. These are denoted high, medium and low resolution, and the surface pressures at the leading edge of the aerofoil during the interaction are shown in Fig 3.12.

The medium and high resolution results are almost identical indicating that grid convergence has been achieved. The low resolution solution underpredicts the strength of the pressure pulse. This is to be expected, as it was shown previously that the vortex strength could not be adequately preserved using only 4 mesh points across the vortex core. Diffusion of the vortex strength will result in an underprediction of the magnitude of the surface pressures.

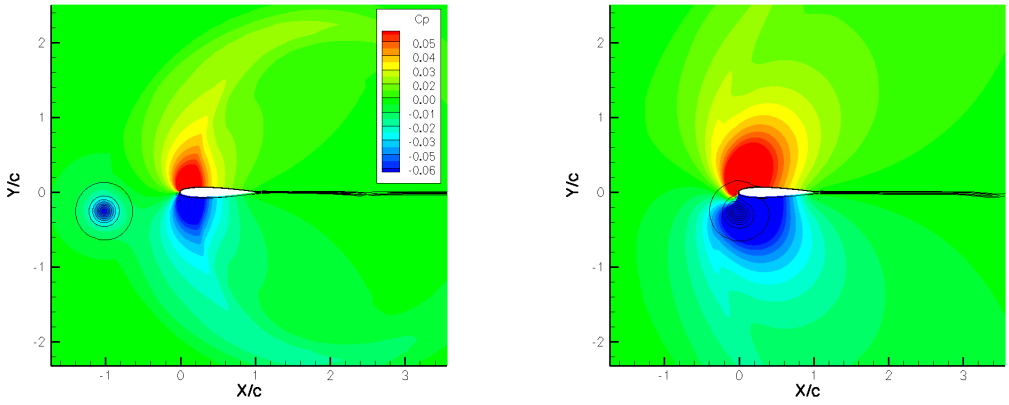

(a) $\psi_{eqv} = 171°$ (b) $\psi_{eqv} = 180°$

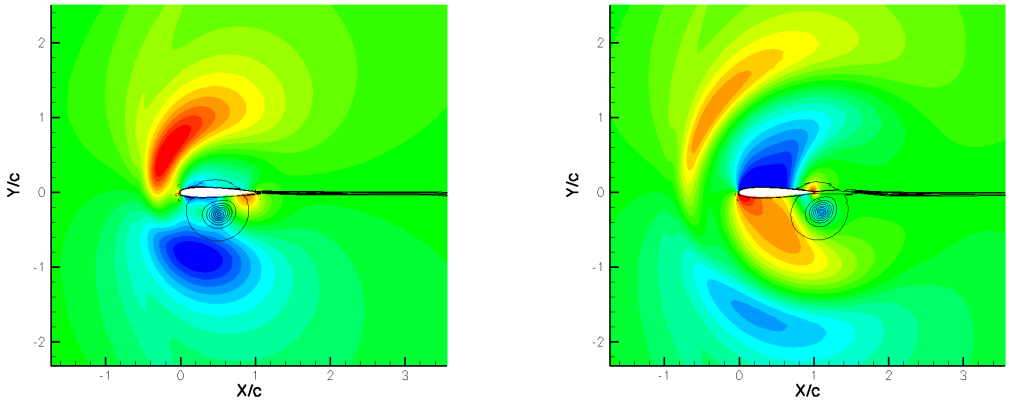

(c) $\psi_{eqv} = 185°$ (d) $\psi_{eqv} = 190°$

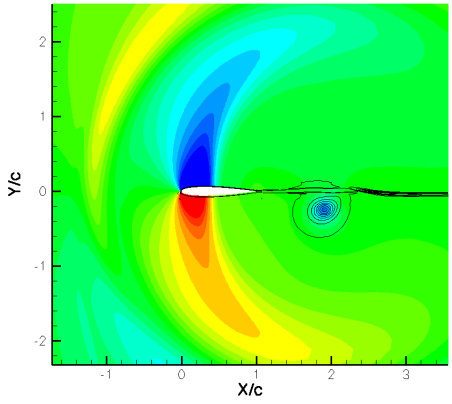

(e) $\psi_{eqv} = 197°$

Figure 3.10: *Weak AVI flowfield. Contour colours show perturbation C_P, contour lines show vorticity.*

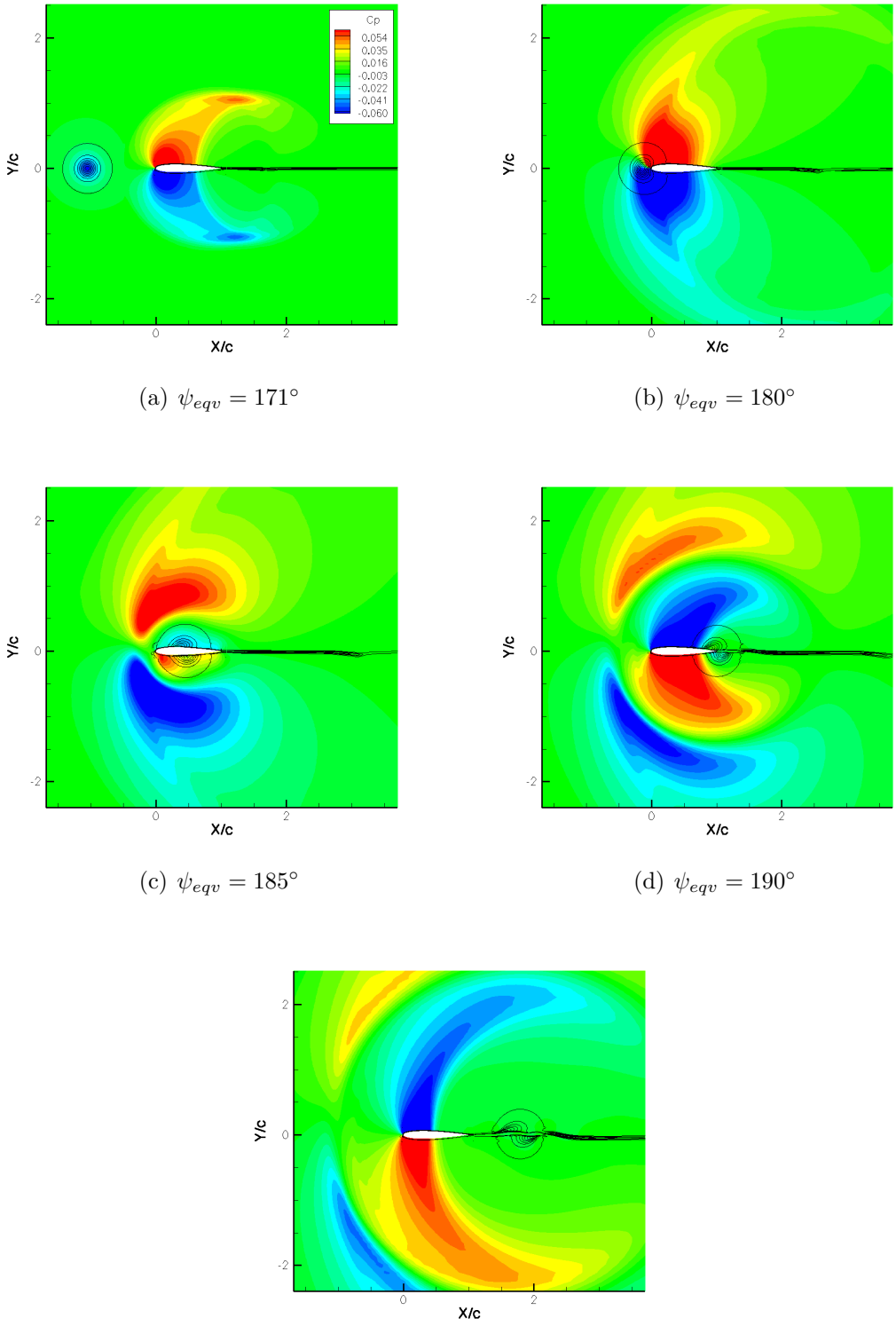

(a) $\psi_{eqv} = 171°$

(b) $\psi_{eqv} = 180°$

(c) $\psi_{eqv} = 185°$

(d) $\psi_{eqv} = 190°$

(e) $\psi_{eqv} = 197°$

Figure 3.11: *Strong AVI flowfield. Contour colours show perturbation C_P, contour lines show vorticity.*

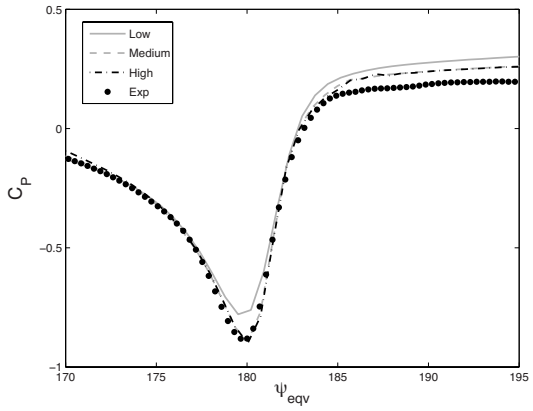

Figure 3.12: *AVI simulation performed on three resolution meshes.*

3.2.5 Comparison with Indicial Method

The indicial approach is a linear analysis method to compute the aerodynamic response to a wide variety of unsteady flow conditions, and has previously been used for the analysis of AVIs [22, 23]. In brief, if the step response is known for a unit input, then the aerodynamic response to an arbitrary input can be found by Duhamel superposition. For an AVI, the effect of the vortex can be represented as a combination of vertical gust functions. The response of a flat plate (or a thin aerofoil) penetrating a uniform vertical gust in incompressible flow is known analytically through the Küssner function. For purposes of computational simplicity, exponential approximations of this functions are used. The response of an aerofoil subject to an arbitrary vertical gust can be calculated from:

$$\begin{aligned}
\Delta C_l(t) &= \frac{C_{l\alpha}}{\beta}\frac{1}{U_\infty}\left[v(s) - Z_1(s) - Z_2(s)\right] \\
Z_1(s) &= Z_1(s-\Delta s)e^{-g_1\beta^2\Delta s} + G_1[v(s) - v(s-\Delta)]e^{-\frac{1}{2}g_1\beta^2\Delta s} \\
Z_2(s) &= Z_2(s-\Delta s)e^{-g_2\beta^2\Delta s} + G_2[v(s) - v(s-\Delta)]e^{-\frac{1}{2}g_2\beta^2\Delta s}
\end{aligned} \tag{3.4}$$

G_1	0.670
G_2	0.330
g_1	0.1735
g_2	1.637

Table 3.3: *Deficiency function coefficients for indicial calculations.*

where $C_{l\alpha}$ is the incompressible lift slope of the aerofoil, s is the distance travelled by the aerofoil in semi-chords, v is the vertical velocity experienced by the aerofoil at its quarter chord point and β is Glauert's compressibility factor, $\sqrt{1-M^2}$. Z_1 and Z_2 are deficiency functions containing the time history information of the unsteady aerodynamics needed to account for the effect of the wake of the aerofoil. This is calculated one-step recursively and the coefficient values g_1, g_2, G_1 and G_2 used to compute the deficiency functions are given in Table 3.3. These coefficients were found using CFD analysis performed by Singh and Baeder [84].

The indicial method is based on the fundamental principle that the flow can be linearised with respect to the forcing function. For AVIs, the forcing function is the vortex and this linearisation is justified for weak interactions, where the passage of the aerofoil does not have a significant effect on the vortex structure. However, if the vortex structure is altered by the interaction, then this linearisation is no longer strictly valid.

To assess the limitation of the indicial method, it is compared against the results of the CFD solver. The results of an indicial calculation of an AVI are shown in Fig. 3.13, where the magnitude of the C_l change and the change of its gradient are labelled ΔC_l and $\Delta\chi$ respectively. These quantities are used to compare the CFD and indicial methods over a range of aerofoil-vortex miss distances, where the flow conditions and the vortex are the same as in section 3.2.2. The results are shown in Fig. 3.14, where the aerofoil-vortex miss distance ranges from $-0.75c$ to $0.75c$.

In general, the indicial method can predict the change in lift, ΔC_l, and the change of its gradient, $\Delta\chi$, well over a range of aerofoil-vortex miss distances. The interaction is

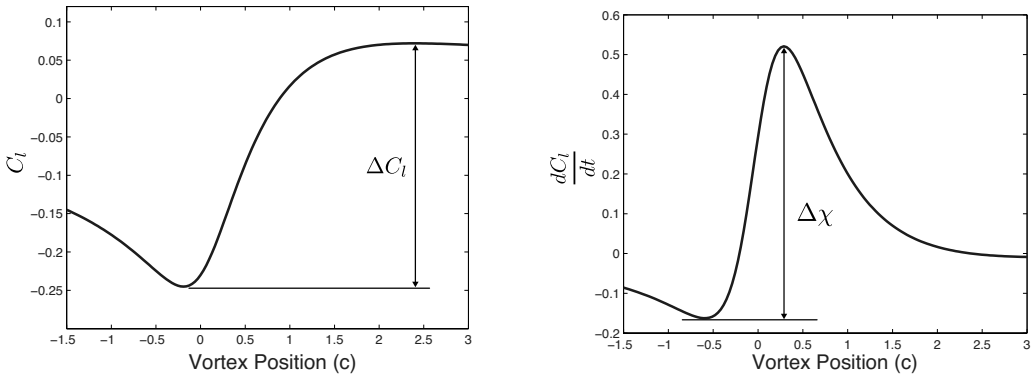

(a) C_l (b) $\frac{dC_l}{dt}$

Figure 3.13: *Measures of the interaction strength. Vortex position is relative to the leading edge of the aerofoil.*

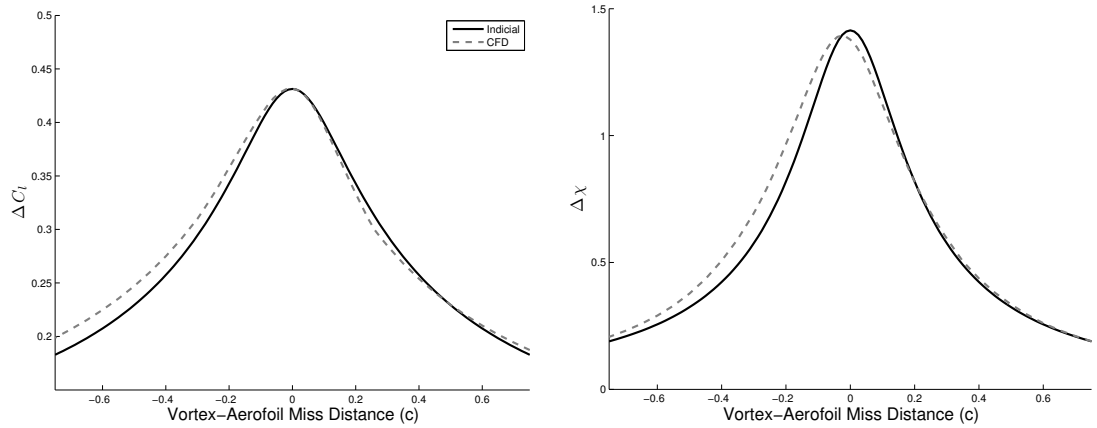

(a) ΔC_l (b) $\Delta\chi$

Figure 3.14: *Indicial and CFD results over various aerofoil-vortex miss distances. Vortex core:* $\bar{r}_v = 1.62$*, freestream velocity:* $M_\infty = 0.626$

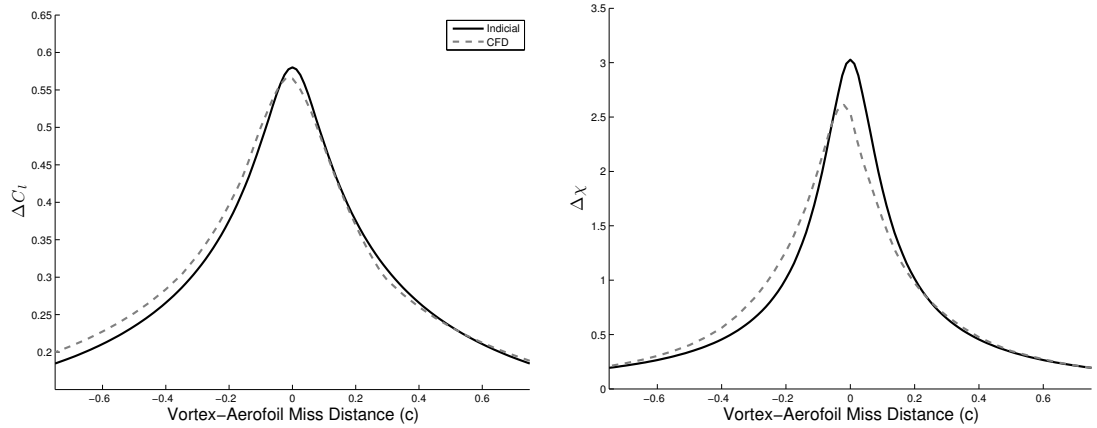

(a) ΔC_l (b) $\Delta\chi$

Figure 3.15: *Indicial and CFD results over various aerofoil-vortex miss distances. Vortex core:* $\bar{r}_v = 0.81$*, freestream velocity:* $M_\infty = 0.626$

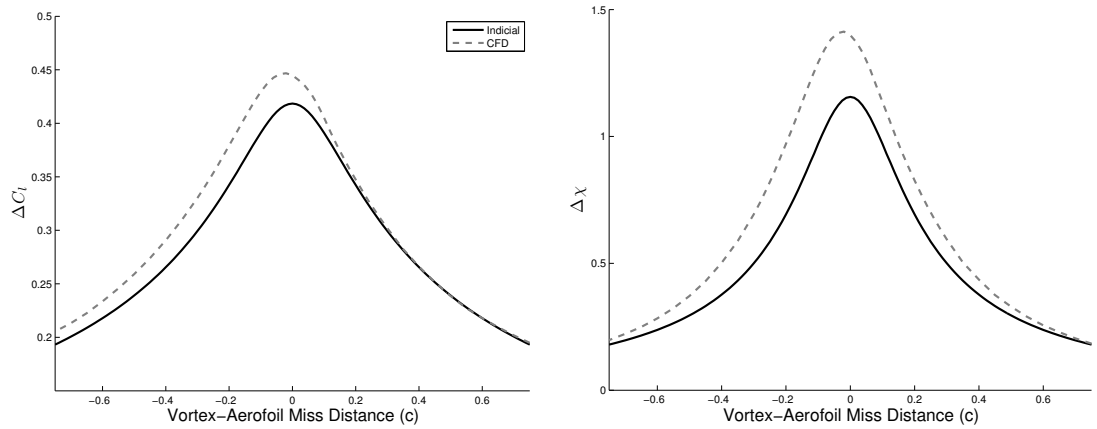

(a) ΔC_l (b) $\Delta\chi$

Figure 3.16: *Indicial and CFD results over various aerofoil-vortex miss distances. Vortex core:* $\bar{r}_v = 1.62$*, freestream velocity:* $M_\infty = 0.8$

even well predicted for stronger interactions with small aerofoil-vortex miss distances, where the vortex structure is severely altered by the aerofoil. This is a surprising result, as this deformation of the vortex structure is not accounted for by the indicial model, yet both ΔC_l and $\Delta\chi$ are well predicted.

However, the indicial method does not compare as well if the vortex core size is reduced, producing a more concentrated vortex. A comparison of the indicial and CFD results is shown in Fig. 3.15, where the vortex core size is reduced to $\bar{r}_v = 0.81$, half the core radius of the vortex used in the experimental study of Caradonna *et al.* The two methods agree well for the computed ΔC_l, however, for small aerofoil-vortex miss distances the indicial method predicts a much more impulsive interaction, as $\Delta\chi$ is overpredicted by approximately 17% for the strongest interaction. The gradient of the lift is an important quantity for the calculation of the far-field acoustics, so this overprediction of $\Delta\chi$ will produce a similar overprediction of the aeroacoustics radiated from the interaction. Accurate modelling of the dynamics of the vortex as it interacts with the aerofoil are needed to predict this change in lift accurately. It should be noted that the vortex generator wing used in the BVI experiments performed by Caradonna *et al.* had a chord three times larger that the rotor chord producing a vortex that is nominally three times larger than that involved in a realistic interaction, where the vortices are generated by the rotor blades. Therefore, a smaller core-size can be expected in realistic situations, and for these cases the indicial method could potentially predict unrealistic lift values for the interaction.

Increasing the free stream Mach number of the interaction introduces nonlinear aerodynamic effects as the flow becomes transonic, and these effects are also neglected by the indicial method. The interaction of the original vortex used in the experimental study of Caradonna *et al.* but at a higher freestream velocity of Mach 0.8 is shown in Fig. 3.16. For this increased freestream velocity, the indicial method cannot accurately predict the strong interactions due to the nonlinear flow effects, and both ΔC_l and $\Delta\chi$ are underpredicted.

It is also apparent that the indicial results are symmetric around the zero aerofoil-vortex miss distance point but that the CFD results are slightly offset, especially for

stronger interactions, where the maximum ΔC_l and $\Delta\chi$ occur at a aerofoil-vortex miss distance less than zero for all the cases shown. This offset of the results means that an interaction with a positive aerofoil-vortex miss distance is weaker and less impulsive that the same interaction with the opposite, negative, aerofoil-vortex miss distance. This offset is due to the velocity component induced by the vortex that is parallel to the freestream velocity, which influences the interaction in two ways. Firstly, this velocity component alters the angle of attack. For the interactions examined here, as the vortex passes below, the aerofoil experiences an increase in freestream velocity. This increase will act to reduce the angle of attack and therefore reduce the strength of the interaction. This effect will shift the interaction results shown in Figs. 3.14–3.16 to the right, in the opposite direction as the offset seen for the CFD results. Also, this addition to the freestream velocity from the vortex will change the strength of the interaction, as the lift force produced is proportional to U_∞^2. As the vortex passes below the aerofoil, the increase in freestream velocity produces a stronger interaction. This increase in interaction strength is greater than the aforementioned reduction caused by the angle of attack decrease, and results in a shift to the left of the interaction results shown in Figs. 3.14–3.16. The combined effect of this freestream vortex velocity component causes the results to be offset from the zero aerofoil-vortex miss distance point, and is not accounted for by the indicial method.

3.3 3D Blade-Vortex Interaction Study

The previous section shows that the important flow physics of a parallel BVI are essentially two dimensional in nature, and that the current computational methodology is capable of accurately computing the interaction, given sufficient spatial resolution. This is an ideal initial validation of the method, due to its relative simplicity, however a realistic BVI is highly three-dimensional. This section will deal with applying the current methodology to model the experimental data fully in three dimensions. This will include resolving the vortex formation at the tip of the vortex generator wing, evaluating the ability of overset meshes in relative motion to resolve the vortex structure, and resolving the interaction of a rotor blade with the tip vortex.

3.3.1 Steady Vortex Formation

The present work attempts to fully model the parallel BVI experiment of Caradonna *et al.* [19]. As shown in Fig. 3.2, the experiment involved the interaction of a blade with a steady vortex formed upstream from a static vortex generator wing. To simulate this interaction accurately, the vortex formation must be accurately resolved and the requirements for the current methodology to do this are examined here.

The vortex generator consists of a NACA 0015 aerofoil section on an untwisted rectangular planform wing. This is discretised by a C-O topology mesh with $209 \times 60 \times 51$ mesh points in the chordwise, spanwise and wall normal direction respectively. The vortex generator has an aspect ratio of 2.4 and is inclined at an angle of attack of 12° to the freestream of Mach 0.142, matching the experimental setup. The vortex generator is overset onto a Cartesian background mesh with dimensions of $296 \times 173 \times 135$ in the freestream, cross-stream and vertical directions respectively. The mesh spacing is refined in the region of vortex convection to 8 points across the vortex core, and the entire mesh is illustrated in Fig. 3.17(a).

The simulation is performed until a steady solution is obtained and this is shown in Fig. 3.17(b) where isosurfaces and contours of streamwise vorticity reveal the vortex rollup process. The vortex velocity profile is shown in Fig. 3.17(c) with a comparison to the experimental data fit of equation 3.1, and the computed results are in good agreement with the experimental data. The vortex sheet roll up can also be seen in the velocity profile data as a small kink in the velocity profile outside of the vortex core region.

The vortex strength, defined as the maximum tangential velocity difference across the vortex profile, and the vortex core size, defined as the distance between the maximum and minimum velocity location, are shown in Fig. 3.18. The experimental data fit was taken at a location of approximately 3 c_{VG} downstream of the trailing edge, and the computed vortex core size and velocity is seen to closely approach the experimental data at this point.

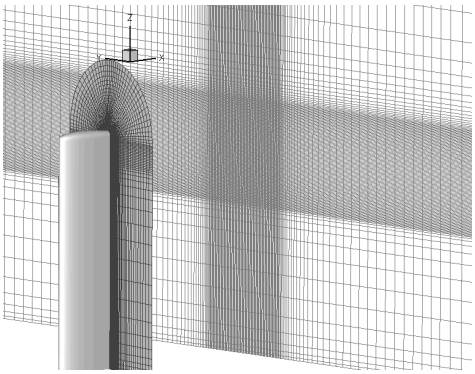

(a) *Mesh system of static vortex generator.*

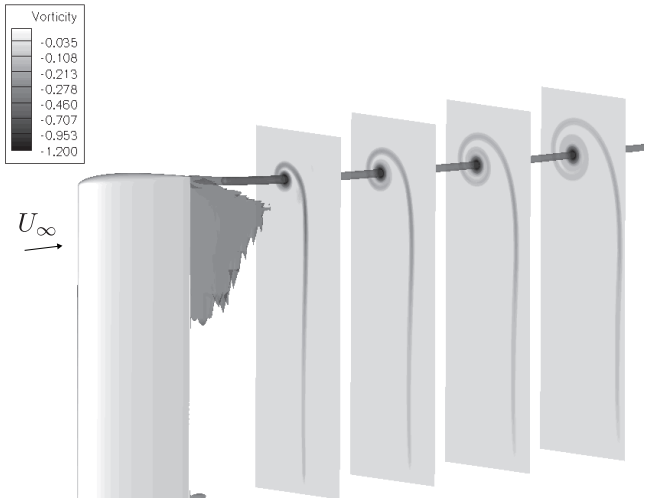

(b) *Sample solution of steady vortex showing contours and an isosurface of streamwise vorticity. Planes shown are at $1c_{vg}$, $2c_{vg}$, $3c_{vg}$ and $4c_{vg}$ downstream of the trailing edge*

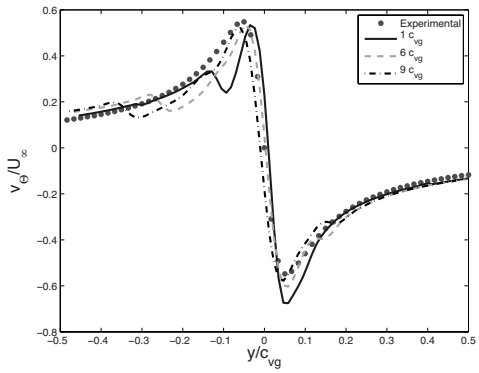

(c) *Velocity profile of vortex downstream of vortex generator.*

Figure 3.17: *Steady vortex swirl velocity compared to experimental data fit measured at $3C_{VG}$ downstream of the trailing edge of the vortex generator.*

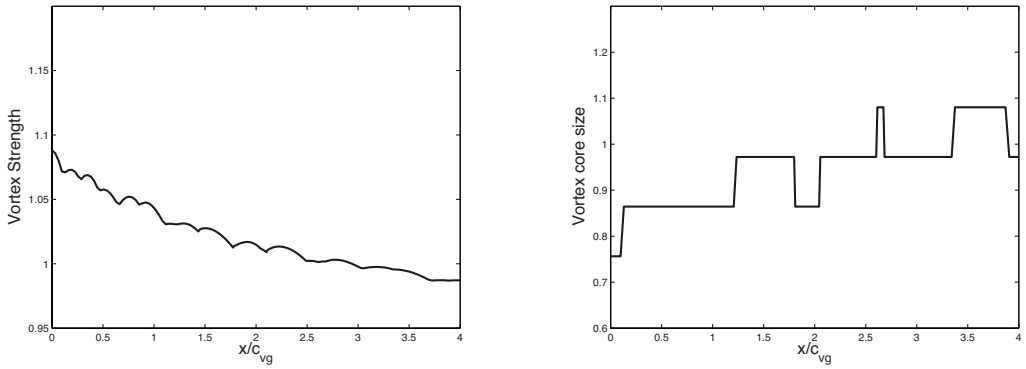

(a) *Peak-to-peak velocity of vortex. Normalised by experimental data fit value.*

(b) *Core size of vortex. Normalised by experimental data fit value.*

Figure 3.18: *Steady vortex velocity and core size.*

3.3.2 Moving Overset Mesh Evaluation

To perform a full simulation of the BVI, the rotor blade mesh will be overset onto the background Cartesian mesh downstream of the vortex generator, and this rotor blade mesh will rotate within the static background mesh. The flow solution is interpolated from the background mesh to the rotor blade mesh through its boundary points. The structure of the vortex must be preserved as it is passed into a moving overset mesh.

The ability of the code to accurately pass flow information from the static background mesh into the rotating mesh is now evaluated. A static vortex is first formed upstream, as detailed in section 3.3.1. The steady vortex convects downstream where a rotating box mesh is placed in the domain as shown in Fig. 3.19. This box mesh rotates at the same angular velocity as the rotor in the experimental setup and has a spatial resolution comparable to the fine vortex region of the background mesh, with 8 points across the vortex core. The box mesh contains no wall surfaces and the solution is interpolated to the box mesh through its boundary points. The solution is not interpolated from the box mesh, and therefore it has no influence on the rest of the solution domain. Ideally, the vortex profile will be passed into the box mesh, and remain the same as the static vortex in the background mesh, any differences between the solution can be attributed to interpolation error and numerical error caused by the

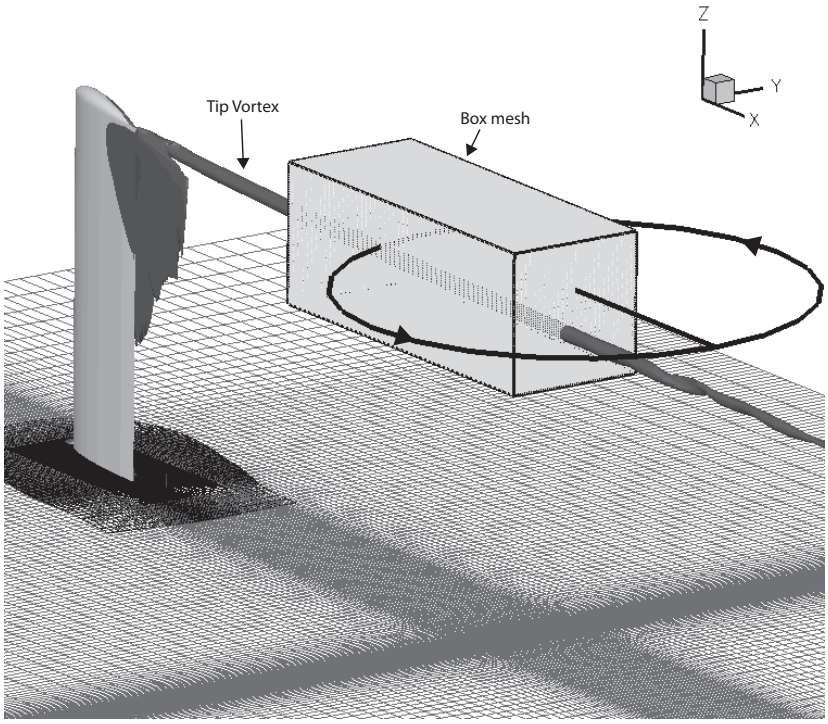

Figure 3.19: *Rotating box mesh system.*

vortex convecting through the moving mesh. This allows both the size of the timestep and the accuracy of the time integration needed to be evaluated.

Once the steady vortex has formed, the box mesh is rotated through 1 revolution, and the velocity of the vortex is extracted at a location close to the tip of the box mesh, as this is where the distortion of the vortex is most apparent. The vortex velocity in the box mesh and the background mesh is shown in Fig. 3.20 for various timesteps and time integration accuracies. The timestep values correspond to the discrete steps of angular rotation of the box mesh. It is observed that the vortex profile can suffer considerable diffusion as it convects through the box mesh; the peak-to-peak velocity decreases and the vortex core expands.

The use of a first order backward Euler time integration scheme is seen to be highly diffusive. The results are improved by reducing the timestep, yet even for the finest

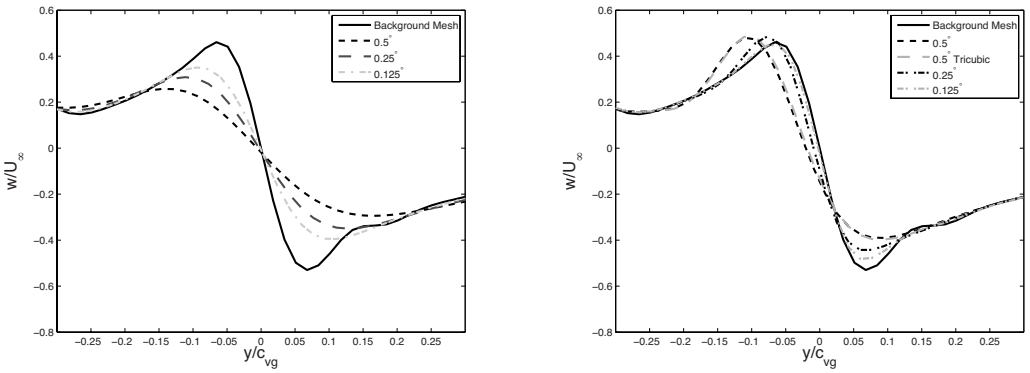

(a) *First order backward Euler time integration.*

(b) *Second order backward differencing time integration*

Figure 3.20: *Vortex velocity profiles.*

timestep tested of $dt = 0.125°$, the vortex is still largely underpredicted. The second order backward differencing time integration scheme is much more capable of preserving the vortex structure over the range of timesteps tested, and the correct velocity profile is almost fully recovered at $dt = 0.125°$ using this scheme.

The accuracy of the interpolation of flow information at the mesh boundaries is also increased by using a tricubic interpolation scheme. For a tricubic interpolation, a stencil of 64 donor points is used to interpolate the solution. This has a beneficial, but very small effect on the resulting vortex properties. This scheme results in an increase in the data that is passed between the CPUs on which the simulation is performed, producing a significant increase in computational time. Therefore a first order interpolation of data is used in the present work.

3.3.3 3D BVI Results

The grid and time integration requirements have been assessed to accurately simulate the vortex formation and its interpolation into a moving mesh. To simulate a full parallel 3D BVI, the rotor blade must now be introduced into the simulation.

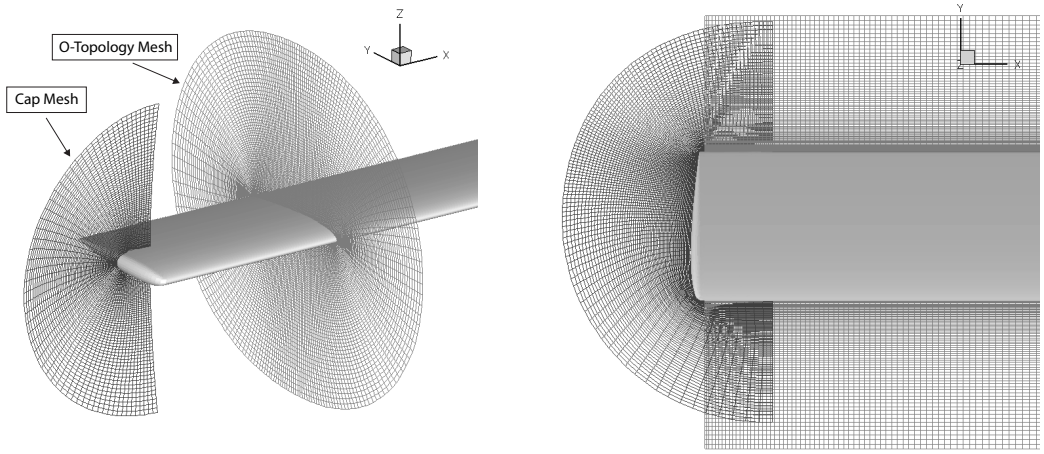

(a) (b)

Figure 3.21: *Details of the two meshes used to discretise the near blade domain.*

Mesh	Topology	Dimensions	Total Points
Vortex Generator	C-O	209×60×51	639,540
Background	Cartesian	296×173×135	6,913,080
Blade	O	187×157×73	2,143,207
Cap	-	111×64×70	497,280
		Total Points	10,058,760

Table 3.4: *Number of cells in BVI meshes.*

The rotor blade is discretised using 2 structured meshes. The majority of the blade span is represented by an O topology mesh, where the O topology planes are stacked in the spanwise direction. The tip of the rotor blade is represented by a cap mesh and its position and topology is illustrated in Fig. 3.21. The advantages of using this combination of meshes is that it produces high mesh quality in the region where the vortex is interpolated into the rotor meshes, which results in the minimum diffusion of the vortex structure. Other mesh topologies, such as the C-O topology used to represent the vortex generator, produce a region where the planes collapse close to the leading edge at the tip of the blade. This will produce a region of low mesh quality, which would have a detrimental effect on the vortex profile as it convects through blade mesh. The mesh dimensions are summarised in Table 3.4.

The simulation is first performed with a static rotor until a steady vortex has formed from the vortex generator. Once a steady vortex has formed, the blade mesh is rotated with a tip velocity of Mach 0.715. As indicated by the previous overset mesh evaluation, a timestep of 0.125° is used with 15 sub-iterations and the flow residual was seen to drop over two orders of magnitude every timestep. This timestep preserves the vortex as it is interpolated across the mesh boundaries, but is also required for the stability of the 5^{th} order WENO scheme with second order accurate time integration, as larger timesteps produced spurious oscillations in the regions of the blade mesh with the highest local CFL numbers. The simulation is performed for 3 rotor revolutions and data is collected on the last revolution. The surface pressure at various chord locations for the upper and lower surface is shown in Fig. 3.22 for the weak interaction case and Fig. 3.23 for the strong interaction case. The upper surface data has been offset by +0.6 for clarity.

The surface pressures for both the weak and strong interactions are resolved well, indicating that the vortex dynamics has been accurately computed. In both cases, the gradient of the pressure pulse has been slightly underpredicted. This is most prominent at the leading edge of the aerofoil where the pressure change is greatest. The gradient of the pressure is an important parameter as it is directly proportional to the acoustics radiated to the far-field. This slight underprediction is most likely due to the strength of the vortex slightly diffusing as it moves through the blade mesh.

The flow field of the interactions is shown in Fig. 3.24 for the weak interaction, and Fig. 3.25 for the strong interaction. An isosurface reveals a constant density level surrounding the blade as it interacts with the vortex. Also shown is the vorticity at a spanwise plane of 88% radius of the blade, the same location as the surface pressure measurements. As with the 2D AVI simulation, the weak interaction does not severely distort the structure of the vortex, and the vortex core remains intact. This preservation of the vortex structure is evident in the 3D isosurfaces of density shown in Fig. 3.24, where the vortex can still be seen downstream of the interaction. Conversely, during the strong interaction the vortex is bisected by the blade and its structure is considerably altered.

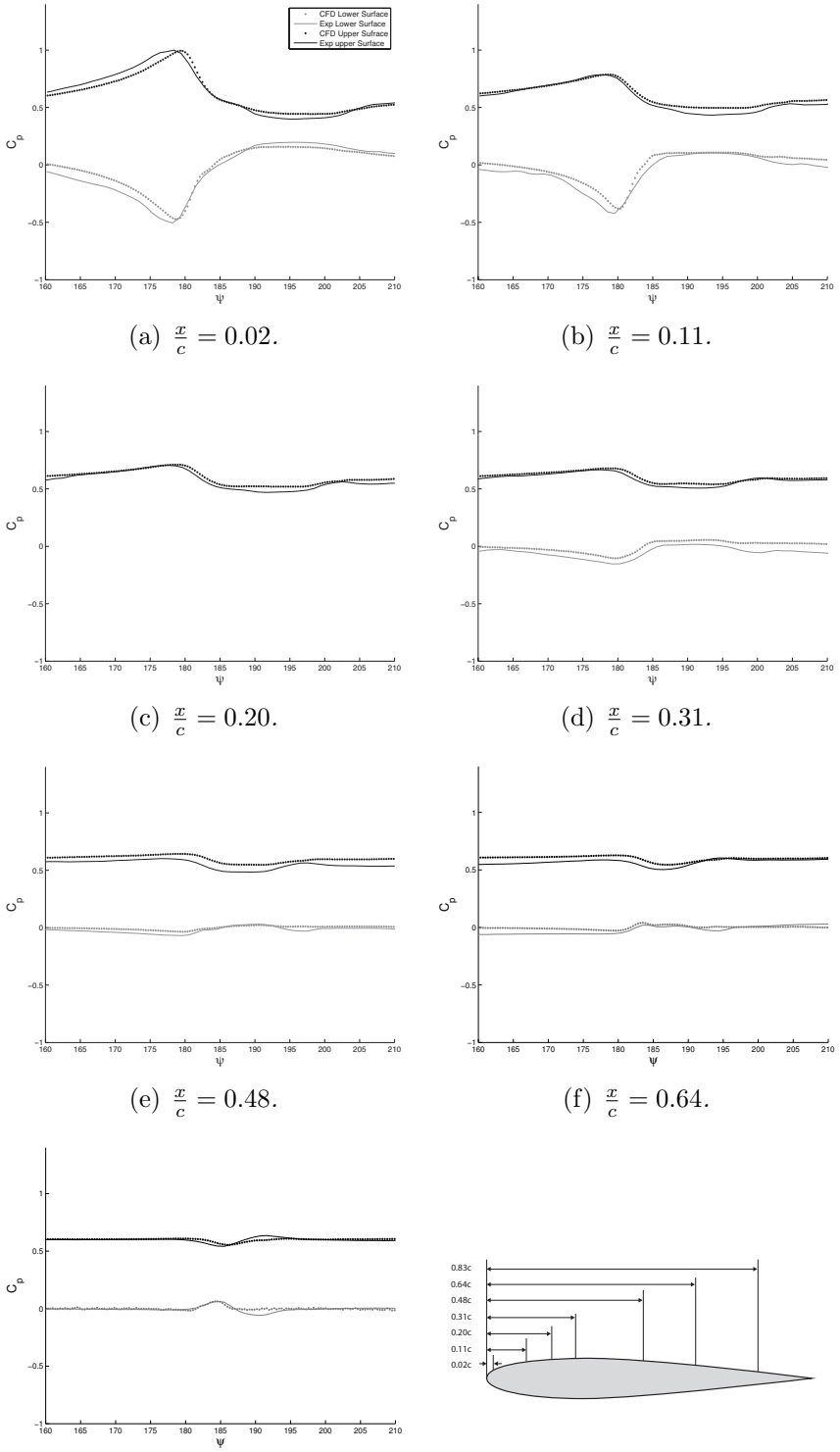

(a) $\frac{x}{c} = 0.02$. (b) $\frac{x}{c} = 0.11$.

(c) $\frac{x}{c} = 0.20$. (d) $\frac{x}{c} = 0.31$.

(e) $\frac{x}{c} = 0.48$. (f) $\frac{x}{c} = 0.64$.

(g) $\frac{x}{c} = 0.83$. (h) *Surface pressure locations.*

Figure 3.22: *Blade Surface C_P during weak BVI for various chordwise location on the upper and lower surface.* $\frac{y_v}{c} = 0.25$. *Upper surface C_P offset by* $+0.6$

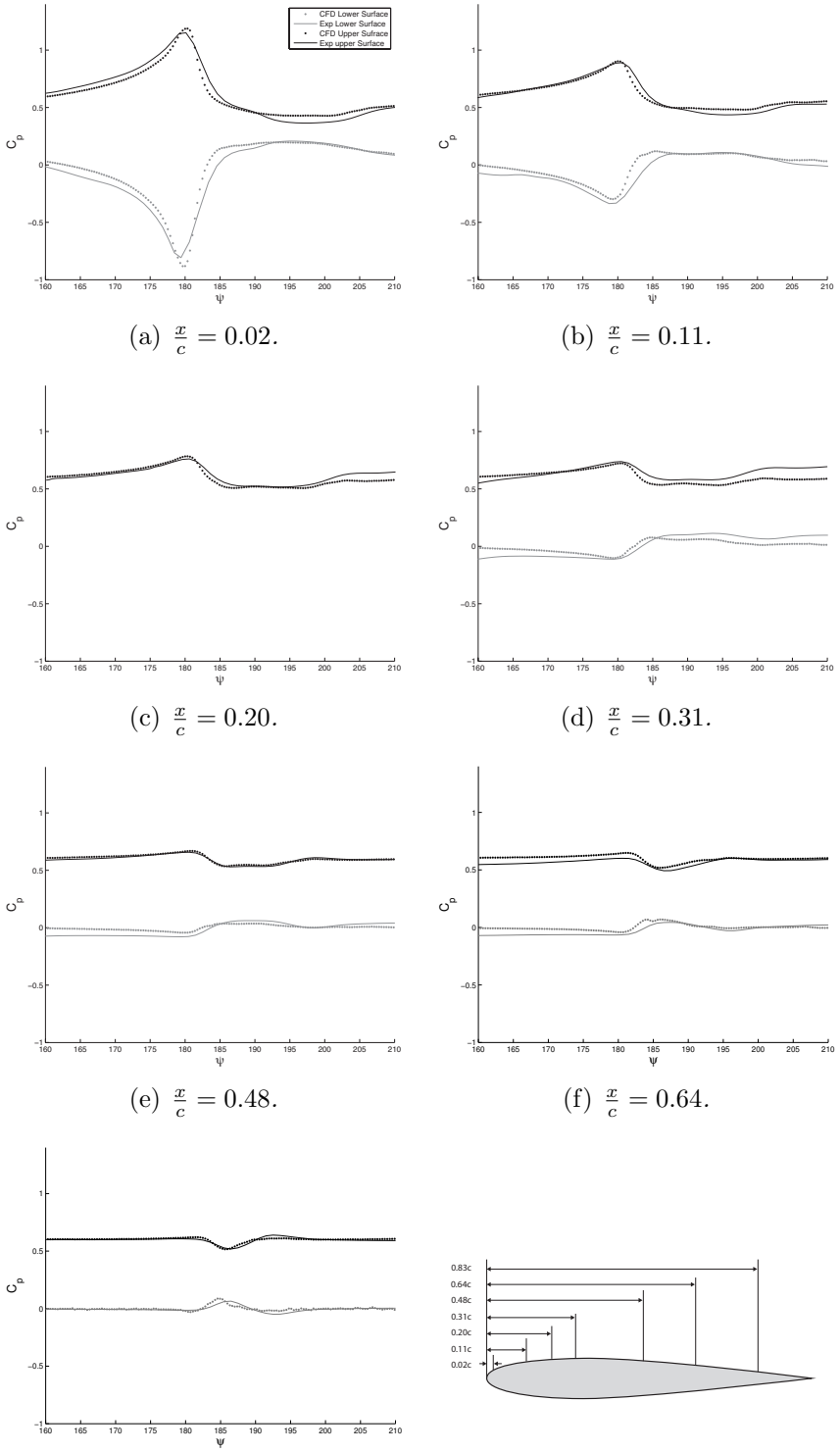

(a) $\frac{x}{c} = 0.02$. (b) $\frac{x}{c} = 0.11$.

(c) $\frac{x}{c} = 0.20$. (d) $\frac{x}{c} = 0.31$.

(e) $\frac{x}{c} = 0.48$. (f) $\frac{x}{c} = 0.64$.

(g) $\frac{x}{c} = 0.83$. (h) *Surface pressure locations.*

Figure 3.23: *Blade Surface C_P during strong BVI for various chordwise location on the upper and lower surface.* $\frac{y_v}{c} = 0.0$. *Upper surface C_P offset by* $+0.6$

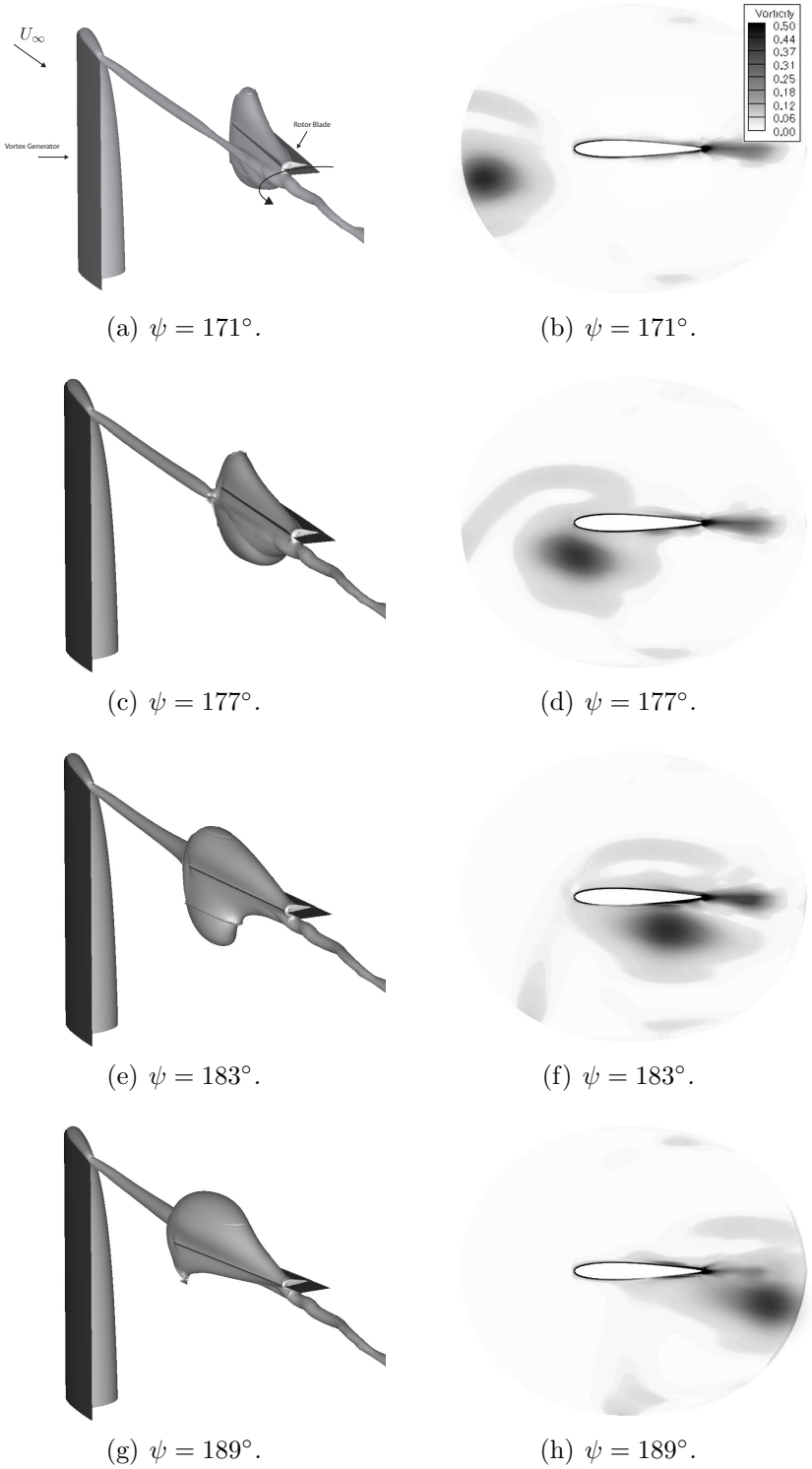

(a) $\psi = 171°$. (b) $\psi = 171°$.

(c) $\psi = 177°$. (d) $\psi = 177°$.

(e) $\psi = 183°$. (f) $\psi = 183°$.

(g) $\psi = 189°$. (h) $\psi = 189°$.

Figure 3.24: *Flowfield during weak BVI, showing an iso-surface of constant density of* $\rho/\rho_\infty = 0.995$*, and contours of vorticity.*

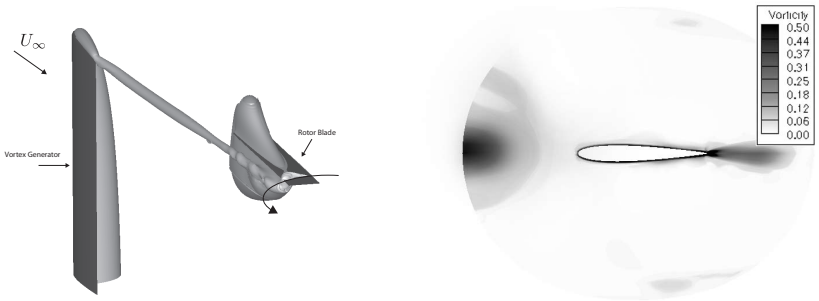

(a) $\psi = 171°$. (b) $\psi = 171°$.

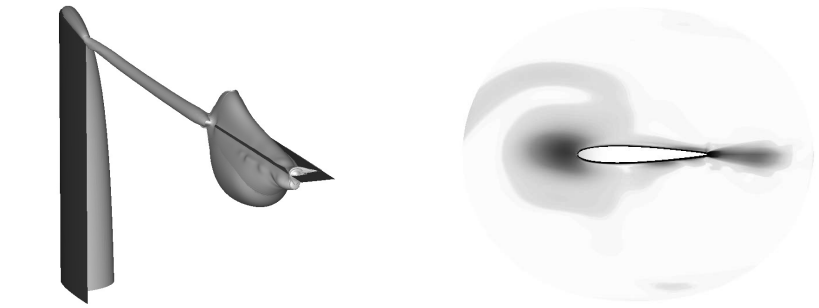

(c) $\psi = 177°$. (d) $\psi = 177°$.

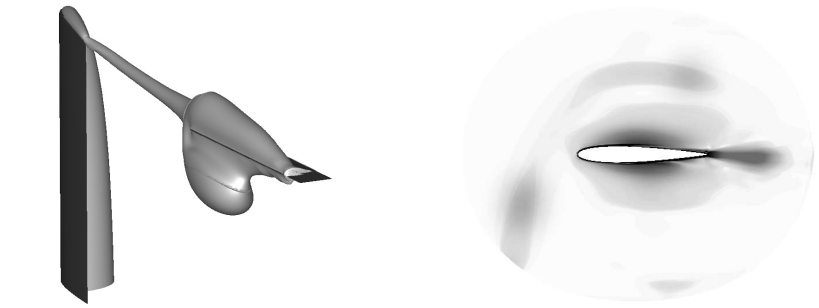

(e) $\psi = 183°$. (f) $\psi = 183°$.

(g) $\psi = 189°$. (h) $\psi = 189°$.

Figure 3.25: *Flowfield during strong BVI, showing iso-surface of constant density of* $\rho/\rho_\infty = 0.995$*, and contours of vorticity.*

3.4 Acoustic Prediction of BVI

A consequence of BVI is the radiation of strong acoustic wave from the rotor. As discussed previously, these acoustic waves are highly impulsive, and radiate out of plane of the rotor towards observers located on the ground. In this section, acoustic predictions are made using the computed blade surface pressures and the linear Ffowcs-Williams Hawkings solver described previously. These predictions are compared with experimental data and the CFD solution. In addition, the directivity of the noise radiated from the interaction is studied.

3.4.1 Near-field Noise Prediction

The experiment obtained acoustic data at two locations in the near-field of the interaction. The position of the microphones are shown in Fig. 3.2 and are located approximately $2c$ below the point of interaction. Acoustic data was taken over 30 rotor revolutions and averaged.

The linear Ffowcs-Williams Hawkings solver uses the blade surface pressures to compute the acoustic pressure at the microphone locations and the results are compared to the experimental data in Fig. 3.26 for the weak interaction, and Fig. 3.27 for the strong interaction. The pressure extracted directly from the CFD solution is also shown for comparison.

The near-field noise computed with the linear acoustic solver differs from the experimental data in both the shape and magnitude of the acoustic pulse. This is most likely because the Ffowcs-Williams Hawkings solver only accounts for noise sources on the surface of the blade, which are the loading and thickness sources, and neglects the off-surface volumetric noise sources. These volumetric noise sources are not in general dominant in the far-field, but can have an influence in the near-field. As a result, there is a slight discrepancy between the near-field acoustic pressures computed using the Ffowcs-Williams Hawkings solver and the experimental data. In contrast,

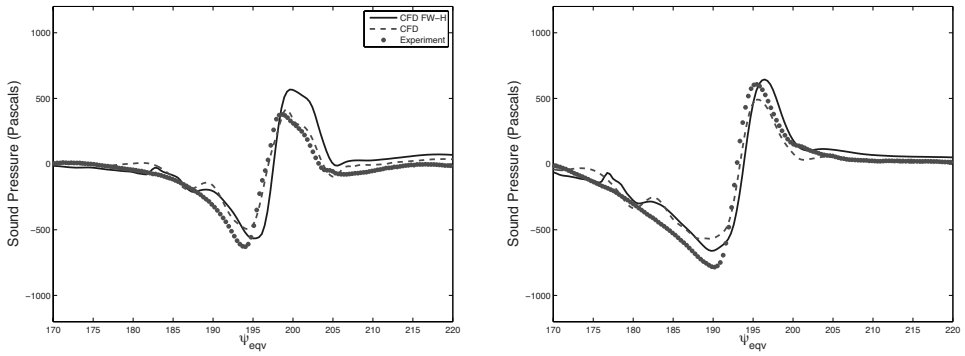

(a) *Microphone 6* (b) *Microphone 7*

Figure 3.26: *Near-field acoustic pulses for weak BVI. CFD with Ffowcs-Williams Hawkings, direct CFD and experimental data shown*

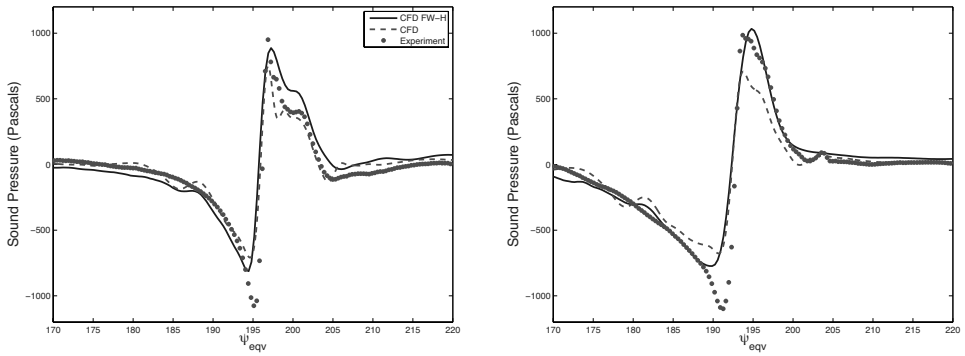

(a) *Microphone 6* (b) *Microphone 7*

Figure 3.27: *Near-field acoustic pulses for strong BVI. CFD with Ffowcs-Williams Hawkings, direct CFD and experimental data shown*

the direct CFD solution naturally represents all the noise sources, and captures the shape of the acoustic pulse well. The magnitude of the pulse is underpredicted though, especially for the strong interaction. In addition to the slight underprediction of the blade surface pressures, this is due to numerical diffusion of the acoustic waves as they propagate outward from the blade surface. The spatial discretisation surrounding the near-field microphone region is the same resolution that is used to preserve the vortex structure, which is approximately equal to 8 mesh points across the vortex core. It is suspected, however, that the accurate preservation of acoustic wave propagation will require greater spatial resolution.

3.4.2 Far-field noise

The acoustic energy that propagates into the far-field for a realistic rotor will be the sound that will be heard by an observer on the ground. In this sense, it is the most important noise to predict for the design of quiet rotors.

The Ffowcs-Williams Hawkings solver is used to predict the acoustics of the 3D BVI simulation and the 2D AVI simulation. To compute the 2D AVI acoustics, the surface pressures computed in section 3.2.2 are mapped onto a 3D blade surface and scaled by the local velocity of the rotor blade, which produces a quadratic spanwise variation in pressure towards the blade tip. This method does not include any tip effects but is justified as the experimental rotor is operated at zero thrust. The number of radial stations used in the mapping was varied until the acoustic solution converged. In the present acoustic analysis, 21 radial stations (with clustering towards the blade tip) are used.

The computed far-field acoustics are shown for the weak interaction in Fig. 3.28, and for the strong interaction in Fig. 3.29. The computed pressures are generally in good agreement with the experimental data. As expected, the strong interaction is slightly underpredicted, due to the underpredicted surface pressures used as inputs for the acoustic solver. The weak interaction is predicted well though in both magnitude and shape. The distinctive kink, which occurs in the pressure pulse immediately after the maximum acoustic pressure, has also been captured. This kink is present in the both BVI cases, but is most prominent in the strong BVI and shows the detail of the acoustic waves that can be predicted. The two dimensional nature of the interaction is also apparent as the 2D AVI pressures are capable of predicting the acoustics to a similar level of accuracy as the full 3D BVI predictions.

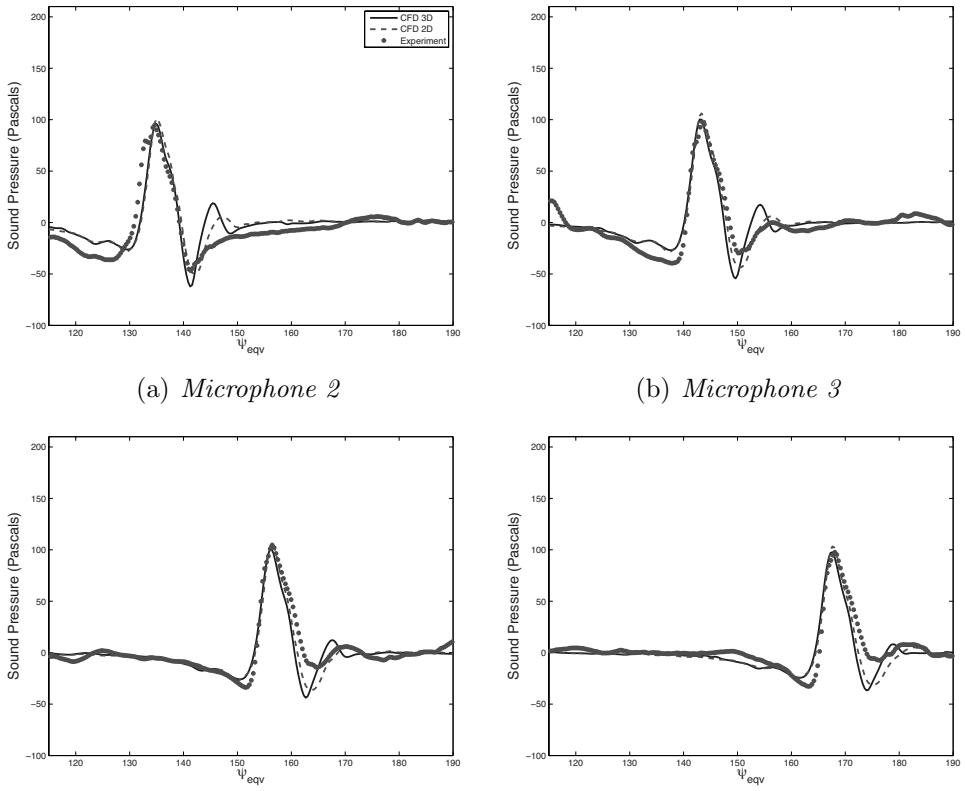

(a) *Microphone 2* (b) *Microphone 3*

(c) *Microphone 4* (d) *Microphone 5*

Figure 3.28: *Far-field noise prediction for weak BVI.*

3.4.3 Noise Propagation

The acoustic waves radiated from the interaction are highly directional. As previously discussed, thickness noise, which is caused by the blade displacing fluid as it rotates, is largely radiated in the rotor plane. Conversely, the loading noise caused by a BVI tends to radiate largely out of the rotor plane. To show this directivity, the noise at various angles beneath a strong interaction is shown in Fig. 3.30 at a span location of $0.88R$, which is computed using the Ffowcs-Williams Hawkings solver. The acoustic energy is shown at two radial locations from the interaction: a location in the near-field at $0.2R$, and a location in the far-field at $1R$.

At the shallow angles close to the plane of the rotor for a radial location of $0.2R$, the

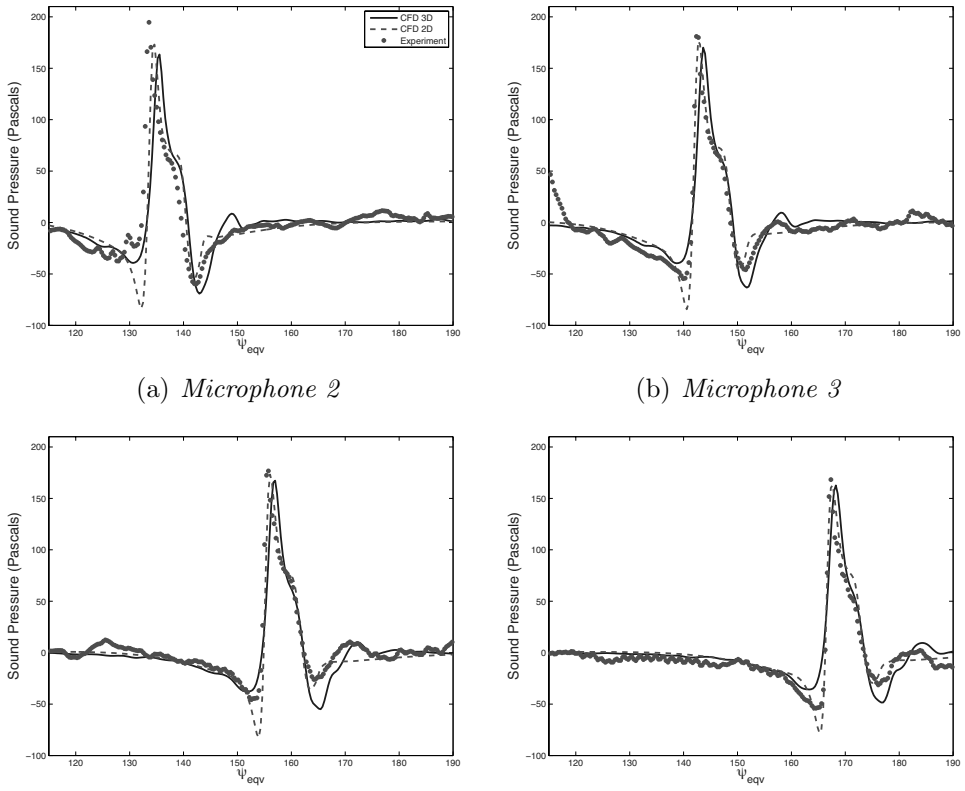

(a) *Microphone 2* (b) *Microphone 3*

(c) *Microphone 4* (d) *Microphone 5*

Figure 3.29: *Far-field noise prediction for strong BVI.*

thickness noise dominates the acoustic pulse and has the characteristic shape of a large negative decrease in pressure. Out of plane of the rotor the thickness noise diminishes to its minimum directly below the interaction, and the loading noise becomes dominant. At the far-field locations, shown in Fig. 3.30(b), the loading noise dominates the acoustics. The loading noise tends to propagate in the direction of blade rotation, and for the angles shown here, it is seen to peak at 45° below the point of interaction. In addition, even for the shallow angle close to the rotor plane, the loading noise is significant and larger than the thickness noise.

The acoustic pulse differs in both magnitude and shape from the near-field to the far-field of the interaction. Close to the blade, both the near-field and the far-field acoustic sources, given in equation 2.28 and equation 2.29, make up the acoustic pulse. Further from the blade, the near-field sources quickly diminish proportional to the

inverse of the radial distance squared, and the far-field is defined when the influence of the near-field sources becomes negligible. The decay of the near-field sources accounts for the change in shape of the acoustic pulses between Fig. 3.30(a) and Fig. 3.30(b). At even greater radial locations, the shape of the acoustic pulse will be approximately the same as the shape seen at the radial location of $1R$, but the magnitude of the acoustic pulses will have decayed by the inverse of the radial distance.

To gain a greater insight into the noise directivity, the sound pressure level (SPL) of the interaction is calculated. SPL is defined as:

$$SPL = 20 \log_{10} \left(\frac{p_{rms}}{p_{ref}} \right) \tag{3.5}$$

Where p_{rms} is the root mean square of the pressure during one rotor revolution and p_{ref} is a reference pressure taken to be $20\mu Pa$. This reference pressure is an approximation to the lower threshold of human hearing. The SPL during a strong interaction is computed in a cubic area surrounding the interaction with vertices of $0.75R$. This cubic area has dimensions of $100 \times 100 \times 100$ points at which the acoustic pressure is calculated. Due to the linear nature of the governing equations, this calculation can be largely parallelised, and the present computations are spread between 100 CPUs using the computational resources described in Appendix B. Each CPU takes approximately 7 days to complete the computation, resulting in 700 days of CPU time to calculate the acoustic data within this cubic area.

An isosurface of $130dB$ of SPL surrounding the interaction is shown in Fig. 3.31 for the total, thickness and loading noise. The SPL is also shown on a plane at a radial location of $0.7R$ and perpendicular to the steady vortex axis. The thickness noise is confined largely close to the plane of rotation, where its maximum level of approximately $150dB$ is reached. Out of the rotor plane, the SPL of the thickness noise quickly diminishes. The interaction has little effect on the thickness noise, as it is dependent on the blade surface normal velocity, which is largely determined by the

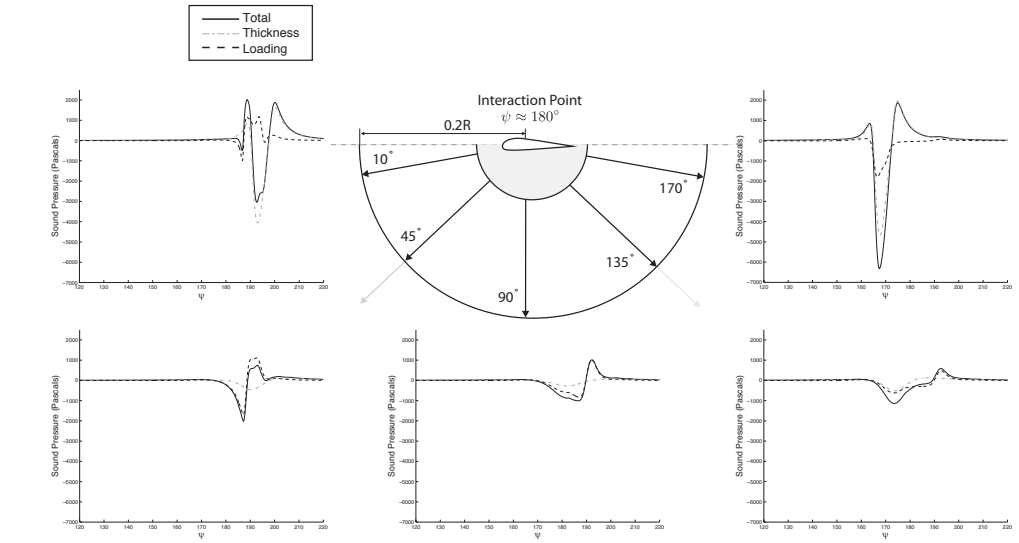

(a) *Acoustic energy at* $0.2R$ *radius from interaction.*

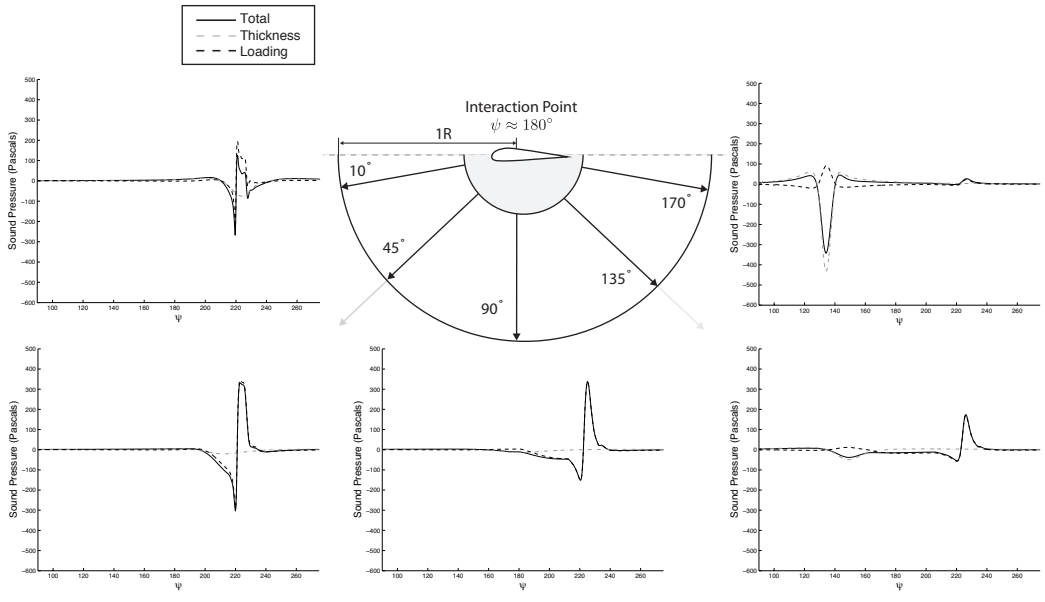

(b) *Acoustic energy at* $1.0R$ *radius from interaction.*

Figure 3.30: *Thickness and loading noise propagation from a strong interaction.*

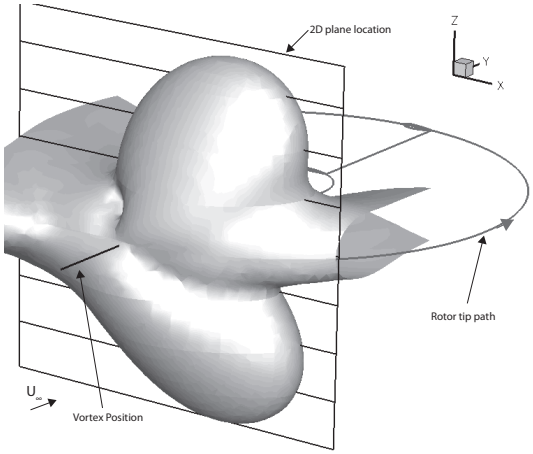

(a) *Total noise.*

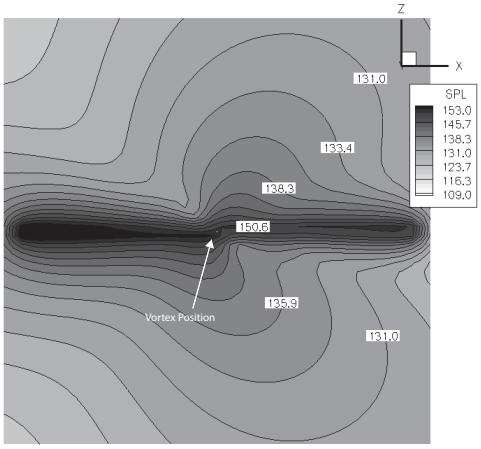

(b) *Total noise.*

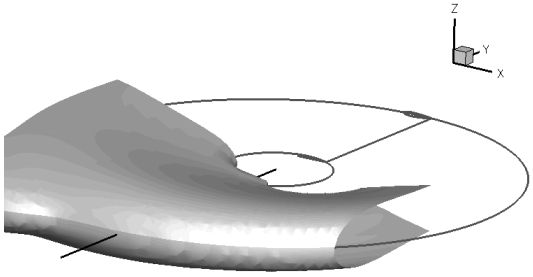

(c) *Thickness noise.*

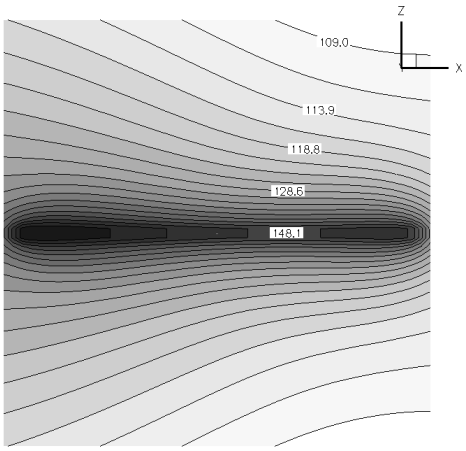

(d) *Thickness noise.*

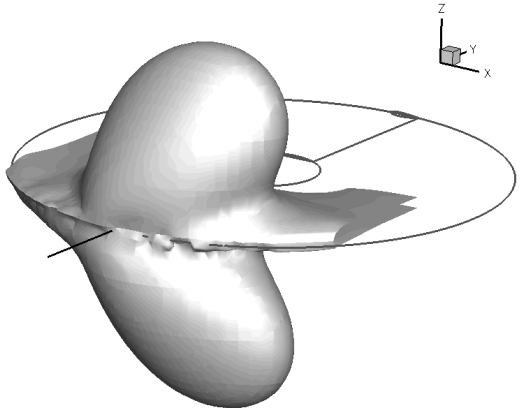

(e) *Loading noise.*

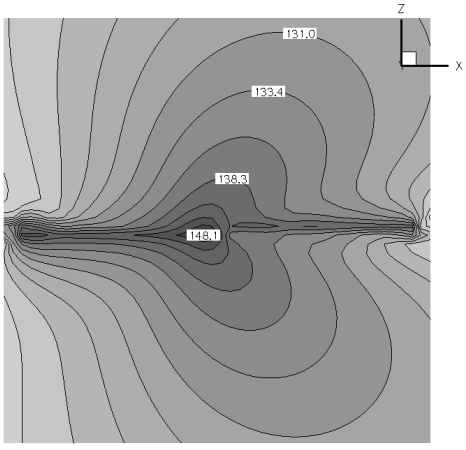

(f) *Loading noise.*

Figure 3.31: *SPL of strong interaction. Isosurface show SPL of* $130dB$.

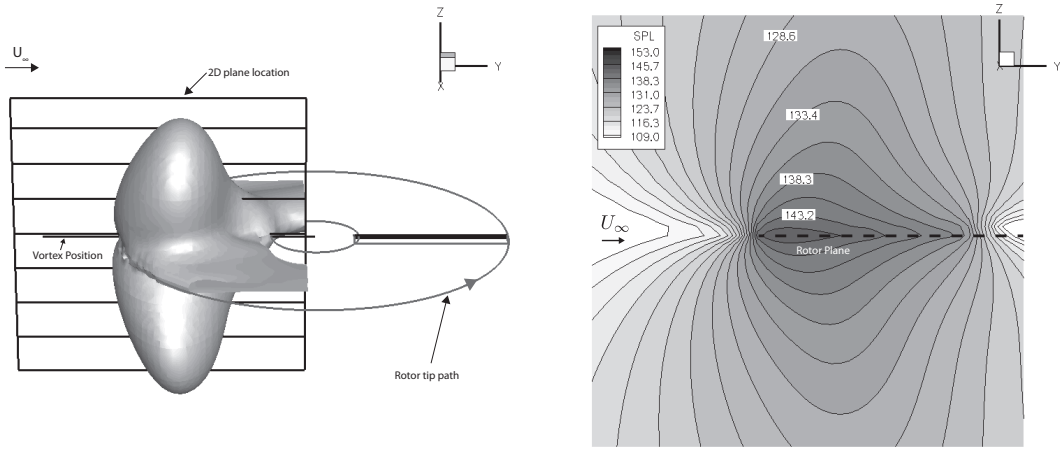

(a) *Loading noise SPL of* $130dB$. (b) *Plane of loading noise at interaction point.*

Figure 3.32: *SPL of loading noise.*

blade motion and freestream velocity. Due to the effect of the streamwise velocity and the blade rotation, the thickness noise varies linearly along the span, and periodically as the blade rotates. It reaches a maximum at $\psi = 45°$, on the advancing side of the rotor, and a minimum at $\psi = 275°$, on the retreating side.

The interaction has the largest effect on the loading noise, where two large lobes of noise emanate above and below the point of interaction. These large lobes radiate out of the rotor plane and in the direction of rotation of the rotor. As the loading noise is radiated from the interaction, it will begin to convect downstream due to the freestream velocity. This convection causes an apparent bending of the loading noise lobes, which is shown in Fig. 3.32. As the rotor considered here is non-lifting, the loading noise at azimuth locations away from the point of interaction is small, and confined to close to the rotor plane.

3.5 Summary and Implications

In this Chapter, an idealised blade-vortex interaction is studied using the present methodology. This idealised interaction is based on the experimental study of Caradonna *et al.* [19], where an independently generated vortex interacts with a ridged non-lifting rotor. This interaction is near parallel, and the salient flow physics are largely two-dimensional.

The interaction is initially studied by considering a two-dimensional aerofoil-vortex interaction, where the vortex is initiated in the flow as a perturbation based on an empirical vortex model. The current methodology is shown to preserve the structure of the vortex well against numerical dissipation, provided a spatial resolution of approximately 8 points across the vortex core is maintained. A weak interaction, where the vortex passes below the aerofoil by $\frac{1}{4}c$ and a strong interaction where the vortex impacts directly onto the aerofoil are studied. It is found that the current inviscid methodology captures all the pertinent flow physics of both these interactions and the computed surface pressures compare very well to experimental data. The detailed wave propagation that occurs across the aerofoil surface, which has been noted in previous experiments, is also captured for both the strong and weak interaction computations. These results are compared to an indicial method, and it is seen that the change in C_l and its gradient can be well predicted over a range of vortex-blade miss distances. However, when the strength of the vortex is strong or the freestream velocity become transonic, the nonlinear effects of the flow become important and the indicial model predicts the interactions inaccurately.

A two-dimensional AVI is an idealisation of a straight vortex interacting with a parallel blade. Ultimately though, accurate prediction of a three-dimensional blade-vortex interaction is sought. Therefore, the present analysis is extended to model the idealised interaction in three dimensions. The tip vortex is generated upstream of the rotor from a static vortex generator wing. The current methodology is found to accurately reproduce the vortex structure and swirl velocity, and preserves these accurately against numerical dissipation. The rotor is modelled using a moving overset mesh,

which has the advantage of maintaining high mesh quality in the important regions of the solution domain. The ability of moving overset meshes to pass flow information is assessed, and it is found that time integration errors, caused by a combination of low time integration accuracy and large timesteps, will severely diffuse the vortex structure. This diffusion can be overcome by increasing the time integration accuracy and reducing the timestep. The present simulations utilises a second order backward difference time integration scheme and a timestep equivalent to $\frac{1}{8}^{\circ}$ of blade rotation to model the interaction and this is found to be sufficient to accurately preserve the vortex structure and resolve the blade surface pressures.

The acoustic energy radiated from the interaction is also studied by using a linear acoustic solver. The linear acoustic solver utilises the Farassat 1A formulation of the Ffowcs-Williams Hawkings equations to compute the acoustic pressure propagated from the computed interaction. The near-field acoustics are computed using this linear acoustic solver and are compared with experimental data in addition to acoustic pressure extracted directly from the CFD solution. It is found that the linear acoustic solver captures the characteristics of the acoustic pulse well, however, the magnitude and pulse shape differs somewhat from the experimental data. This deficiency is attributed to the linear acoustic model neglecting the volume source terms which are known to be important for near-field noise prediction. In contrast, the acoustic pressures extracted directly from the computed CFD solution agree well with the experimental data, as the volumetric noise sources are naturally accounted for. In these results, the magnitude of the pulse is slightly underpredicted, which is attributed to numerical dissipation of the acoustic waves.

The linear acoustic solver is then used to compute the far-field acoustics and these are found to compare well with the experimental data, both in shape and magnitude. As the volume acoustic sources do not in general contribute to the far-field acoustics, which is dominated largely by the loading noise sources, this modelling method is sufficient provided that the blade surface pressures are accurate.

The noise directivity of the interaction is studied by computing the sound pressure level (SPL) for a region surrounding the interaction. It is seen that the thickness noise

of the interaction is largely confined to a small region close to the blade, and in the rotor plane. In contrast, the loading noise generated by the interaction radiates largely out of the rotor plane, above and below the point of interaction. The SPL of the loading noise reveals two large lobes of acoustic energy that emanate above and below the interaction point and in the direction of the rotor blade rotation. These lobes are also seen to convect downstream due the freestream velocity.

The main implication of this work is to show that the all the important flow features needed to accurately predict the blade surface pressures during a BVI are resolved using the current approach. Provided sufficient care is taken to preserve the vortex structure against dissipation as it convects through the solution domain, the interaction and the important vortex dynamics are resolved. Consequently, if the blade surface pressures are accurately resolved, then the far-field acoustics can be accurately predicted using a linear acoustic analysis.

Chapter 4

Propeller Wake-Wing Interaction

This Chapter studies the interaction of a propeller wake with a wing, a flow situation experienced by an aircraft powered by tractor-mounted turboprops. The wake of a propeller contains strong tip vortices trailed from the propeller blades, and large axial and swirl velocities. If the propeller is mounted in a tractor configuration, then this wake system will impact upon the wing, drastically altering its lift and drag distribution. Accurate modelling of this flow requires CFD analysis to fully capture the unsteady aerodynamics.

The idealised wing-propeller interaction studies which were experimentally investigated by Samuelsson [44] are analysed using the current methodology. First, the wake of an isolated four bladed propeller is simulated and its wake structure is compared to experimental data. The unsteady simulation of a propeller wake interacting with a wing is then attempted where the isolated propeller solution is imposed as an unsteady boundary condition. This method simplifies the analysis and reduces the computational costs while maintaining the majority of the important flow phenomena. The wing surface pressures at the point of interaction are then compared to the experimental data.

The interaction induces a considerable deformation in the lift and drag distribution

of the wing. The design of an efficient wing is therefore sought to exploit this interaction where the induced drag is reduced for a given lift. To investigate novel wing designs, the current methodology is coupled with an optimisation algorithm to investigate changes in the wing twist distribution.

4.1 Details of Experiment

The experimental data is taken from a study performed by Samuelsson at the former FFA, the aeronautical research institute of Sweden [45, 46]. The primary aims of this study was to gain a physical insight into the complex aerodynamic interference that occurs when the slipstream of a propeller interacts with a fixed wing, and to provide detailed wake and surface pressure data for the validation of computational methods. The experimental setup consisted of a propeller mounted on a nacelle. The propeller design was typical of a modern medium speed turboprop commuter aircraft and was operated at a high thrust during the experiment.

Mounted downstream of the propeller was a removable, untwisted wing, with a constant NACA $63_{(010)}A012$ section. This wing had an aspect ratio of 2, and was mounted at zero angle of attack. The geometry of the experiment is summarised in Fig. A.1 and the test conditions are summarised in Table 4.1.

During the experiment, velocity data in the wake of the propeller was obtained, with and without the fixed wing mounted downstream. This data consisted of time-averaged axial and swirl velocity measurements at various positions downstream of the propeller plane. Pressure measurements were also obtained on the surface of the wing during the interaction along chordwise stations, which are shown in Fig. A.

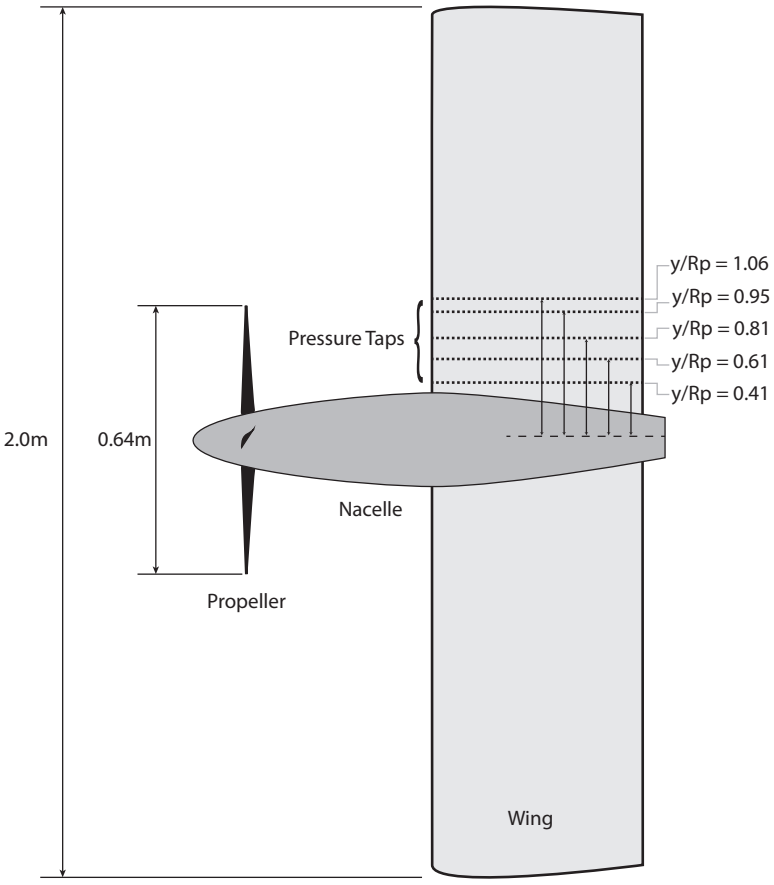

(a) *Top view*

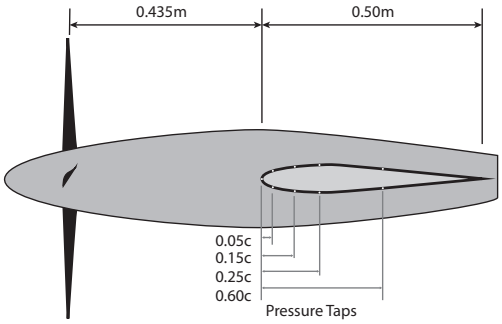

(b) *Side view*

Figure 4.1: *Propeller wake-wing interaction experimental setup for case with the wing. Wake data was also collected for case without the wing.*

Propeller Conditions	
J	0.7
C_T	0.23
$U_\infty(m/s)$	50
M_∞	0.15
Reynolds number (Wing)	$1,700,000$

Table 4.1: *Summary of experimental conditions*

4.2 Isolated Propeller Study

4.2.1 Isolated Propeller Mesh System

The steady wake generated from an isolated propeller mounted on a nacelle is first computed without the presence of the wing. The propeller is composed of a blend of NACA 6 series aerofoils with varying thickness along the span. The twist and chord distribution are given in Fig. 4.2 with details of the aerofoil section at selected spanwise locations. This geometry is representative of a typical turboprop geometry for a medium sized turboprop commuter aircraft. The propeller was discretised using a C-O mesh topology, with collapsing planes at the tip to produce high mesh quality in the tip region. The dimensions of the propeller mesh are $119 \times 181 \times 56$ in the chordwise, spanwise and wall normal direction respectively. The propeller mesh is shown in Fig. 4.3.

The background mesh represents the flow domain from the nacelle to the far-field boundaries. This area is discretised with $175 \times 155 \times 394$ points in the azimuthal, wall normal and streamwise directions, respectively, and then subdivided into 5 smaller meshes. As shown in Fig. A, the nacelle geometry in the experimental setup has a blunt trailing edge, but to ensure high mesh quality for the computations, the trailing edge was smoothed out. As this is downstream of the position where the wake interacts with the wing, this change will have little influence on the computed surface pressures of the wing. The propeller mesh is merged with the wall of the nacelle so the first

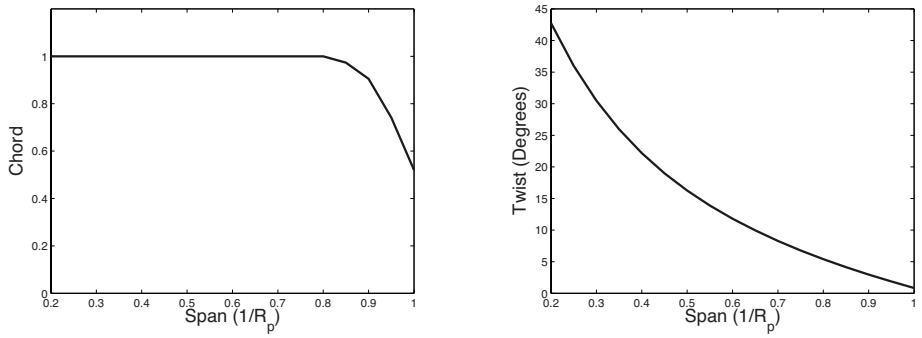

(a) *Chord Distribution.* (b) *Twist Distribution.*

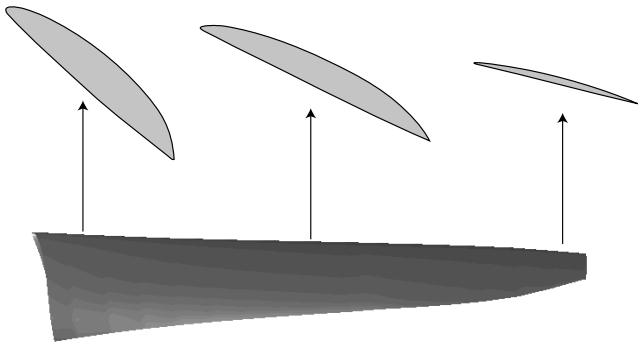

(c) *NACA 6-series aerofoils across span of propeller.*

Figure 4.2: *Propeller sectional properties.*

spanwise plane at the propeller root is coincident with the wall of the nacelle. This is shown in Fig. 4.4. At this first spanwise plane of the propeller and the wall of the nacelle, an inviscid wall boundary condition is imposed. Details of the nacelle and propeller geometry are given in Appendix A.

As the flow of a isolated propeller mounted on a symmetric nacelle has two planes of symmetry, only a quarter of the domain needs to be modelled for a four bladed propeller. Periodic boundary conditions are then used to communicate flow data correctly between the first and last azimuth planes, illustrated in Fig. 4.5.

The region where the tip vortex will convect in the background mesh has been refined to preserve the strong flow gradients associated with the tip vortices. This

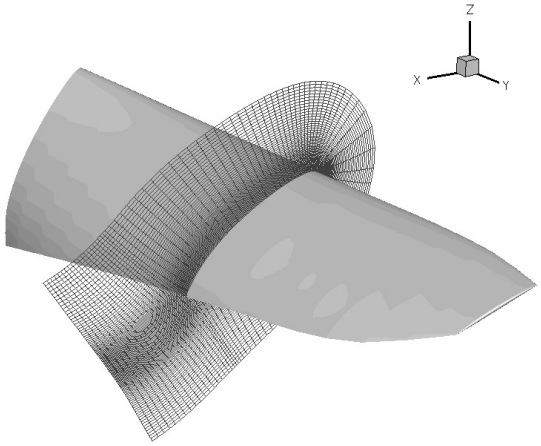

Figure 4.3: *Propeller mesh detail*

refined region is shown in Fig. 4.4. The spacing in this region was refined to 8 points across the vortex core, as this resolution was found to adequately preserve the tip vortex structure as it convects downstream of the propeller. The boundary of the background mesh extended to roughly 10 propeller radii from the nacelle and approximately 20 propeller radii downstream. At these outer regions the mesh spacing is very coarse, approximately equal to the chord of the propeller. This coarse mesh spacing causes any strong flow features to dissipate before reaching the outer boundary and hence at these far boundaries the characteristic freestream boundary conditions can be imposed without spurious reflections.

4.2.2 Isolated Propeller Computational Results

The Euler equations are solved in a rotational frame of reference [50] until a steady thrust coefficient, C_T, is achieved and the norm of the residual had dropped sufficiently. The converged value of the C_T= 0.25 is 10% higher than the experimental value, and this is similar with other inviscid thrust calculations for the same isolated propeller configuration [42]. Convergence is achieved within 6000 iterations and the C_T and residual norm is shown in Fig. 4.6. It is seen that the value of the C_T is within 5% of

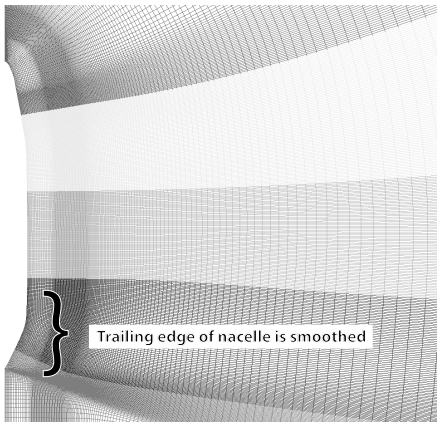

(a) *Nacelle geometry smoothed out at trailing edge.*

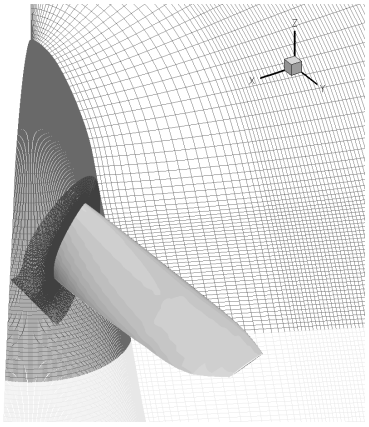

(b) *Propeller mesh overset onto background mesh.*

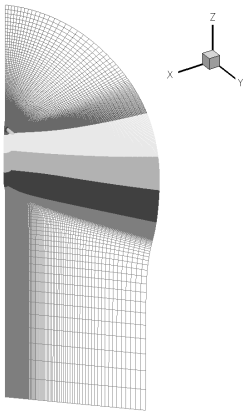

(c) *Full view of mesh system.*

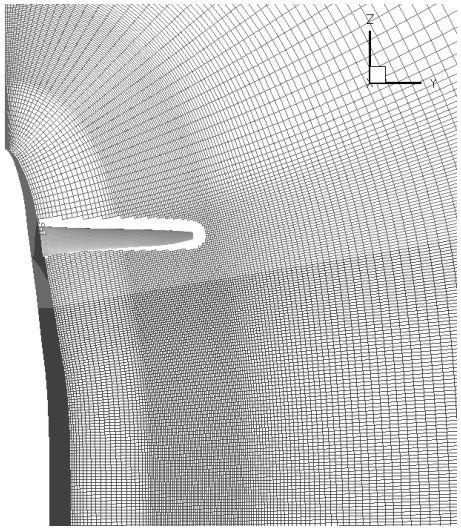

(d) *Fine mesh space in location where vortex convects.*

Figure 4.4: *Mesh system for isolated propeller simulations.*

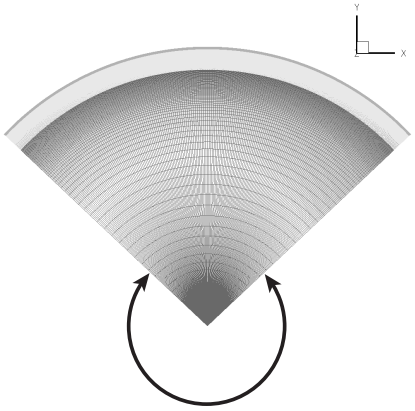

Figure 4.5: *Top view of mesh system showing the planes where the periodic boundary conditions are enforced.*

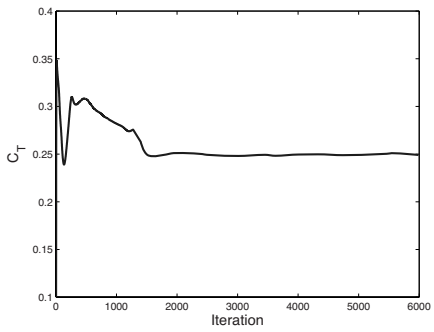

(a) *C_T of propeller as simulation is advanced.*

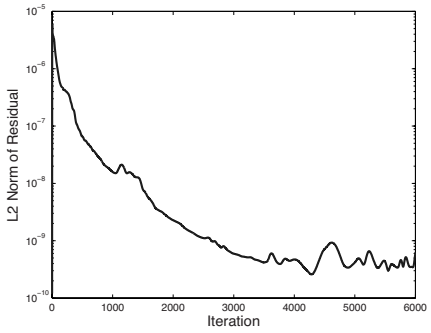

(b) *L-2 norm of residual as simulation is advanced.*

Figure 4.6:

its final value after 1500 iterations, yet the norm of the residual is not fully converged. This is because the wake of the propeller is not fully developed until approximately 5000 iterations have been performed. Each iteration took approximately 11 seconds utilising the computational resources described in Appendix B.

The steady flow field of the wake of the propeller is shown in Fig. 4.7, where isosurfaces of vorticity reveal the position of the vortex and contour colours show the density. The vortices develop into a regular quadruple helix structure, the diameter of which contracts slightly as the vortices convect downstream. The flow solver maintains

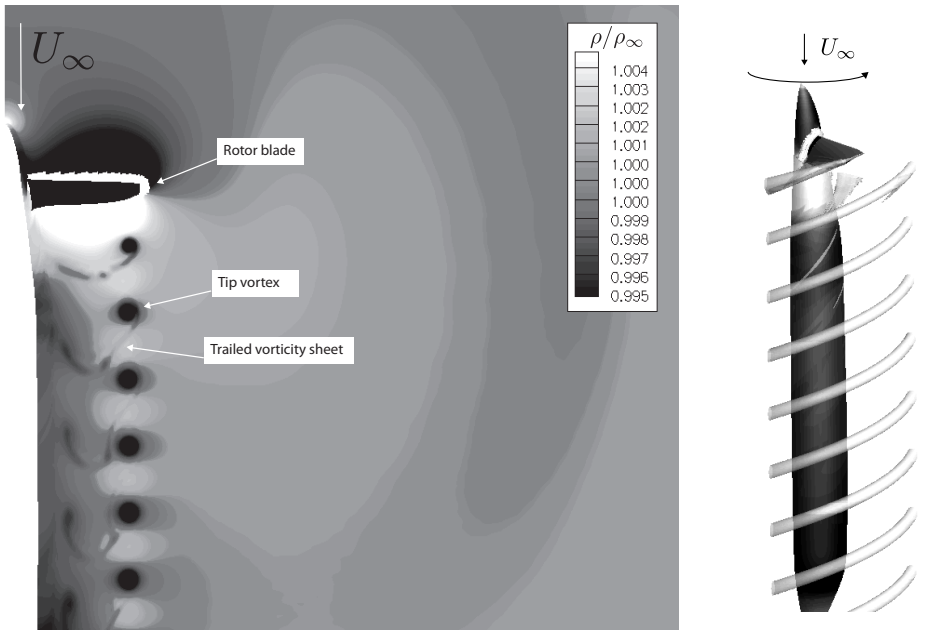

(a) *Density of propeller wake.*

(b) *Isosurface of vorticity reveals the trailed tip vortices.*

Figure 4.7: *Isolated propeller computation results.*

the structure of the vortices well downstream of the propeller until they convect into the coarse mesh region where they dissipate.

The computed axial velocity is compared directly with the experimental results in Fig. 4.8 for various positions behind the propeller plane. The propeller induces large axial velocities in its wake, up to 170% of the free stream velocity, and this is in general well resolved by the CFD solver. Close to the propeller plane, the discrepancy between the computed and experimental results is greatest, which is indicative that the early development of the wake is not being full captured by the present method. This could be a result of viscous effects in the wake having a significant influence on its early development, which are not accounted for by the inviscid analysis used here. Numerical studies of tip vortex formation [50] have shown that viscous effects can influence the wake formation in the near-field, where secondary and tertiary vortex structures are formed close to the blade surface. However, as the wake further develops downstream, the agreement with the experiment is excellent. The furthest downstream location in

Fig. 4.8 also shows a slight discrepancy from the experimental data. This difference is likely due to the mesh geometry at the trailing edge of the nacelle differing from the experimental geometry. As mentioned before, this difference in geometry was to ensure high mesh quality in the important regions of the solution domain.

The swirl angle is also compared with the experimental data and is shown in Fig. 4.9. The swirl angle is defined as the angle between the swirl velocity vector and the freestream velocity vector, and is positive in the rotational direction of the propeller. This propeller induces large swirl angles close to its root, which gradually decreases outwards. As the wake develops, the swirl angle matches closely with the experimental data. Again, as seen in the axial velocity results, the swirl angle closest to the propeller plane has the greatest discrepancy from the experimental data.

The computed velocities of the propeller wake agree well with the experimental data, however, these are time-averaged values and mask the unsteady nature of the flow in the propeller wake. To reveal the true unsteady nature of the flow, the axial, swirl and radial velocities are shown on a plane parallel to the rotor plane and at $1.72R_p$ behind it in Fig. 4.10. The axial velocity is defined as positive downstream, the swirl velocity is positive is the direction of propeller rotation, and the radial velocity is positive outward from the rotational axis. The velocities within the propeller wake vary significantly with radial and azimuthal location. The tip vortex is labelled at the outer edge of the wake, and induces a large local variation in axial velocity, between 0.6–2.0 w/U_∞. As this tip vortex is inclined to the plane, large variation in the swirl and radial velocities are also present.

Inboard of the tip vortex, there are also variations in the flow velocity across the propeller wake. Close to the nacelle surface, an inboard vortex is present. The development of this vortex can be seen in Fig. 4.7, and is produced by the inboard section of the trailed vorticity sheet rolling up to form a root vortex. This vortex is not as strong as the tip vortex, yet still induces a significant variation in velocity close to the nacelle surface. It should also be noted that the inboard mesh resolution is lower that the tip vortex region, and therefore the root vortex is not as well resolved. Studies where this mesh region is refined revealed that a stronger root vortex system develops

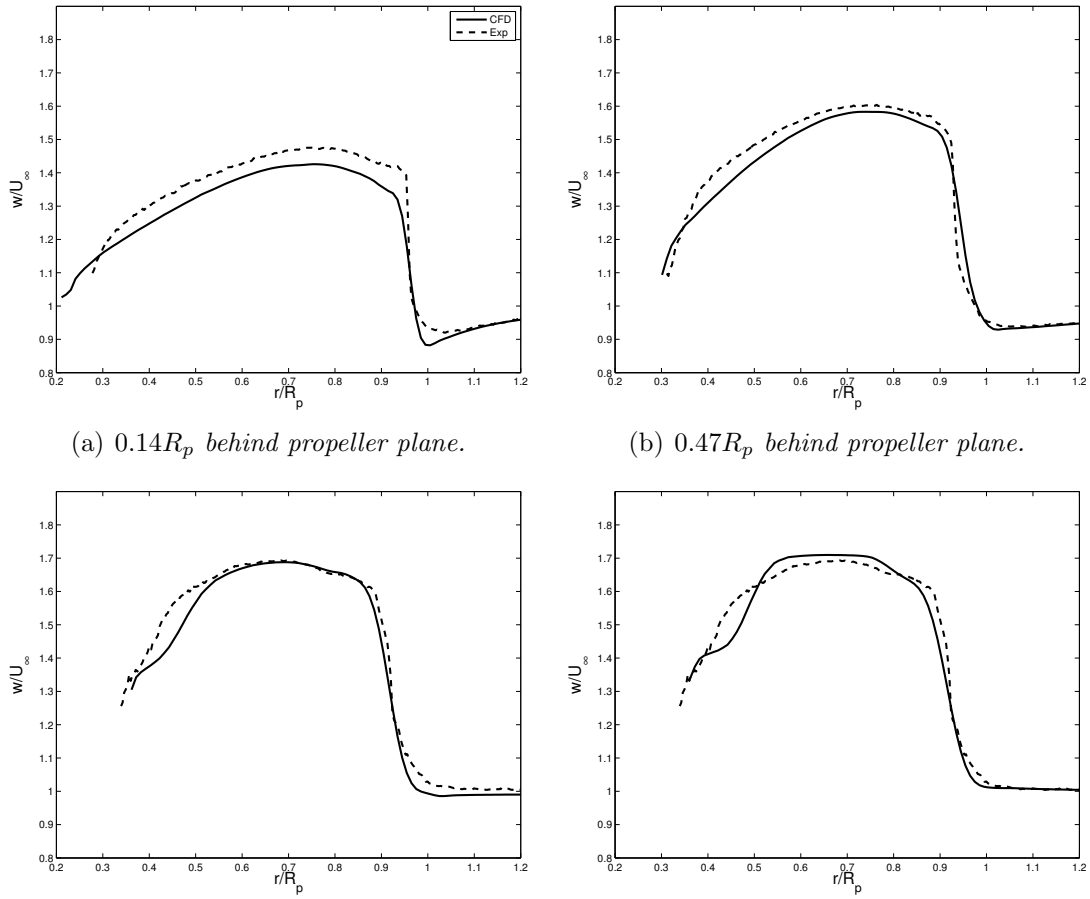

(a) $0.14R_p$ *behind propeller plane.*

(b) $0.47R_p$ *behind propeller plane.*

(c) $1.72R_p$ *behind propeller plane.*

(d) $3.0R_p$ *behind propeller plane.*

Figure 4.8: *Axial velocity at various locations downstream of propeller.*

in the flow close to the nacelle surface, but that this is still weaker than the tip vortex.

In addition to the high swirl velocity, the tip vortices will have a velocity component along the vortex axis. This vortex axial velocity is largely contained within the core region of the vortex and can either be in the direction of propeller rotation (velocity deficit) or in the opposite direction (velocity excess). Theoretical expressions for the axial velocity have been derived for the axial velocity by Batchelor [85] and later supplemented by Spalart [86], where the axial velocity of the vortex was found to be proportional to a *circulation parameter*, $\frac{\Gamma}{U_\infty b}$, where Γ is the vortex circulation and b is the wingspan. This expression was found to agree qualitatively with experimental

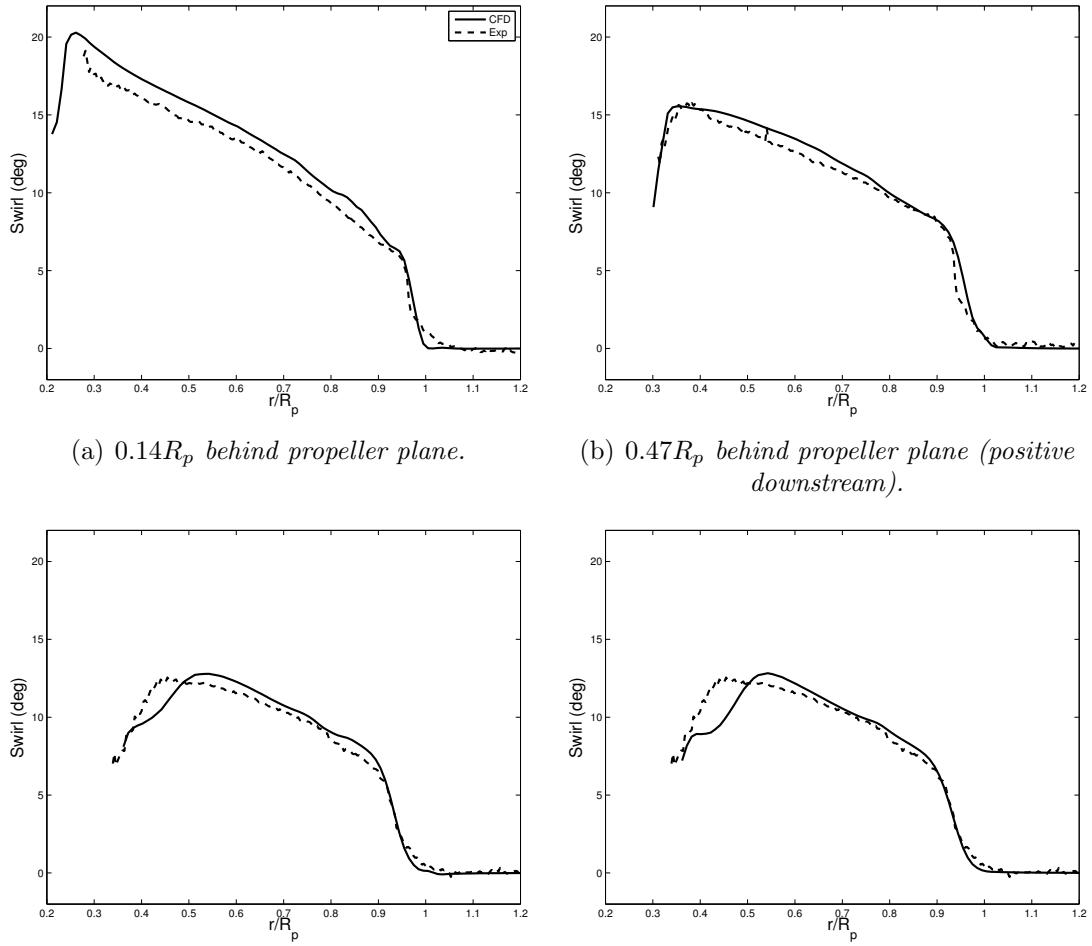

(a) $0.14R_p$ *behind propeller plane.*

(b) $0.47R_p$ *behind propeller plane (positive downstream).*

(c) $1.72R_p$ *behind propeller plane.*

(d) $3.0R_p$ *behind propeller plane.*

Figure 4.9: *Swirl velocity at various locations downstream of propeller.*

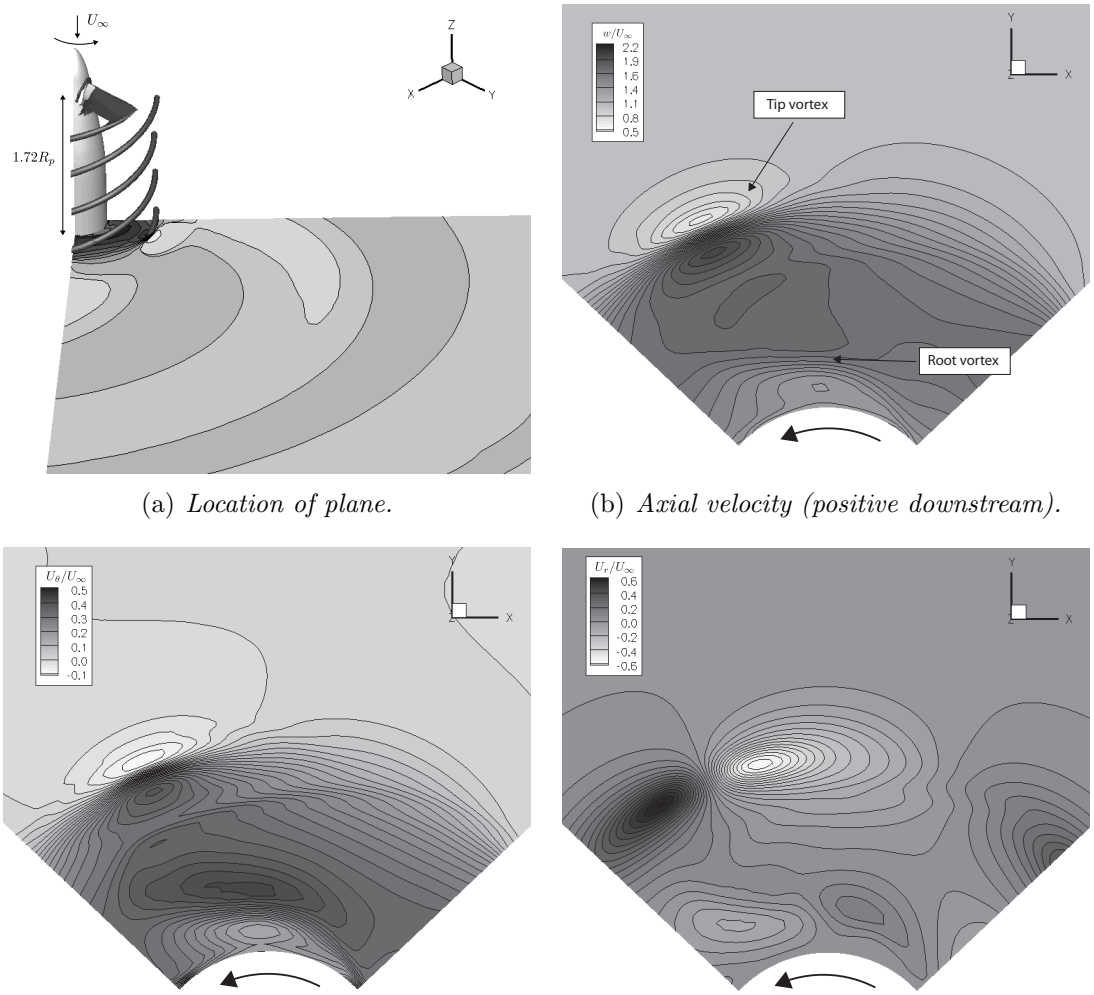

(a) *Location of plane.*

(b) *Axial velocity (positive downstream).*

(c) *Swirl velocity (positive anticlockwise).*

(d) *Radial velocity (positive outward from propeller axis).*

Figure 4.10: *Axial, swirl and radial velocity at* $1.72R_p$ *behind the propeller plane.*

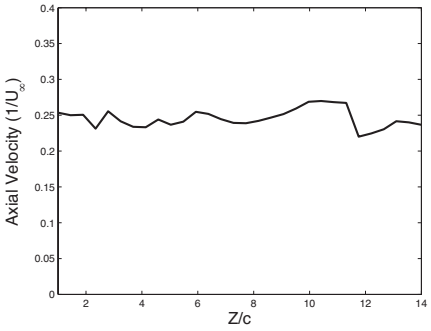

Figure 4.11: *Vortex axial velocity.*

data [87], where a highly loaded wing produced a large circulation parameter and an axial velocity excess in the vortex core.

Previous CFD studies [50] have shown favourable comparisons with experimental data when recreating the vortex axial velocity, however resolving this velocity accurately over many chord lengths of convections required a high mesh resolution, typically in the order of 20 points across the vortex core or greater and a similar resolution in the axial direction of the vortex. This high resolution is prohibitively expensive in the current simulations, so the axial velocity is unlikely to be accurately resolved. For the current simulations, the axial velocity of the vortex at various locations behind the propeller plane is shown in figure 4.11 defined as positive in the direction of propeller rotation. A near-constant velocity deficit is maintained throughout the vortex convection. As this velocity is restricted to the small region of the vortex core, it can be expected to have a comparatively small effect when interacting with the downstream mounted wing compared to the influence of the axial and swirl velocity in the propeller wake.

4.2.3 Grid Convergence

To confirm grid convergence, the isolated propeller computation is performed on three mesh systems where the resolution of the mesh is changed in all directions. These three

Resolution	Spatial resolution across the vortex core
High	12
Medium	8
Low	4

Table 4.2: *Summary mesh resolutions for isolated propeller simulation.*

cases are summarised in Table 4.2 where the mesh points across the vortex core are used as a convenient measure of mesh resolution.

The axial velocities and swirl angles computed on the high, medium and low resolution meshes are shown in Fig. 4.12 for a single plane at a location of $1.72R_p$ downstream of the rotor. All three meshes perform well at preserving the general shape and magnitude of the propeller wake, however, the preservation of the tip vortex structure differs between the three meshes. This is seen in Fig. 4.12(b) and 4.13(d), where the edge region of the wake is shown in detail. The tip vortex is present at this edge region and for the lower resolution meshes, this vortex is seen to have diffused. However, the medium and high resolution mesh show the velocity converging on a velocity profile.

The computed time-averaged velocity masks the extent of the numerical diffusion of the vortex structures on the lower resolutions meshes, and is more clearly seen by examining the velocity across the isolated tip vortex. Fig. 4.13 shows the vortex profile in the three resolution meshes at a location of $1.72R_p$ behind the rotor. Again, the low resolution mesh in very diffusive as the magnitude of the vortex velocity profile is overpredicted and the core diameter has increased. The computed velocity profile on the medium and higher resolution meshes appears to have converged on a solution, where both the magnitude of the velocity and the core size is similar for both cases.

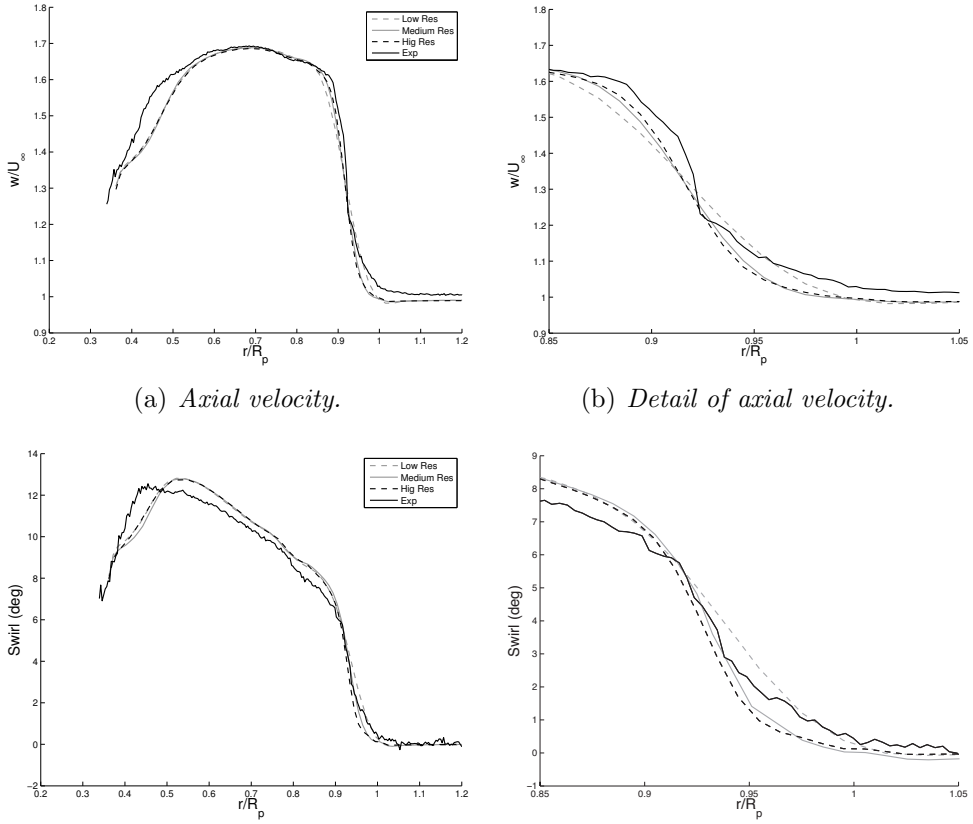

(a) *Axial velocity.* (b) *Detail of axial velocity.*

(c) *Swirl angle.* (d) *Detail of swirl angle.*

Figure 4.12: *Axial velocity and swirl angle on meshes of three different resolutions at a location of* $1.72R_p$ *behind propeller plane.*

4.3 Propeller Wake-Wing Interaction Study

It has been shown in the previous section that the wake of the propeller can be accurately captured using the current methodology, and in the present section the interaction of the wake of the propeller with a fixed wing is studied. To simulate this interaction fully would require the representation of all 4 of the propeller blades, the nacelle, and the 2 fixed wings in the computation. This approach is prohibitively expensive on the available computational resources especially due to the motion of the propeller with respect to the wing, therefore a simpler and computationally more efficient approach is taken where the propeller wake is imposed as an unsteady boundary

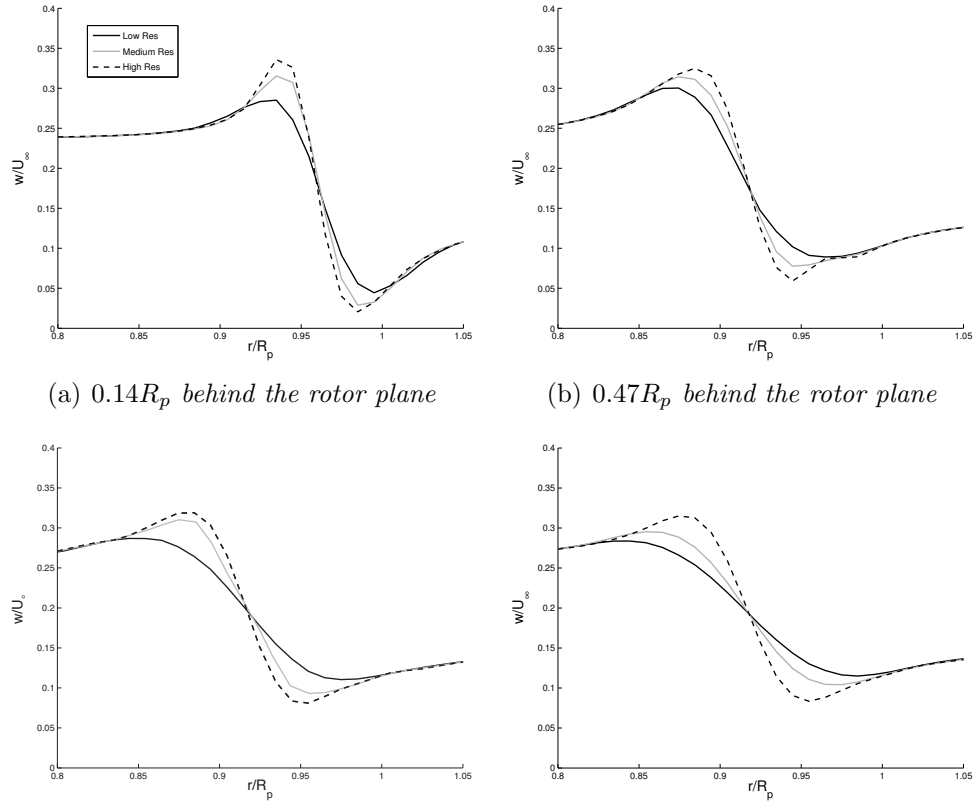

(a) $0.14R_p$ *behind the rotor plane* (b) $0.47R_p$ *behind the rotor plane*

(c) $1.72R_p$ *behind the rotor plane* (d) $3.0R_p$ *behind the rotor plane*

Figure 4.13: *Tip vortex velocity various distances downstream of rotor plane on three resolution meshes.*

condition.

4.3.1 Propeller Wake-Wing Mesh System

The mesh system for the modelling of the propeller wake-wing interaction is similar to the modelling of the isolated propeller, and is shown in Fig. 4.14. The upstream part of the mesh where the propeller was modelled for the isolated propeller computation is removed and here an unsteady boundary condition which introduces the propeller wake into the flow is imposed, as explained in section 4.3.2. When the propeller wake is introduced in this manner, one plane of symmetry exists for this case and only half

the nacelle needs to be modelled with appropriate periodic boundary conditions.

The wing mesh is of C-O topology with dimensions $291 \times 127 \times 71$ in the chordwise, spanwise and wall normal directions, respectively. The spanwise spacing is clustered in the region where the vortex convects into the wing mesh, similar to the background mesh and is shown in Fig. 4.14(c). The wing is mounted onto the nacelle where the root of the wing mesh is merged with the nacelle wall boundary. Around the wing, a hole is cut in the background nacelle mesh, and the governing equations are not solved at the points within this hole.

4.3.2 Unsteady Boundary Condition

To model the propeller wake-wing interaction fully is prohibitively expensive on the current computational resources, as this would require the four propeller blades, the nacelle and the entire wings to be resolved. Therefore, an efficient means of introducing the wake into the flow as an unsteady boundary condition is used.

A plane of the flow solution from the isolated propeller simulation is extracted immediately downstream of the propeller plane. This solution is then imposed as an unsteady boundary condition on the propeller wake-wing interaction simulations, as indicated in Fig. 4.14(a). At every timestep the mesh boundary points are updated by searching within the extracted flow solution and interpolating the flow variables. As the wake solution rotates with respect to the stationary wing, new interpolation points must be found for every timestep, and this is performed using the stencil walk procedure outlined in Chapter 2.

This method has the drawback that the influence of the wing on the development of the propeller wake is not fully captured. The importance of this has been noted in previous studies of propeller wake-wing interactions [48] and is dependent on many factors, particularly the propeller-wing separation distance. In the present study, however, the propeller-wing separation distance is quite large at $1.6R_p$.

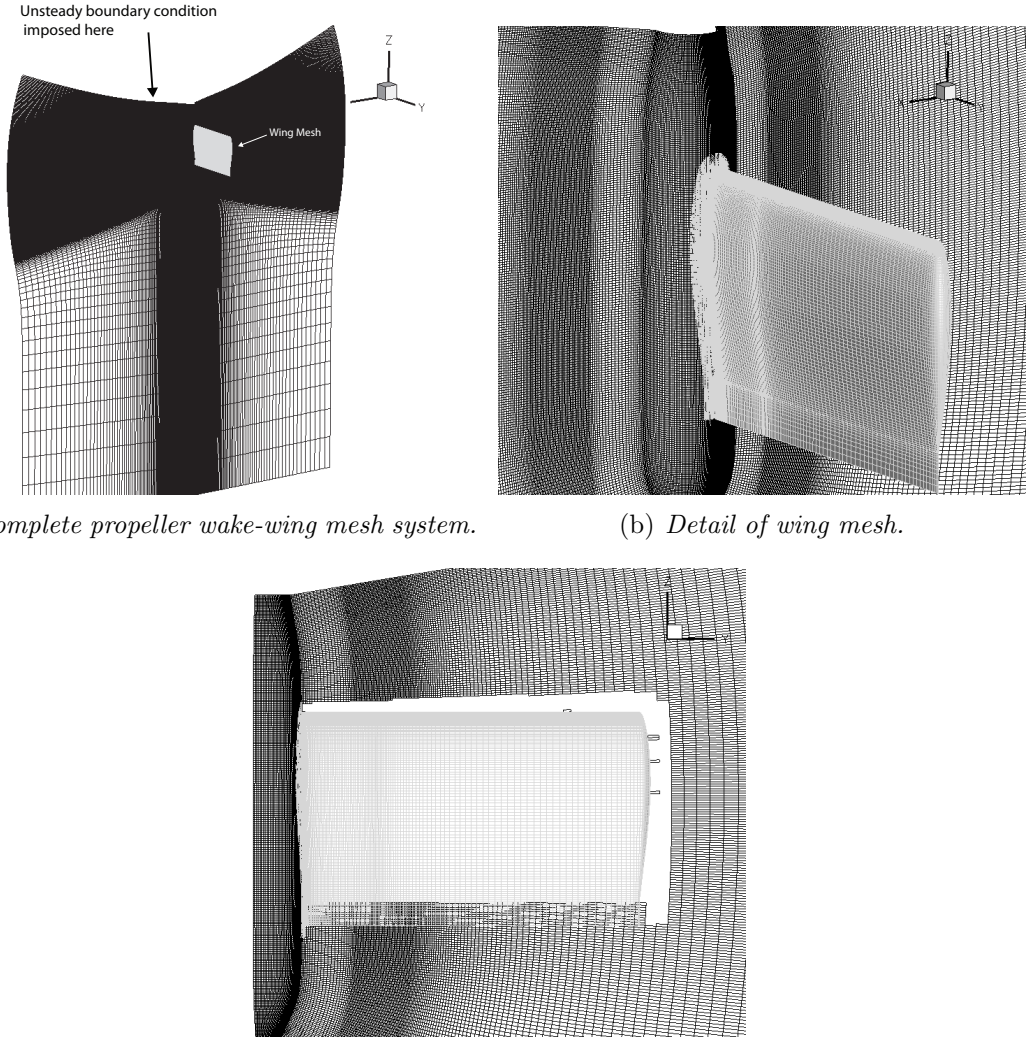

(a) *Complete propeller wake-wing mesh system.* (b) *Detail of wing mesh.*

(c) *Detail of hole cut around wing mesh.*

Figure 4.14: *Propeller wake-wing mesh system.*

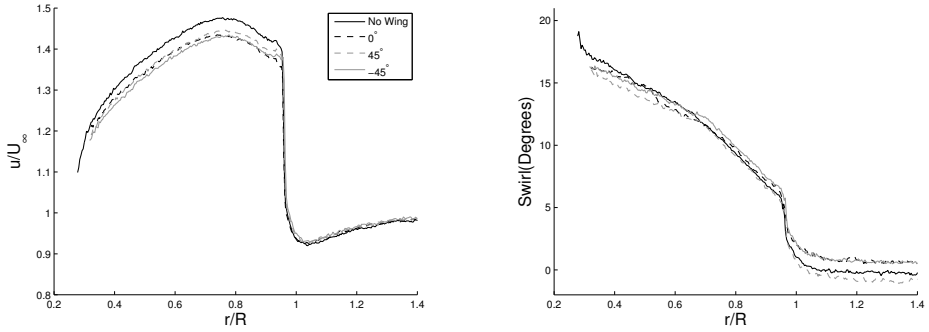

(a) *Axial velocity.* (b) *Swirl angle.*

Figure 4.15: *A comparison of the experimental data of the wake for a case with and without the wing.*

The extent of the influence that the wing has on the propeller and its wake can be seen in the experimental data. The experimental study obtained wake data for a case where the wing was mounted on the nacelle, in addition to the isolated propeller measurements. Fig. 4.15 shows a comparison of the experimental wake data at a position of $0.14R_p$ downstream of the propeller plane. The velocity data in the wake is shown at various angles around the nacelle for the case where the wing was present and these angles are relative to the wing position, with the wing located at 0°. Also shown are the wake measurements for the isolated propeller without the wing. It can be seen that although the wake measurements of the propeller with the wing differ from the isolated propeller case, the difference is small at this plane location. However, the two cases begin to diverge downstream where the wing has a larger influence on the propeller wake structure. The unsteady boundary condition is therefore imposed as far upstream as possible at a location of approximately $0.25R_p$, closely behind the propeller plane. This allows the wake to develop largely under the influence of the wing.

The isolated propeller wake computation is performed by solving the governing equations in a rotating frame of reference. The computed propeller wake is therefore static with respect to the computational meshes and the flow field is steady in time. However, for the propeller wake-wing interaction simulations the flow field is unsteady in time as the propeller wake, and the tip vortices within it, must convect through

the computational domain. For this unsteady computation, the time integration of the governing equations must be carefully considered to ensure accurate convection of the propeller wake.

To assess the ability of the current methodology to preserve the propeller wake as it convects through the solution domain, the flow field is computed for a case where the unsteady boundary condition is imposed on the mesh system shown in Fig. 4.14, but with no wing present. The results where a first order backward Euler time integration scheme is utilised are shown in Fig. 4.16 where the simulation is performed for a variety of timesteps equivalent to 1°, 0.5° and 0.25° of propeller rotation. Also shown are the results from the steady wake computation, which would be recovered if the errors produced by the numerical time integration were sufficiently reduced. The time-averaged axial velocity and the velocity across the vortex are shown at a location of $1.72R_p$ behind the propeller plane, so the propeller wake must convect approximately $1.47R_p$ to this position. These results show that the tip vortex suffers large diffusion using this time integration scheme. This diffusion is reduced for finer timesteps, yet even for $dt = 0.25°$ the vortex velocity is still overpredicted by a significant amount.

The results where the second order backward difference time integration is used are shown in Fig. 4.17. Here, the larger timestep of $dt = 1°$ produces an incorrect velocity profile. However, for the small timesteps of $dt = 0.5°$ and $dt = 0.25°$, the velocity profile of the steady computation is recovered, and the propeller wake convects accurately through the solution domain.

4.3.3 Propeller Wake-Wing Interaction Results

The simulation is performed with a timestep equivalent to $\frac{1}{2}^\circ$ of the propeller rotation utilising the second order backward differencing time integration scheme to ensure adequate preservation of the wake structure. Within each timestep, 5 sub-iterations with a pseudo timestep of 20 are performed and the norm of the residual is seen to reduce by over an order of magnitude. The residual drop is shown in Fig. 4.18. The

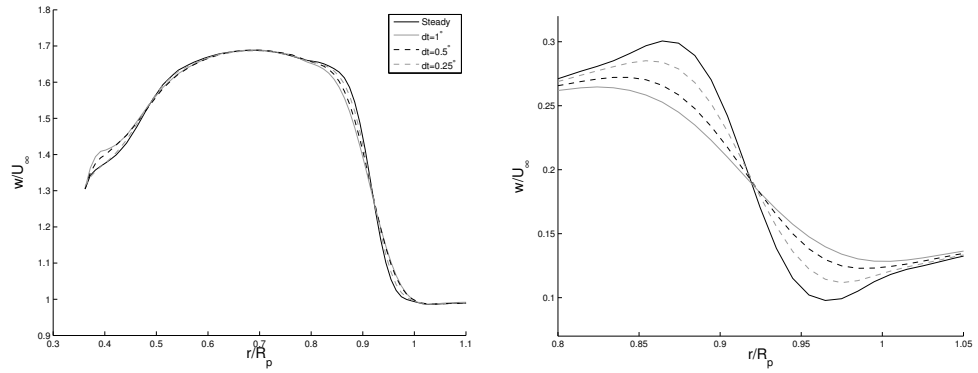

(a) *Axial velocity* (b) *Vortex velocity.*

Figure 4.16: *Propeller wake computed using first order backward Euler time integration.*

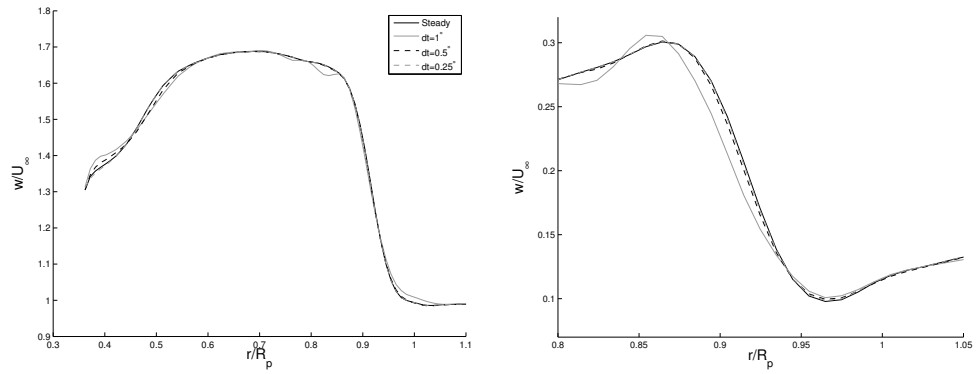

(a) *Axial velocity* (b) *Vortex velocity.*

Figure 4.17: *Propeller wake computed using second order backward difference time integration.*

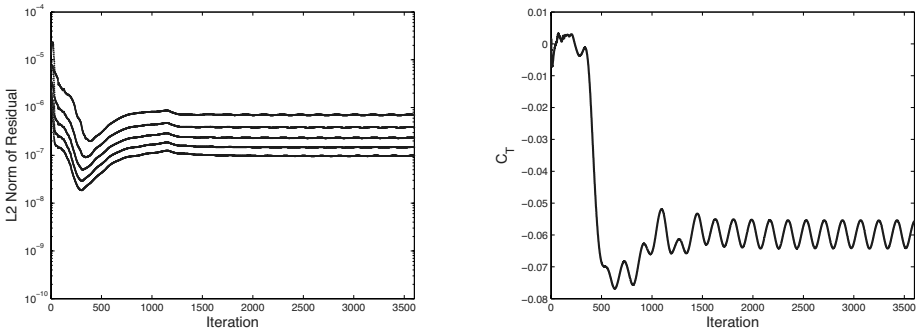

(a) *Residual in wing mesh.* (b) C_L *of wing as solution advances.*

Figure 4.18: *The convergence of the solution.*

C_L of the wing converges on an oscillation with a frequency of 4 peaks per propeller revolution. This is to be expected from the interaction with the wake of a 4 bladed propeller. Each full iteration took approximately 70 seconds using the computational resources described in Appendix B.

The computed surface pressures of the wing at various spanwise locations are compared with the time-averaged experimental data in Fig. 4.19. The spanwise location of the experimental pressure taps are shown in Fig. A. In general the computed wing surface pressures are in good agreement with the experimental data. It is noted that the greatest discrepancy occurs at the span location closest to the root of the wing, which most likely occurs for two reasons. Firstly, the nacelle geometry had to be modified in order to ensure high mesh quality at the trailing edge of the wing, and as a result the nacelle length was extended in the simulations. This altering of the geometry will likely affect the wing surface pressures closest to the nacelle surface. Secondly, where the root of the wing meets the wall of the nacelle, two boundary layers meet. This interaction is extremely complex, and is not captured in the computations performed here due to the inviscid modelling of the fluid. To accurately model this interaction requires an accurate representation of the boundary layer.

In addition to the time-averaged surface pressures, the maximum variation of surface pressure is also shown. This reveals the unsteadiness at the different spanwise locations during the interaction. There is little variation of the surface pressure close

to the root of the wing. The largest variation is seen around the edge of the propeller wake, where the tip vortices impact on the blade.

Grid convergence is also confirmed in Fig. 4.20 where the surface pressures are computed on a low and medium resolution mesh. The resolution of the low and medium meshes is given as the spatial resolution across the vortex core and is summarised in Table 4.2. The results have been split into upper and lower surface of the wing for clarity. It is observed that the mean pressures have converged, yet the magnitude of the limit of the computed surface pressures is slightly smaller for the low resolution case. This is due to the dissipation of the tip vortices in the lower resolution mesh, which produces a weaker interaction with the wing.

A more insightful view of the interaction can be gained by examining the sectional lift and drag of the wing during the interaction. This is shown in Fig. 4.21 where the sectional C_l and C_d are shown along the span of the wing, with time normalised by the propeller rotational angle and each full rotation of the propeller corresponds to 4 tip vortices passing over the wing. Also plotted is the total C_L and C_D of the wing over the same time period. The majority of the lift and drag is seen close to the root of the wing. This is to be expected, as the largest swirl angles occur close to the propeller root, as shown in Fig. 4.9. These large swirl angles are due to the large geometric angle of attack of the propeller blade close to the root. The sectional lift and drag decreases outward along the span, and beyond $r/R_p = 1$, which is approximately the boundary of the wake, they are close to zero.

The inboard drag computed here is largely negative, that is a local thrust force is produced on the wing. This is because of the large swirl angles of the propeller wake rotating the force vector forward as discussed previously. Close to the region where the vortices impact upon the blade, large fluctuations can be seen in this drag corresponding to the tip vortices passing over the wing.

Close to $r/R_p = 1$ where the tip vortices interact with the surface of the blade, the largest oscillation of the forces is seen, and in particular a large oscillation in the sectional drag. A visualisation of the vortex impacting upon the blade is shown in

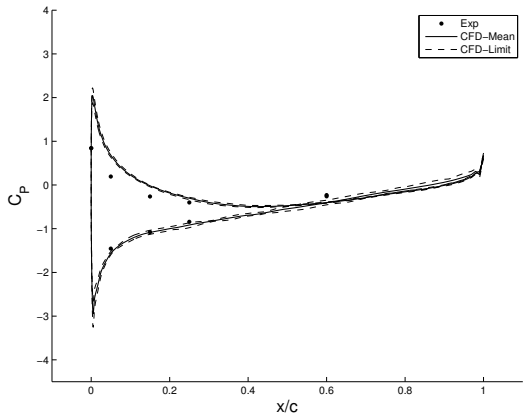

(a) C_P *at* $\frac{r}{R_p} = 0.41$

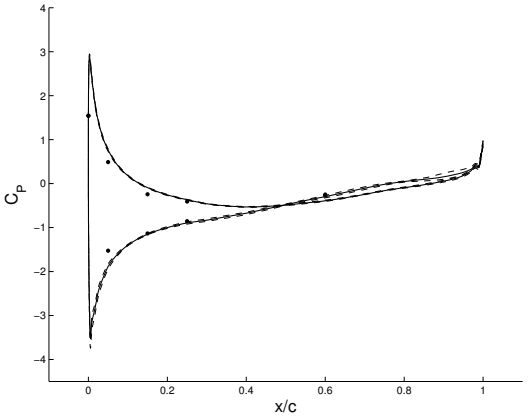

(b) C_P *at* $\frac{r}{R_p} = 0.61$

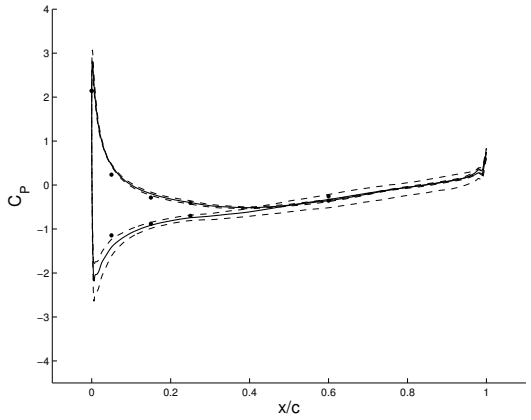

(c) C_P *at* $\frac{r}{R_p} = 0.80$

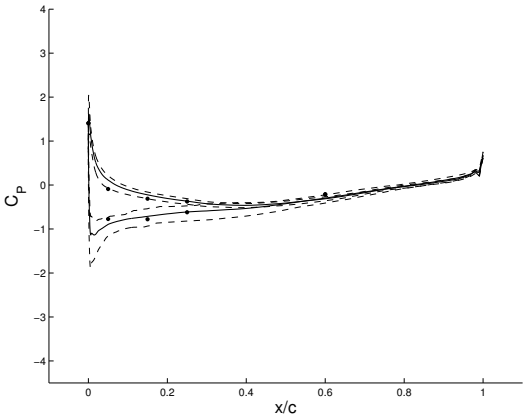

(d) C_P *at* $\frac{r}{R_p} = 0.93$

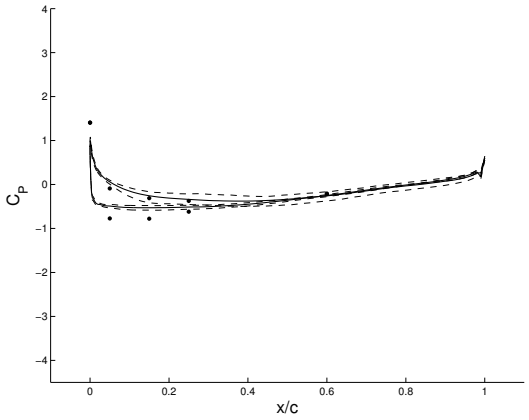

(e) C_P *at* $\frac{r}{R_p} = 1.05$

Figure 4.19: *Experimental and computational time-averaged wing surface pressures during interaction with propeller wake.* R_p *= propeller radius.*

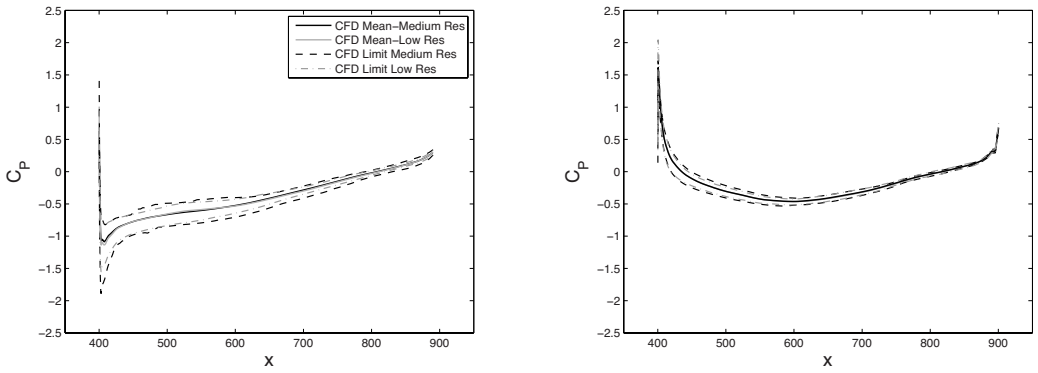

(a) *Lower surface pressures.* (b) *Upper surface pressures.*

Figure 4.20: *Wing Surface* C_P *at* $\frac{r}{R_p} = 0.93$ *on the medium and low resolution meshes.*

Fig. 4.22, where an isosurface of constant vorticity is shown. Also shown is a plane of vorticity at a span location of $r/R_p = 0.97$ revealing the interaction of the vortex with the wing. The interaction is shown for a period of 90° of propeller rotation with 9 time instances and the timescale used is the same as shown in Fig. 4.21. As the vortex approaches the wing it is seen to compress against the wing surface, concentrating its vorticity in the vortex core. The vortex then bends around the leading edge of the wing resulting in the vortex core becoming substantially reduced close to the wing, and the vortex axis lying near parallel the the wing surface. The largest variation in the lift and drag forces shown in Fig. 4.21 occur at a propeller angle of approximately 45° which corresponds with Fig. 4.22(d), where the vortex impacts on the leading edge of the wing.

To examine the effect of the propeller wake on the wing surface pressure, the spanwise perturbation pressure coefficient at a constant chordwise position of $0.05c$ behind the leading edge is shown in Fig. 4.23. The C_P is shown for both sides of the wing which are labelled the "upper" and "lower" side in Fig. 4.22(a). It is evident that the passage of the wake over the wing induces large variations in surface pressures, especially near the region $r/R_p = 1$. This is to be expected due to the tip vortex passing over the wing at this span location. However, the variation of surface pressures on the upper surface of the wing is larger and occurs over a wider area than the lower

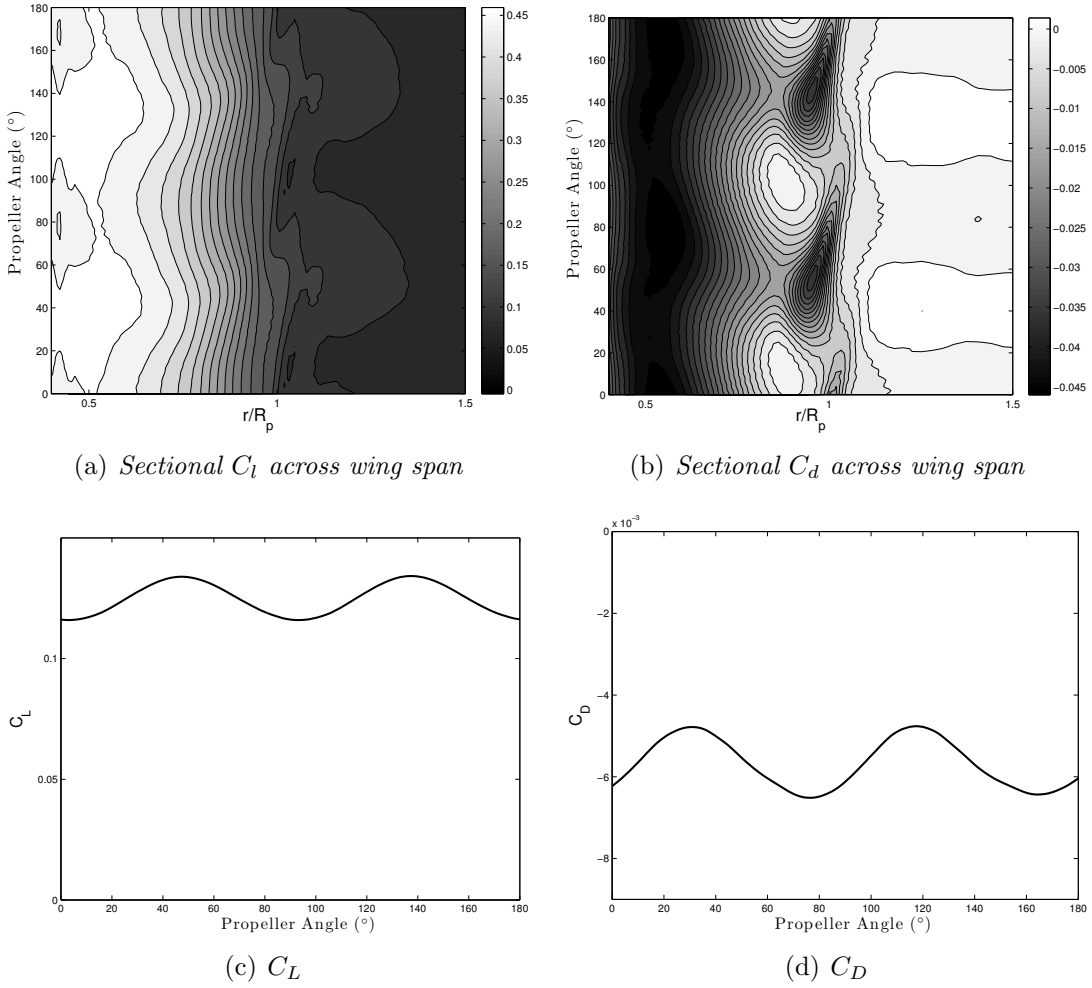

(a) *Sectional C_l across wing span*

(b) *Sectional C_d across wing span*

(c) C_L

(d) C_D

Figure 4.21: *Computed lift and drag on the wing during interaction.*

surface. This is an unexpected result, as one would expect the lower side of the wing to experience the largest pressure variation, as it encounters the wake fully, whereas the upper side is somewhat shielded from the wake by the lower side. However, by examining the computed flow field in Fig. 4.22, it is evident that this shielding of the upper side causes the vortex to bend around the leading edge of the wing, as seen in 4.22(e). This bending aligns the axis of the vortex with the wing, causing the swirl velocity of the vortex to interact more directly with the flow on the surface of the wing, producing an increase in the surface pressure. This larger variation in surface pressure on the upper side of the wing has also been seen in the experimental results of Johnston and Sullivan [88].

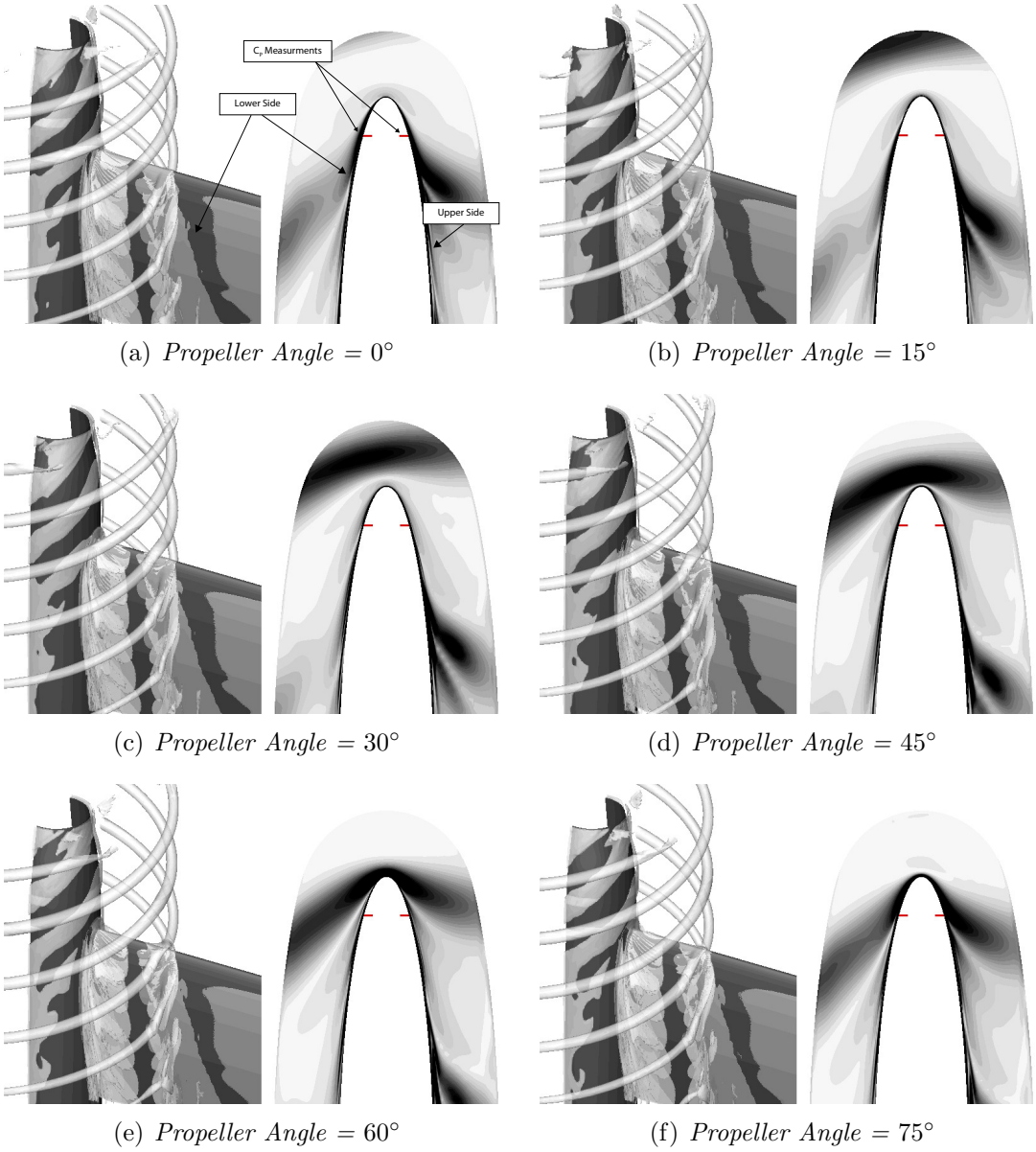

(a) *Propeller Angle* = 0°

(b) *Propeller Angle* = 15°

(c) *Propeller Angle* = 30°

(d) *Propeller Angle* = 45°

(e) *Propeller Angle* = 60°

(f) *Propeller Angle* = 75°

Figure 4.22: *Isosurfaces and contours of vorticity during vortex-propeller interaction. The contour surface is taken from a vertical plane in the wing mesh at a span location of* $r/R_p = 0.97$.

As noted above, the vortex is severely bent when it interacts with the leading edge of the wing, and is not initially cut into two distinct sections. The distinction between vortex bending and vortex cutting is examined in the theoretical and computational work of Marshall and Yalamanchili [89, 90]. In this work, the ratio of wing thickness (T) to vortex core size (r_c) was shown to determine whether the vortex will be cut by the blade or bend around the blade surface. For $T/r_c < 1$, the vortex will be cut, producing two separate vortex sections on either side of the wing. For $T/r_c > 1$, the vortex will bend around the wing surface. In the present work, $T/r_c \approx 3$, which agrees well with the vortex bending that is observed as the vortex interacts with the wing. This bending is such that the vortex core is extended and the vortex axis will be near-parallel to the wing surface as it passes the leading edge of the wing. During this process, it is difficult to determine when the two sections of the vortex on either side of the wing become cut, as the vortex convects further downstream and the vortex is further bent. As the vortex axis is near-parallel to the wing surface, the creation of secondary vortices are seen, which have vorticity in the opposite sense to the primary vortex. These secondary vortices are labelled in Fig. 4.26 and Fig 4.27.

As the vortex bends around the leading edge of the wing, the upper and lower vortex sections move out of the spanwise plane shown in Fig. 4.22 and this movement is illustrated in Fig. 4.24. Initially, as the vortex approaches the wing, it will be displaced outward from the nacelle, labelled as *1* in Fig. 4.24. This movement is attributed to the image vortex in the surface of the wing inducing an outward velocity. The vortex is then bent around the leading edge and its two parts convect along the wing surface. On the upper side, the vortex section moves inboard and on the lower side it moves outboard, labelled as *2* in Fig. 4.24. This is caused by the lift force and associated spanwise flow that is induced on the wing due to the propeller wake, and acts to move the vortices. This lift also causes the vortex section on the upper surface of the wing to convect faster than the vortex on the lower surface. As a result of this, the two parts of the vortex pass the trailing edge at different span locations and at different times, resulting in a large shearing of the propeller wake, shown in Fig. 4.25.

Downstream of the trailing edge of the wing, the experimental study by Johnston and Sullivan [88] noted that the vortices undergo a complex reconnection process. In

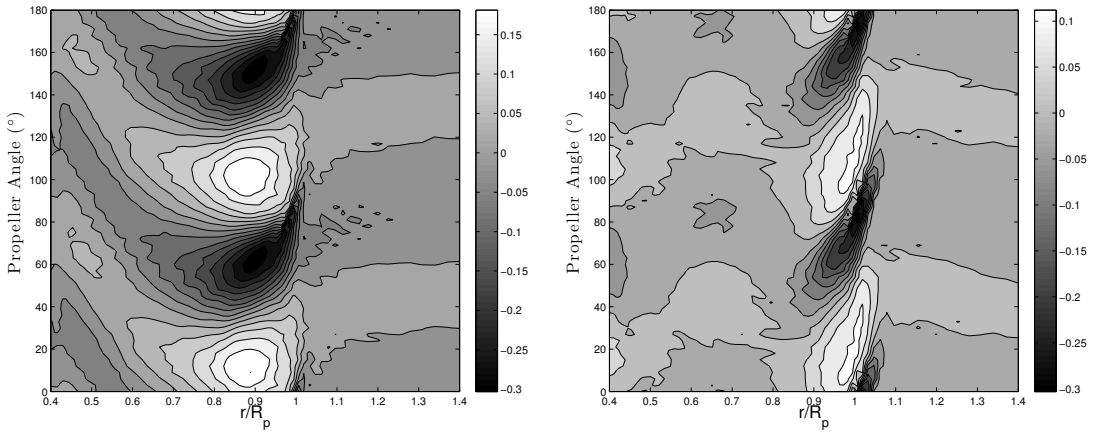

(a) C_P *on upper side of wing.* (b) C_P *on lower side of wing.*

Figure 4.23: *Perturbation spanwise* C_P *at* $0.04c$ *from leading edge of the wing.*

this experimental study it was noted that although the tip vortices do not regain their initial helical structure, the vortices likely reconnected through the shed and trailed vorticity of the wing, created by the interaction. This reconnection process is not clearly seen here, most likely because the vortex system diffuses in the coarse region of the mesh before this reconnection occurs.

The creation of vortices is also seen at the root section of the wing where the wing root is attached to the nacelle. These vortices are labelled in Fig 4.26 and Fig 4.27 for both sides of the wing and originate at the leading edge of the wing and develop along its span close to the nacelle. Vortices of this type appear in a large variety of flows where two solid surfaces meet at a sharp angle and are referred to as "necklace" or "horse shoe" vortices [4]. Previous studies have also revealed these structures when analysing propeller-wake interactions [91], and they will influence the local lift and drag at the wing root.

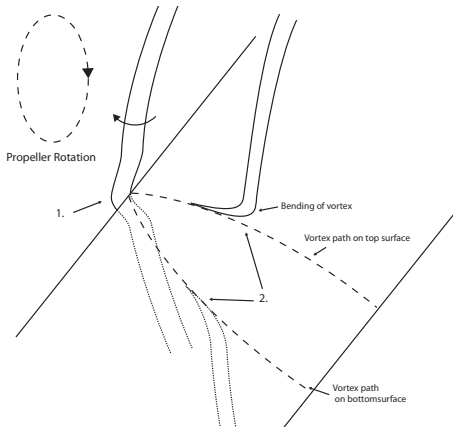

Figure 4.24: *Vortex movement during interaction.*

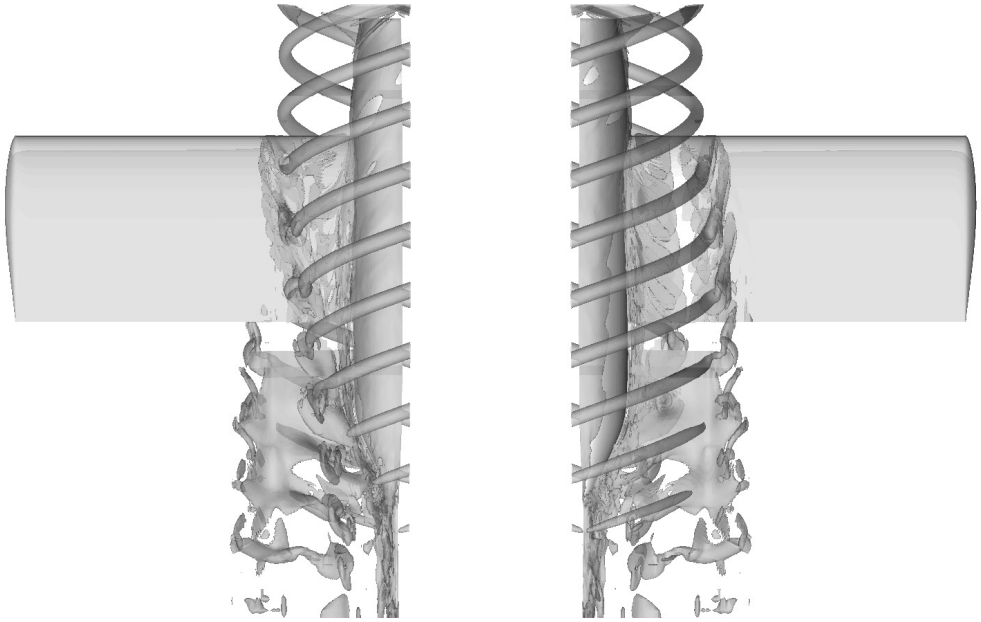

(a) *Vortices move inboard on the upper side of the wing*

(b) *Vortices move outboard on the lower side of the wing*

Figure 4.25: *Iso-surfaces of vorticity show the shear of the propeller wake due to the induced spanwise flow on the wing.*

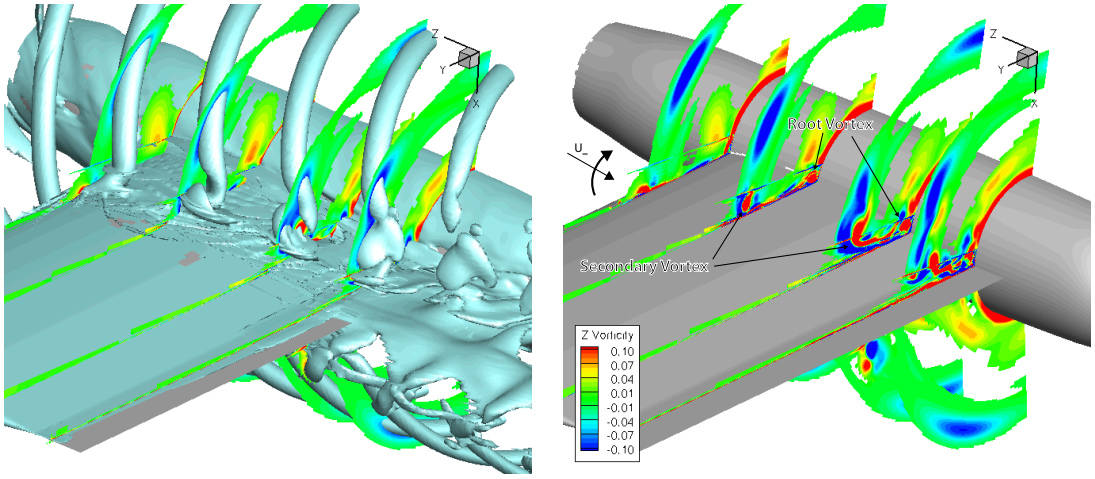

(a) *Isosurface of vorticity magnitude revealing wake structure.*

(b) *Contours of streamwise vorticity show the creation of root vortices.*

Figure 4.26: *Vortex created at root section on the upper side of the wing. Slices show streamwise vorticity, isosurface shows vorticity magnitude.*

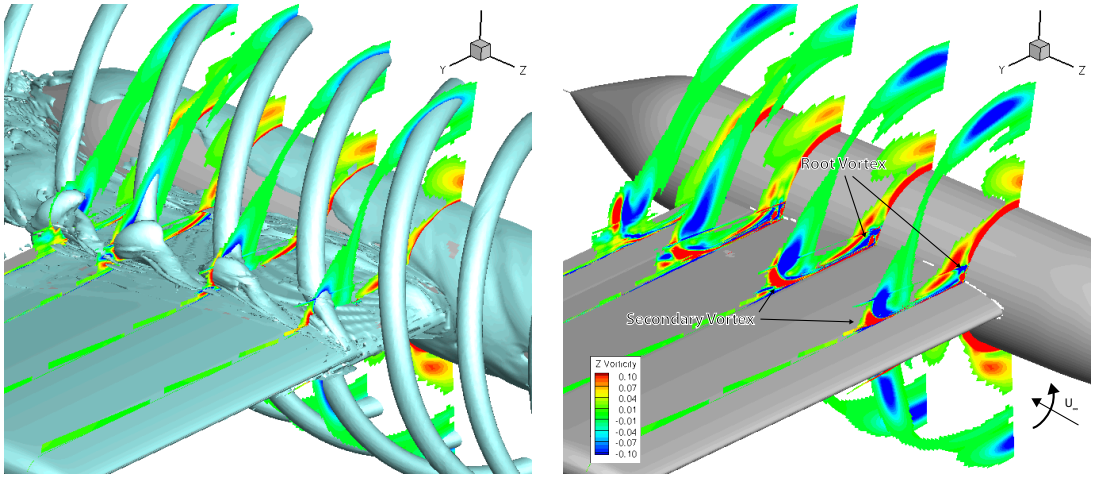

(a) *Isosurface of vorticity magnitude revealing wake structure.*

(b) *Contours of streamwise vorticity show the creation of root vortices.*

Figure 4.27: *Vortex created at root section on the lower side of the wing. Slices show streamwise vorticity, isosurface shows vorticity magnitude.*

4.3.4 Acoustics of Interaction

A significant disadvantage of turboprops is the large amount of noise that is radiated during their operation, of which a significant proportion is aerodynamic noise. As the rotor plane is typically nearly perpendicular to the ground plane, both thickness noise and loading noise have a significant contribution to the perceived noise level of a turboprop. In addition, advanced turboprop designs, that operate at higher Mach numbers in the region of Mach 0.7–0.8, will have supersonic flow around the outer regions of the blades. The shockwaves from this supersonic flow produce additional noise that is perceivable to observers based on the ground.

Due to the prominence of this noise, there has been much research towards methods that accurately predict the acoustics generated by the turboprop blades. Similar to helicopter aeroacoustic analysis, the Ffowcs Williams-Hawkings equation have proven successful in this analysis [92], as the majority of the rotor noise propagates from thickness or loading sources.

The scattering effect that an aircraft structure has on the sound propagated from the blades of a turboprop is known to alter its acoustic footprint. However, the acoustic noise originating from the wake of the propeller impacting on the wing in not usually considered. To investigate this noise source, the acoustics radiated from both the wing during the interaction and the turboprop blades are computed using the linear acoustic analysis. The acoustics are computed on a plane that is perpendicular to the wingspan at a span location of $r/R_p = 1$, the location of this plane is illustrated in Fig. 4.28(a). The sound pressure levels of the propeller blades, the wing and their combination are shown in Fig. 4.28.

The noise radiated from the propeller blades dominates the total acoustics. This noise is seen to radiate largely in the plane of the rotor. In comparison, the noise radiated from the wing is much lower, although is less directional and tends to propagate over a wider area. The combined acoustics of these two noise sources is largely similar to the acoustics of the propeller alone, but with the wing radiating lower level noise

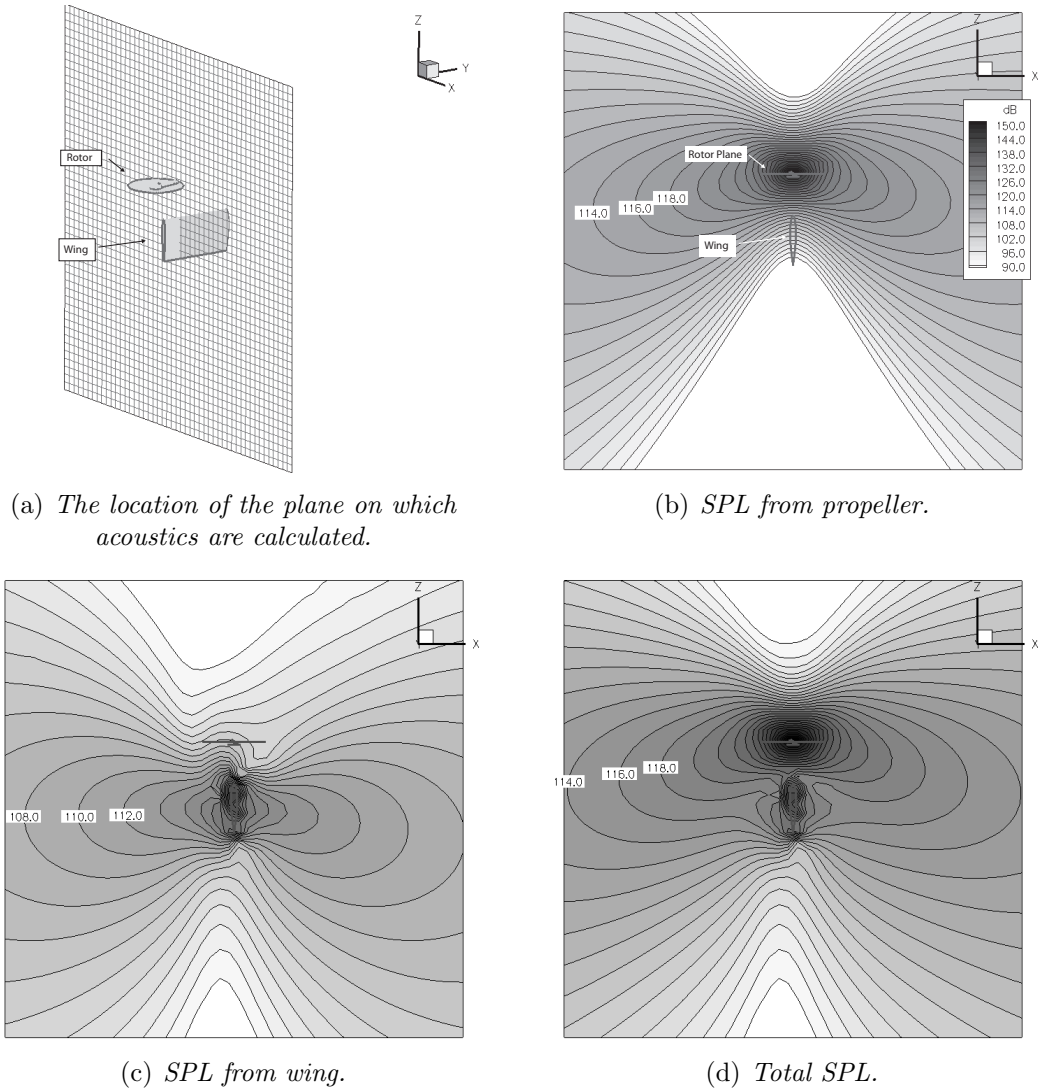

(a) *The location of the plane on which acoustics are calculated.*

(b) *SPL from propeller.*

(c) *SPL from wing.*

(d) *Total SPL.*

Figure 4.28: *SPL of the propeller and its wake interaction with the wing.*

over a wider area. These computations confirm that while the noise propagated from the wing is not negligible, it is significantly smaller that noise originating from the propeller blades.

4.4 Wing Design

The previous section showed that the wake of the propeller will cause large fluctuations in the lift and drag distribution across the wingspan, and that the details of this interaction can be accurately computed using the current computational methodology. The design of a novel wing is now studied with the aim of reducing the induced drag for a given lift.

The wing geometry used in the experiments of Samuelsson [44], which is shown in Fig. A.1, is studied here, but to create a more typical lift and drag distribution across the span, the wing is inclined at 5° to the freestream. Introducing this angle of attack removes any symmetry in the solution, so both wings must now be modelled. The computed (time-averaged) lift and drag across the span of this wing is shown in Fig. 4.29. Also shown for comparison is the lift and drag distribution across a "clean" wing without the effect of the propeller slipstream. The propeller slipstream causes the lift and drag distribution to depart drastically from the "clean" wing case, where the upwash and downwash of the propeller change the local angle of attack of the wing. In the upwash region, the wing experiences a large rise in lift and the resultant force vector is rotated forward such that there is a local thrust force on this region of the wing, shown in the Fig 4.29(b). Conversely, the downwash region of the wing has a reduced lifting force and in general an increase in sectional drag. This lift and drag distribution is not only affected by the propeller slipstream, but also by the modified trailed and shed wake of the wing.

Also shown is the ratio of C_d to C_l across the wing span giving an indication of how efficient each span section of the wing is at generating lift, where small values correspond to a large lifting force for a small drag penalty. The region in the upwash of the

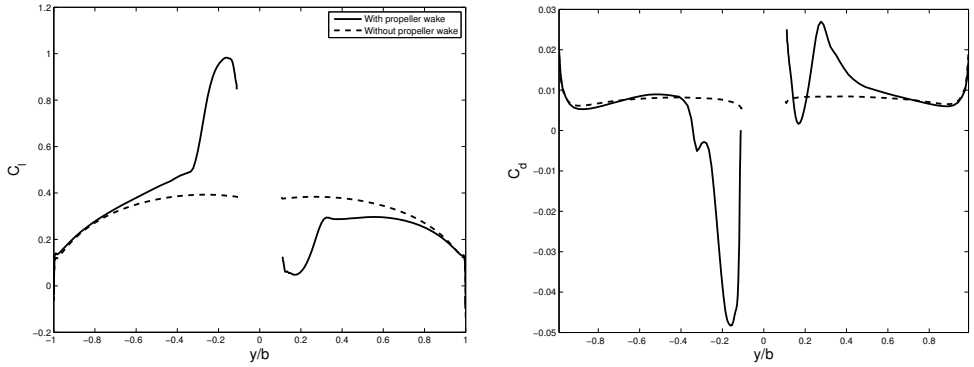

(a) C_l. (b) C_d.

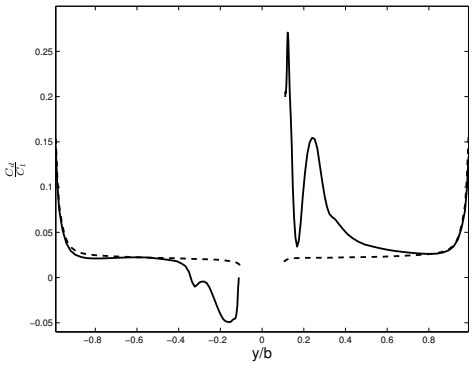

(c) $\frac{C_d}{C_l}$.

Figure 4.29: *Lift and drag variation across wing span immersed in the propeller slipstream. The lift distribution across a "clean" wing is also shown.*

turboprop wake has a negative value of C_d/C_l whereas the wing region in the propeller downwash has the highest values across the span. It is therefore desirable to design a wing that maximises the potential benefits of the upwash region and ameliorates the effects of the downwash region.

The lift and drag distribution across the span can be altered by varying the local aerofoil section, chord or twist of the wing. For simplicity, the present work will examine variations of the twist distribution of the wing, although the true optimal solution is likely to result from a combination of all three. The twist distribution along the wing span can be described by a Bézier curve, which has the following form:

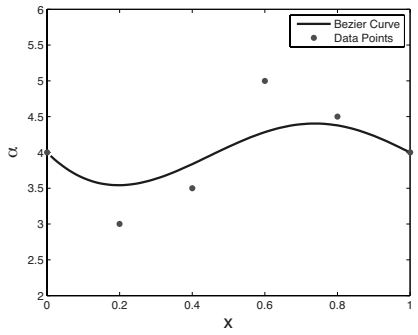

Figure 4.30: *A 5^{th} order Bézier curve defined by 6 control points.*

$$\begin{aligned} B(t) &= \sum_{i=0}^{d} \frac{d!}{i!(d-i)!}(1-t)^{(d-i)}\mathbf{P}_i \\ \mathbf{P}_i &= \begin{bmatrix} x_i \\ N_i \end{bmatrix} \end{aligned} \tag{4.1}$$

where d is the degree of the Bézier curve and $0 \geq t \geq 1$ is a free parameter varying. $\mathbf{P}_i$ are the control points that describe the twist distribution, where the value N_i is a specified value of the twist at the location x_i. A Bézier curve is chosen as it produces a smooth distribution which avoids the Runge's phenomenon. A Bézier curve reconstruction of 6 data points is shown in Fig. 4.30, which produces a 5^{th} degree polynomial. This curve produced a smooth representation of the data that in general only intersects the first and last points. To determine the value of the control points, the CFD solver is coupled to an optimisation algorithm.

4.4.1 Optimisation Algorithm Implementation

To perform an optimisation analysis of the wing immersed in the wake of a propeller, the toolkit DAKOTA (Design Analysis Kit for Optimization and Terascale Applications) is used [93]. The DAKOTA toolkit was developed by the Sandia National Laboratories

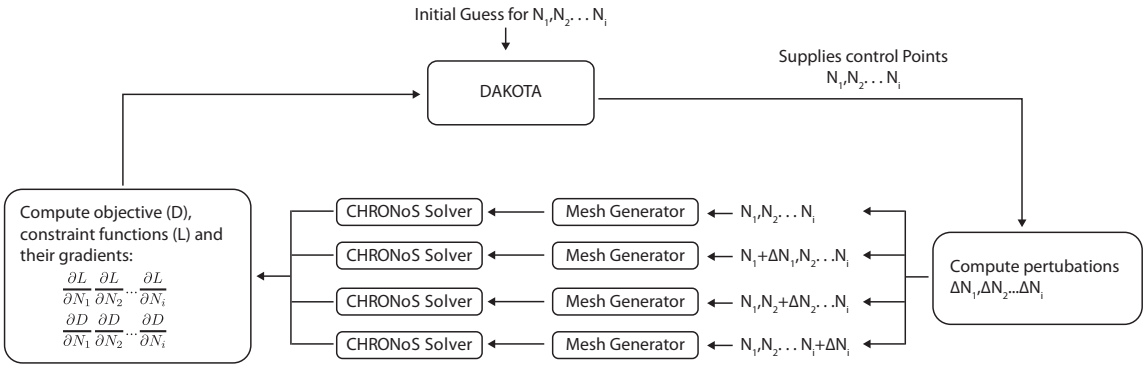

Figure 4.31: *Flow chart of the DAKOTA algorithm coupled with the CHRONoS solver.*

and provides a flexible interface between simulation codes and a variety of iterative system analysis methods, including optimisation, uncertainty quantification, nonlinear least squares methods, and sensitivity/variance analysis.

DAKOTA's optimisation capabilities are utilised which includes a variety of gradient and non-gradient based methods. Variations in the wing twist distribution produces a non-linear relationship to the lift and drag across the wing. This combined with the non-linear constraints of the problem are best suited by a gradient based quasi-Newtonian method, as suggested by Sandia National Laboratories [93].

The quasi-Newton approach is a gradient based iterative optimisation scheme, where the optimal solution is obtained through successive *function evaluations*. For the present problem, the optimal values of the design variables that describe the twist are sought, which are the variables N_i in equation 4.1. For each function evaluation, the value of the objective function and any constraint functions are needed, and for the present problem these are the drag and lift of the wing respectively. The gradients of both the objective and constraint function with respect to each of the design variables, N_i, are also required at each function evaluation. These are computed in parallel using finite difference and supplied to the DAKOTA code. The interfacing between the optimisation algorithm and the flow solver is performed by a Korn Shell script, implemented in a UNIX environment and the process is summarised in Fig. 4.31.

4.4.2 Wing Twist Optimisation

The twist distribution across the wing span is described by two 4^{th} order Bézier curves, for the upwash and the downwash side of the nacelle respectively. Each curve requires 5 control points at 5 spanwise locations. To examine the influence of the twist in the region immersed in the propeller wake, 3 of these control points are held constant, and two are free to vary on each wing. These varying control points influence the twist distribution of the wing in the region immediately behind the propeller, and their location is illustrated in Fig 4.32. This results in an optimisation with 4 varying parameters and thus for each function evaluation, 5 solutions from the flow solver are required to calculate the appropriate gradients.

The optimisation process is iterative and depends on successive function evaluations. To reduce the computational cost of each evaluation, the low-resolution mesh examined in the previous section is used which has a spatial resolution of 4 points across the vortex core. This mesh was seen to slightly dissipate the vortical structures but retained much of the important flow features of the higher resolution mesh. In addition, each function evaluation was started from a previously converged flow solution imposed on the new geometry. This resulted in every simulation only needing to be performed for two propeller revolutions for the lift and drag of the new geometry to converge. Each flow solution requires 6 CPUs, therefore requiring 30 CPUs for each function evaluation, which took a minimum run-time of approximately 26 hours to complete. However, this run-time was often longer due to non-optimal load distribution across the computing cluster.

The control points N_1, N_2, N_3, and N_4 are shown in Fig. 4.33 for 15 function evaluations. The largest changes in the control values between each function evaluation occur at the beginning of the optimisation process, and become successively smaller as the optimisation progresses and the control points converge. The final twist distribution is shown in Fig. 4.34(b) where the local angle of attack has decreased on the upwash side of the nacelle and increased on the downwash side. This results in a wing which more efficiently recovers some of the swirl energy imparted to the flow from the propeller

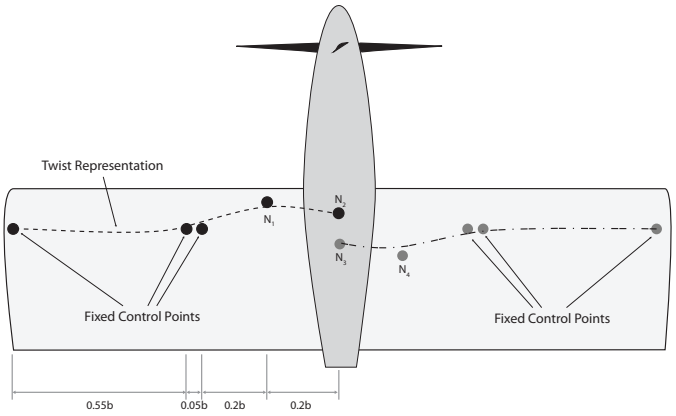

Figure 4.32: *Control point locations that describe chord distribution.*

and is characteristically similar to other lower order optimisation results [48]. The total lift and drag is shown in Fig. 4.34(a), where the optimised wing design has resulted in approximately 5% reduction in induced drag while maintaining the initial lift. The initial and optimal wing designs are compared in Fig. 4.35 where the spanwise lift and drag are compared.

4.4.3 Validity of Results

The analysis presented here is based on the solution of the Euler equations and does not model the viscosity of the fluid. The skin friction drag caused by fluid viscosity has therefore not been accounted for in the present optimisation analysis of the wing twist yet in real flows, this drag may not be negligible.

Previous propeller-wing optimisation studies by Veldhuis [48, 94] based on a lifting line analysis attempted to account for the local viscous drag by using an empirical relationship to the local lift. In this study, the optimised wing twist for the induced drag and the total drag were compared. The analysis showed differences in these two optimised designs, however these differences were small and both wing twist distributions were qualitatively the same. This analysis however, approximated the propeller wake as a steady increase in axial and swirl velocity, neglecting any unsteady effects.

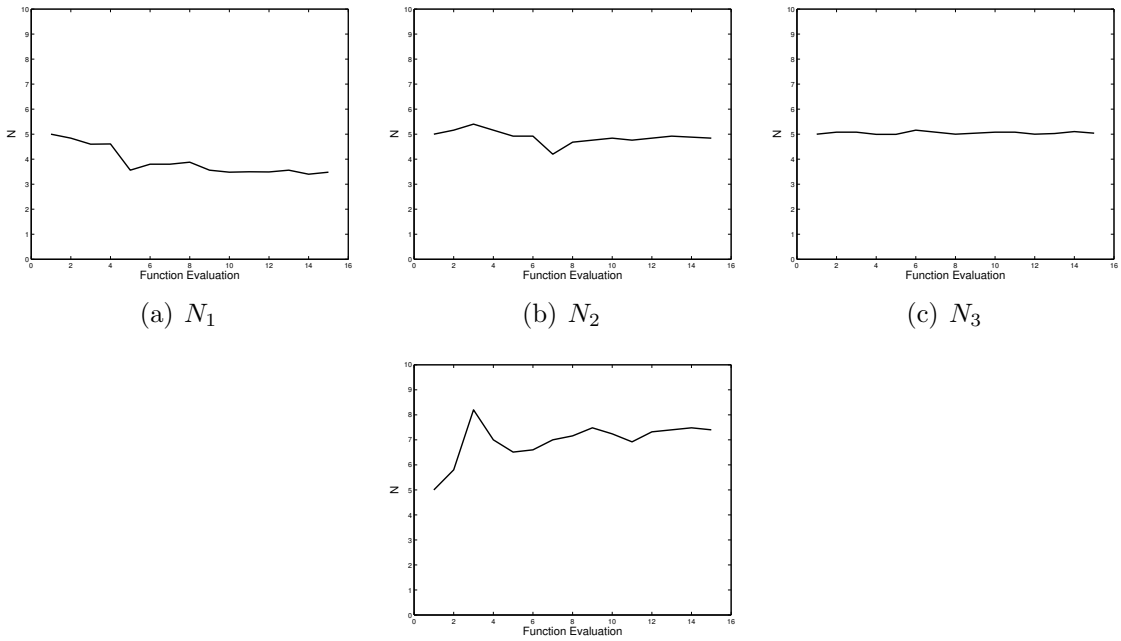

(a) N_1 (b) N_2 (c) N_3

(d) N_4

Figure 4.33: *Control points during optimisation.*

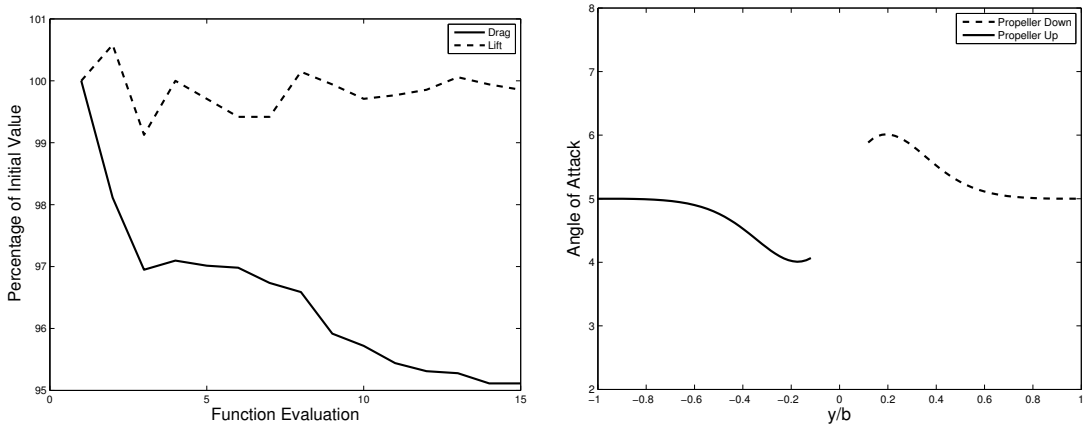

(a) *Lift and drag reduction during optimisation* (b) *Optimised twist distribution of wing.*

Figure 4.34: *Optimisation results.*

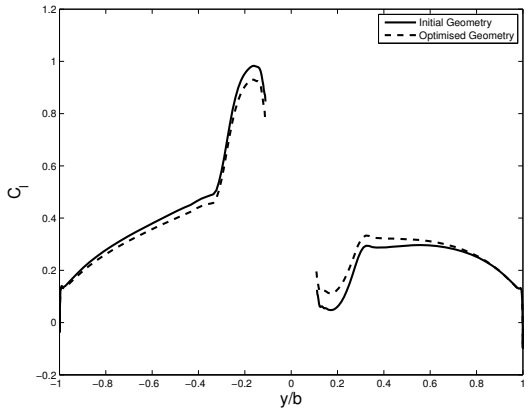

(a) C_l.

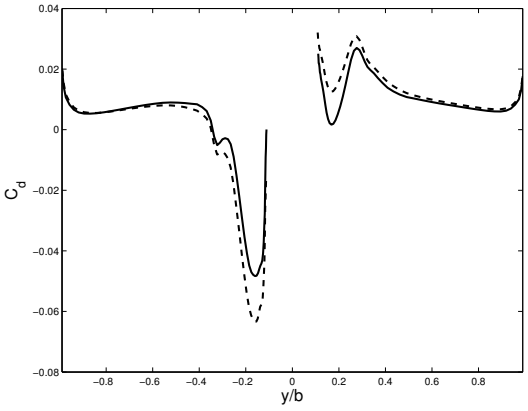

(b) C_d.

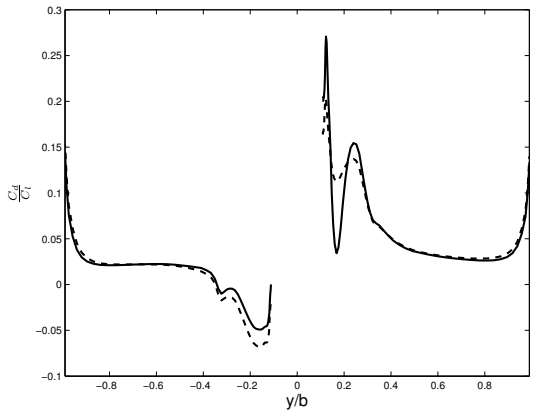

(c) $\frac{C_d}{C_l}$.

Figure 4.35: *Spanwise lift and drag of optimised wing compared to initial geometry.*

Previous experimental studies [95] have shown that the passage of the propeller wake over the wing causes a rise in boundary layer turbulence and the associated skin friction drag. An unsteady analysis of the propeller wake is therefore needed to gain an accurate prediction of the skin friction drag.

The present methodology could be easily extended to model the skin friction by including the viscous terms in the governing equations and utilising an appropriate turbulence model. This will require a much finer resolution in the boundary layer which will increase the computational expense.

4.5 Summary and Implications

The idealised propeller-wing interaction experiments performed by Samuelsson [45, 46] are studied using the current methodology. This experiment involved a highly loaded turboprop mounted in a tractor configuration on a wing. Initially, an isolated propeller is resolved and the wake data is compared to experimental measurements. It is found that the axial and swirl velocity can be accurately resolved many rotor diameters downstream of the propeller. The velocity within the wake is seen to vary largely in both the azimuthal and radial direction.

The interaction of the propeller wake with a wing is then considered. The propeller wake is introduced into the flow as an unsteady boundary condition, and it is seen that this produces an accurate wake that is preserved against numerical dissipation provided the error from the time integration scheme is sufficiently minimised. The interaction of the wake with the wing is seen to produce highly unsteady lift and drag forces on the wing. The pressure on the wing surface is compared to experimental data, and it is shown that the current approach can accurately resolve the time-averaged forces.

The current methodology also resolves the intricate wake dynamics as the tip vortices from the propeller convect over the wing. The tip vortices are seen to either move inboard or outboard due to the induced flow across the wing span, producing a large

shearing of the propeller wake. The tip vortices are also seen to bend around the leading edge of the wing. This bending causes the swirl velocity of the vortex to impact more directly onto the wing surface, producing a large variation in surface pressure especially on the upper surface.

The design of a wing which accounts for this interaction is then studied by coupling the current CFD solver to the optimisation algorithm DAKOTA. A quasi-Newton gradient-based optimisation scheme is utilised to modify the twist distribution of the wing in the region immersed in the propeller wake. This optimisation attempts to minimise the induced drag while maintaining the initial lift distribution. This optimisation produces a wing where the local twist rotates the wing into the swirl velocity of the propeller wake, and results in a 5% induced drag reduction.

The implication of this work is to show that the important inviscid phenomenon of a propeller-wing interaction can be accounted for using the current methodology. The tip vortices and their interaction with a wing can be accurately resolved and the intricate wake details are seen. In addition, this analysis can be used in the design process of a wing, enabling efficient propeller-wing integration. Small changes in the twist distribution can yield benefits in the form of a drag reduction, and these should be considered for efficient propeller-wing integration.

Chapter 5

Conclusions and Further Work

The interaction of a vortex with a lifting surface is significant to the operation of many aircraft, and accurate modelling and analysis of these interactions is essential for future design. This thesis develops and applies a high fidelity flow solver to the analysis of the aerodynamics and aeroacoustics of two vortex-lifting surface interaction problems: blade-vortex interactions on a helicopter rotor, and propeller wake-wing interactions behind a tractor mounted turboprop. Proper analysis of both these problems require the accurate modelling of strong tip vortex structures and their subsequent interaction with a lifting surface.

Some previous studies have analysed these interactions using lower fidelity models, but have shown that these models are of limited use, especially when attempting to resolve cases where the vortex is severely distorted by the interaction. Other studies have used higher fidelity CFD analysis, which is capable of resolving the important flow features. However, these studies have been afflicted by numerical dissipation that strongly diffuses the tip vortex structures.

The high fidelity flow solver CHRONoS has previously shown promising results resolving tip vortex formation and convection, and in the present work this solver is modified to facilitate the efficient analysis of vortex-lifting surface interaction problems.

The governing equations of the flow are solved implicitly in time and in present work, the temporal accuracy was increased by implementing a second order backward differencing time integration scheme. Increasing the time integration accuracy is necessary to reduce the numerical dissipation of vortical flow structures as they convect through the solution domain for unsteady flow calculations. To improve numerical stability and convergence within each timestep, dual time stepping was implemented. This allows fewer sub-iterations to be taken within each timestep, increasing the efficiency of the computations.

Moving overset meshes are used to discretise the solution domain, as this allows high quality spatial discretisation of complex geometries and mesh points to be easily clustered in the solution domain. As an overset mesh moves through the solution domain, its boundary points are required to be updated at every timestep. A stencil walking algorithm was implemented to efficiently search for the correct boundary points at every timestep, and it was demonstrated that this method can efficiently update the boundary points for the mesh topologies used in the present work.

These modifications allow the high fidelity flow solver to be used for the efficient analysis of unsteady aerodynamic problems involving vortex-lifting surface interactions. For all calculations, a careful mesh and timestep convergence study is performed to ensure that the results are not affected by numerical error and to confirm that the calculations asymptote to the physically correct solution.

5.1 Blade-Vortex Interaction Study

An idealised BVI is considered where an independent vortex is generated upstream from a static wing. This vortex then interacts with a non-lifting rotor downstream, and for this case high quality experimental surface pressures and acoustic data is available. The following conclusions are found:

- The expected laminar and turbulent diffusion of the vortices considered here is calculated using the expressions derived by Lamb [80] and Squire [81]. This diffusion is found to be negligible, and numerical diffusion is seen to be potentially far greater when resolving tip vortex convection. The current computational methodology is capable of accurately resolving the formation and convection of a tip vortex accurately, provided a spatial resolution of at least approximately 8 points across the vortex core and adequate temporal resolution are used. For a 2D AVI simulation, the vortex structure is initiated as a perturbation in the flow using an empirical vortex model and the constant enthalpy condition, and convects through the solution domain with negligible numerical dissipation. For 3D BVI simulations, the tip vortex formation is accurately resolved and its swirl velocity and core size compare well with the experimental data.

- The current inviscid methodology is capable of accurately resolving the blade forces produced by BVIs over a range of vortex-blade miss distances. Experimental blade surface pressures can be reproduced, and the detailed propagation of the primary and secondary BVI pressure waves on the aerofoil surface are observed. A strong interaction, where the vortex core impacts directly with the blade, causes the vortex structure to become severely distorted. During a weak interaction, the blade does not penetrate the vortex core and the vortex structure is largely unaltered.

- The rotor geometry of a BVI can be accurately represented using moving overset meshes, provided sufficient care is taken to ensure that the vortical structures are accurately transferred between meshes. It is observed that the passage of vortices into a moving overset mesh can cause significant distortion to the vortex structure. This distortion is largely attributed to time integration errors, and by increasing the accuracy of the time integration scheme and refining the timestep, the diffusion of the vortex is largely reduced such that the correct vortex profile is recovered. For the present study, a timestep equivalent to 0.125° of rotor rotation and second order accurate time integration is seen to sufficiently preserve the vortex structures. Increasing the interpolation accuracy to a tricubic scheme using 64 donor points was found to have a beneficial but small effect on interpolating the vortex structure between meshes.

- The far-field acoustics can be accurately predicted using a linear acoustic solver based on the Ffowcs-Williams Hawkings equation provided that the surface pressures are accurately computed. This method has been used to compute three dimensional acoustic surfaces of the SPL of the interaction where the loading noise is see to radiate as two large lobes above and below the rotor plane. The near-field acoustics computed using a linear acoustic analysis are less accurate, due to the omission of the volumetric noise sources surrounding the blade. However, the near-field acoustics are accurately computed in the CFD flow solution, provided sufficient spatial resolution is used to preserve the acoustic wave propagation.

5.1.1 Recommendations for Future Work

The three-dimensional computations presented in this thesis have shown that the current methodology is capable of resolving all the important flow features of a blade-vortex interaction. The next logical step is to extend the present work to resolve a rotor undergoing self-induced BVI, where the rotor blades interact with their own wake system. The flexibility of moving overset meshes allows the modelling of complex geometry but maintaining a minimal spatial resolution of 8 points across the core of the vortex throughout the simulation will be computationally expensive.

For larger computations, it will be advantageous to implement numerical methods that reduce the numerical error present in the discretised time integration, allowing larger timesteps while accurately maintaining the vortex structure and strength. This can be achieved through the use of higher order accurate time integration and multi-dimensional advection schemes [96]. The flexibility of the current CFD solver means that such improvements could be implemented relatively easily.

The present idealised computational study could also be used in the design of novel quiet blades. Both passive and active helicopter blade designs, such as active higher harmonic control or novel blade platforms, could potentially reduce BVI noise. These

designs aim to reduce the perceived noise of the rotor to an observer on the ground and the computational methods presented in this thesis could help develop these concepts in an idealised interaction framework.

5.2 Propeller Wake-Wing Interaction Study

The idealised interaction of the wake of a 4 bladed turboprop and a wing is considered where the turboprop is mounted in a tractor configuration and is operated at a high thrust, creating a strong wake system. This wake interacts downstream with a wing that is mounted at zero incidence to the freestream. Experimental surface pressures and wake velocities are available for comparison and the following conclusions are found:

- The axial and swirl velocity in the wake of an isolated turboprop can be accurately modelled by the current methodology, and this wake can be accurately preserved to several rotor diameters downstream of the rotor plane. Close to the propeller plane the computed results show a small discrepancy with experimental data, which is partially attributed to viscous effects in the wake formation. However, further downstream, the computed propeller wake is seen to be in excellent agreement with experimental data. Within the wake, large variations in axial, swirl and radial velocity are seen, which are largely induced by the tip vortex and the smaller root vortex.

- The interaction of the wing and the propeller wake is shown to be accurately modelled by imposing the wake of an isolated propeller as an unsteady boundary condition. The wake is seen to convect accurately through the computational domain provided the time integration is of sufficient accuracy. For the present case, a timestep equivalent to 0.125° of propeller rotation was seen to accurately preserve the propeller wake. This approach reduces the computational cost significantly, but has the disadvantage of not accounting for the influence of the wing on the propeller and the development of its wake. However, this effect is thought to be small for the present case, due to the large separation distance of

the propeller and wing. The interaction was validated by comparing the computed wing surface pressures with experimental data. The propeller wake is seen to induced a lifting and drag force on the wing, which is relatively unsteady at $r/R_P \approx 1$, where the tip vortices impact onto the wing.

- The dynamics of the wake as it interacts with the wing are observed, where the entire wake is seen to shear as it convects across the chord of the wing. This shearing of the wake is caused by the induced spanwise flow on the wing which move the tip vortices across the wing span. As the tip vortices encounter the leading edge of the wing, they are severely bend around the wing surface causing the axis of the vortex to lie parallel to the wing surface. This bending is due to the large ratio of wing thickness to vortex core size, $T/r_c \approx 3$.

- The impact of the propeller wake on the wing is a source of aeroacoustic noise, but the magnitude of this noise is small in comparison to the acoustic energy radiated from the propeller. As the rotor plane of a turboprop will, in general, be near perpendicular to the ground plane, the thickness noise of the rotor blades will radiate towards the ground, and will be far greater than the noise generated from the wake-wing interactions.

- The method was used to reduce induced drag for a given lift by altering the circulation distribution of the wing immersed in the propeller wake. To study this, the CFD solver was coupled to an optimisation algorithm utilising a quasi-Newton, gradient method. The twist distribution of the wing is altered during the optimisation process, and the optimised wing twist geometry tends to rotate the local aerofoil section into the swirl velocity of the propeller wake. The optimised wing achieves an induced drag reduction of approximately 5% while maintaining the initial lift for the case studied.

5.2.1 Recommendations for Future Work

The present work introduces the effect of the propeller into the flow as an unsteady boundary condition. As previously mentioned, this method, although considerably

more computationally efficient, does not model the influence of the wing on the propeller. The wing can influence the propeller inflow, especially for a case with a small propeller-wing separation. This influences can be assessed by fully modelling the interaction, where the flow around the turboprop blades, the nacelle and the wing is resolved. This will be considerably more computationally expensive that imposing the propeller wake as an unsteady boundary condition, but the current methodology is capable of resolving the full interaction, give sufficient computational resources.

Viscous effects are also not modelled in the present work and therefore any drag forces resulting from the viscosity of the fluid have not been accounted for. This effect could be accounted for by including the viscous terms in the governing equations with an appropriate turbulence model and resolving the boundary layer of the surfaces. It is expected that the optimised wing geometry will be characteristically similar to the inviscid optimised geometry, as indicated by previous studies using lower fidelity models [48], and that significant drag reductions are still achievable.

The interaction considered in the present work represents an idealisation of a real interaction. A realistic case will be more complex, involving the effect of the fuselage and a realistic wing with potentially multiple engines. As the complexity increases, the use of a high fidelity CFD solver become prohibitively expensive for optimisation analysis, but lower fidelity methods remain feasible. Therefore, a comprehensive comparison of lower fidelity methods to the current CFD solver to assess their limitations and usefulness is necessary. A lower fidelity method could conceivably be used for preliminary design, and this design validated and refined with CFD analysis.

Appendix A

Propeller and Nacelle Geometry Details

The geometry of the nacelle and propeller are detailed in this section. The coordinates system used is defined in Fig. A.1, where the streamwise direction, x, and the radial direction, r, are shown. As mentioned in Chapter 4, this geometry is slightly modified from the experimental setup to guarantee high quality meshes generation. The propeller twist and chord distributions are defined in Table A.1, and details of the aerofoil sections used are shown in Fig. A.2. This propeller has an aspect ratio of 7, when its span is defined from the centre of the nacelle to its tip. The geometry of the nacelle is given in Table A.2.

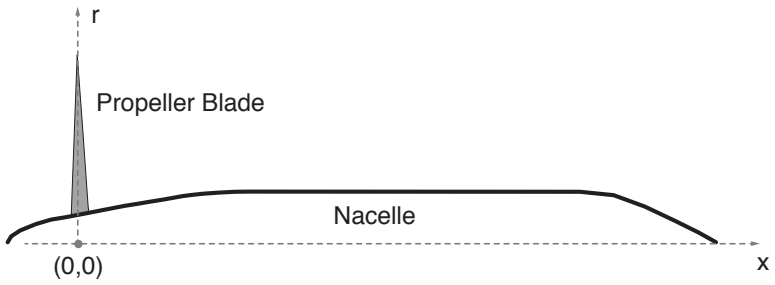

Figure A.1: *Side view of the nacelle detailing the coordinate directions.*

r/R	Chord (c)	Twist (°)
0.2000	1.0000	56.7431
0.2500	1.0000	51.3025
0.3000	1.0000	46.9850
0.3500	1.0000	43.5190
0.4000	1.0000	40.6833
0.4500	1.0000	38.3074
0.5000	1.0000	36.2631
0.5500	1.0000	34.4538
0.6000	1.0000	32.8069
0.6500	1.0000	31.2669
0.7000	0.9895	29.7912
0.7500	0.9940	28.3468
0.8000	0.9875	26.9076
0.8500	0.9611	25.4528
0.9000	0.8939	23.9659
0.9500	0.7325	22.4333
1.0000	0.5134	20.8439

Table A.1: *Propeller chord and twist geometry. Twist given relative to propeller plane.*

x (c)	r (c)
-3.0500	-0.0000
-2.8787	0.2776
-2.4564	0.5532
-1.7155	0.8611
-1.0095	1.0646
-0.3214	1.1810
0.5682	1.3481
1.5923	1.5490
2.4652	1.7162
3.1700	1.8325
3.5895	1.8988
4.2943	2.0151
5.2342	2.1818
5.7541	2.2473
6.2235	2.2958
6.9107	2.3425
7.6729	2.3798
8.4181	2.3911
23.9637	2.3855
25.5604	2.2241
27.0264	1.6888
28.4570	1.0143
29.5877	0.4469
30.3850	0.0000

Table A.2: *Nacelle geometry.*

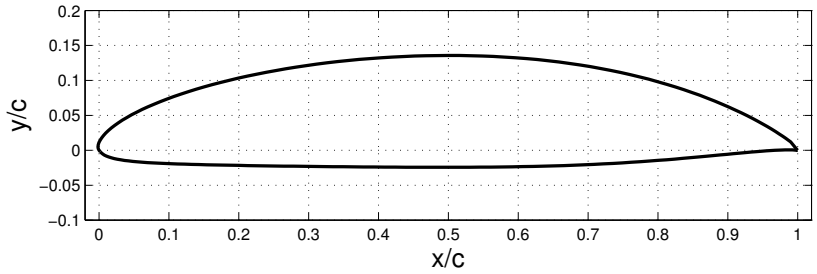

(a) *Aerofoil section at* $r/R = 0.2$.

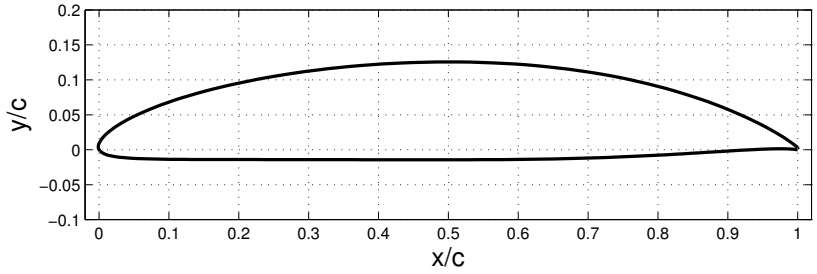

(b) *Aerofoil section at* $r/R = 0.4$.

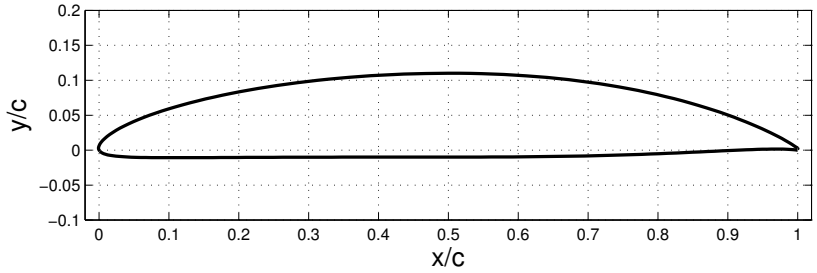

(c) *Aerofoil section at* $r/R = 0.67$.

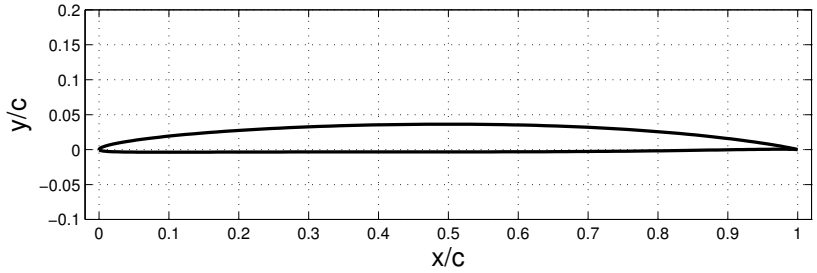

(d) *Aerofoil section at* $r/R = 1.0$.

Figure A.2: *Aerofoil section details at various propeller span locations.*

Appendix B

Practical Computation Details

The simulations were performed in parallel where one master and several slave CPUs were used. The computational domain was split by distributing each overset mesh to a single slave CPU. The master CPU is then used to communicate flow information between the appropriate slave CPUs, where the boundary conditions are updated every timestep. In order to efficiently utilise each CPU, each mesh should contain approximately the same number of mesh cells, thus distributing the load approximately equally. The CPUs used were Intel Xeon "Gainstown" 2.40GHz processors, each with access to a shared RAM of 12 GB between 8 CPUs. To illustrate the computational cost, details of the unsteady 3D BVI simulation described in Chapter 3.3 are given.

For this computation, each iteration, containing 15 sub-iterations, took approximately 280 seconds to complete. The breakdown of this time is given in Table B.1. RHS and LHS refers to the computing of the right and left hand side of equation 2.18, respectively. Interpolation refers to the interpolation of data between the boundary and donor points of the meshes. Grid rotation refers to the updating of the grid position and boundary point information for unsteady calculations. The largest computational cost is the interpolation of data between CPUs, which accounts for 39% of the CPU time every iteration. This value depends largely on the position of the CPUs on the computing cluster. If the CPUs used are distributed on the same blade, the interpola-

Procedure	CPU time
LHS Inversion	21%
RHS	35%
Interpolation	39%
Grid Rotation	5%

Table B.1: *CPU time breakdown.*

tion time is dramatically reduced. However, in normal operation, the CPUs are spread across several blades resulting in the large interpolation times noted here.

References

[1] Argelles, P., Bischoff, M., Busquin, P., Droste, B., Evans, S. R., Krll, W., Lagardre, J.-L., Lumsden, J., Ranque, D., Rasmussen, S., Reutlinger, P., Robins, S. R., Terho, H., Wittlv, A., and Lina, A., "European Aeronautics: A Vision for 2020," Tech. rep., European Commission, 2001.

[2] Garcia, A., Bettignies-Thibaux, B., Chivers, P., Desvalles, P., Junior, A., Kingcombe, R., Laroche, M., Latella, C., Martin-Hernandez, J., Moeller, U., Pilon, N., Ritchey, I., Side, S., and Young, D., "Aeronautics and Air Transport: Beyond Vision 2020 (Towards 2050)," Tech. rep., Advisory Council for Aeronautics Research in Europe, 2010.

[3] Dareck, M., Edelstenn, C., Ender, T., Fernande, E., Hartman, P., Herteman, J., Kerkloh, M., King, I., Ky, P., Mathieu, M., Orsi, G., Schotman, G., Smith, C., and Wrne, J., "Flightpath 2050 Europes Vision for Aviation," Tech. rep., European Commission, 2011.

[4] Lugt, H., *Vortex Flow in Nature and Technology*, John Wilsey and Sons, 1983.

[5] Kuethe, A. and Chow, C.-Y., *Foundations of Aerodynamcis*, John Wiley & Sons, 1986.

[6] Leishman, J. G., *Principles of Helicopter Aerodynamics, Second Edition*, Cambridge University Press, 2006.

[7] Hirsch, C., *Numerical Computation of Internal and External Flows: Fundementals of Computational Fluid Dynamics, Second Edition*, Elsever, 2007.

[8] McCluer, M., "Helicopter Blade-Vortex Interaction Noise with Comparisons to CFD Calculations," Technical Memorandum TM-110423, NASA Ames Research Center, Moffett Field, CA, December 1996.

[9] Leverton, J. and Taylor, F., "Helicopter Blade Slap," *Journal of Sound and Vibration*, Vol. 4, No. 4, 1966, pp. 345–357.

[10] Schmitz, F. and Boxwell, D., "In-Flight Far-Field Measurement of Helicopter Impulsive Noise," *Journal of the American Helicopter Society*, Vol. 21, No. 4, 1976, pp. 2–16.

[11] Boxwell, D. and Schmitz, F., "Full-Scale Measurements of Blade-Vortex Interaction Noise," *Journal of the American Helicopter Society*, Vol. 27, No. 4, 1982, pp. 11–27.

[12] Kube, R., Splettstoesser, W. R., Wagner, W., Seelhorst, U., Yu, Y. H., Tung, C., Beaumier, P., J. Prieur, G. Rahier, P. S., Boutier, A., Brooks, T. F., Burley, C. L., Boyd, D. D., Mercker, E., and Pengel, K., "HHC aeroacoustic rotor tests in the German-Dutch wind tunnel: Improving physical understanding and prediction codes," *Aerospace Science and Technology*, Vol. 2, No. 3, 1998, pp. 177–190.

[13] van der Wall, B., Junker, B., Burley, C., Brooks, T., Yu, Y., Tung, C., Raffel, M., Richard, H., Wagner, W., Mercker, E., Pengel, K., Holthusen, H., Beaumier, P., and Delrieux, Y., "The HART II test in the LLF of the DNW - a Major Step towards Rotor Wake Understanding," *Proceedings of the 28th European Rotorcraft Forum*, Bristol, England, 2002.

[14] van der Wall, B. G., Burley, C., Yu, Y., Richard, H., Pengel, K., and Beaumier, P., "The HART II test measurement of helicopter rotor wakes," *Aerospace Science and Technology*, Vol. 8, No. 4, 2004, pp. 273–284.

[15] Lee, S. and Bershader, D., "Head-On Parallel Blade-Vortex Interaction," *AIAA Journal*, Vol. 32, No. 1, 1994, pp. 16–22.

[16] Surendraiah, M., "An experimental study of rotor blade-vortex interaction," Tech. Rep. CR-1573, NASA, May 1970.

[17] Horner, M. B., Saliveros, E., Kokkalis, A., and Galbraith, R. A. M., "Results from a set of low speed blade-vortex interaction experiments," *Experiments in Fluids*, Vol. 14, No. 5, 1993, pp. 341–352.

[18] Caradonna, F. and Kitaplioglu, C., "A Study of Blade-Vortex Interaction Aeroacoustics Utilizing an Independently Generated Vortex," *AGARD Symposium*, Berlin, Germany, 10–14 October 1994.

[19] Kitaplioglu, C., Caradonna, F. X., and McCluer, M., "An Experimental Study of Parallel Blade-Vortex Interaction Aerodynamics and Acoustics Utilizing an Independently Generated Vortex," Tech. Rep. TM1999-20879, NASA Ames Research Center, Moffett Field, CA, July 1999.

[20] McAlister, K. W. and Takahashi, R. K., "NACA 0015 Wing Pressure and Trailing Vortex Measurements," Technical Paper 3151, NASA Ames Research Center, Moffett Field, CA, November 1991.

[21] Widnall, S., "Helicopter Noise Due to Blade-Vortex Interactions," *Journal of the Acoustical Society of America*, Vol. 50, No. 1, 1971, pp. 354–365.

[22] Leishman, J., "Aeroacoustics of 2-D and 3-D blade vortex interaction using the indicial method," *52nd Annual Forum Proceedings*, American Helicopter Society, Washington, D.C., June 1996.

[23] Leishman, J., "Sound Directivity Generated by Helicopter Rotors using Wave Tracing Concepts," *Journal of Sound and Vibration*, Vol. 221, No. 3, 1999, pp. 415–441.

[24] Bridgeman, J. O., Ramachandran, K., Caradonna, F. X., and Prichard, D. S., "A Computational Analysis of Parallel Blade-Vortex Interactions Using Vorticity Embedding," *American Helicopter Society 50th Annual Forum Proceedings*, American Helicopter Society, Washington, D.C, May 1994.

[25] Torok, M. and Berezin, C., "Aerodynamic and Wake Methodology Evaluation using Model UH-60A Experimental Data," *Journal of the Acoustical Society of America*, Vol. 39, No. 2, 1994, pp. 21–30.

[26] Srinivasan, G. R., McCroskey, W., and Baeder, J., "Aerodynamics of Two-Dimensional Blade-Vortex Interaction," *AIAA Journal*, Vol. 24, No. 10, 1986, pp. 1569–1576.

[27] Baeder, J. D., *The Computation and Analysis of Acoustic Waves in Transonic Airfoil-Vortex Interactions*, Ph.D. thesis, Stanford University, Stanford, CA, 1989.

[28] Srinivasan, G. and McCroskey, W., "Euler Calculations of Unsteady Interaction of Advancing Rotor with a Line Vortex," *AIAA Journal*, Vol. 31, No. 9, 1993, pp. 1659–1666.

[29] Morvant, R., *The Investigation of Blade-Vortex Interaction Noise using Computational Fluid Dynamics*, Ph.D. thesis, University of Glasgow, Glasgow, Scotland, February 2004.

[30] Morvant, R., Badcock, K., Barakos, G., and Richards, B., "Aerofoil-Vortex Interaction Simulation using the compressible vorticity confinement method," *AIAA Journal*, Vol. 43, No. 1, 2005, pp. 63–75.

[31] Dindar, M., Shepard, M., Flaherty, J., and Jansen, K., "Adaptive CFD analysis for rotorcraft aerodynamics," *Computer Methods in Applied Mechanics and Engineering*, Vol. 189, No. 4, 2000, pp. 1055–1076.

[32] Oh, W., Kim, J., and Kwon, O., "Numerical Simulation of Two-Dimensional BladeVortex Interactions Using Unstructured Adaptive Meshes," *AIAA Journal*, Vol. 40, No. 3, 2002, pp. 474–480.

[33] Lim, J., Nygaard, T., Strawn, R., and Potsdam, M., "BVI Airloads Prediction Using CFD/CSD Loose Coupling," *Proceedings of the American Helicopter Society Annual Forum, Vertical Lift Design Conference*, San Francisco, CA, 2006.

[34] Lim, J. and Strawn, R., "Computational Modeling of HART II Blade-Vortex Interaction Loading and Wake System," *Journal of Aircraft*, Vol. 45, No. 3, 2008, pp. 923–933.

[35] Kelly, M., *Predicting High Frequency Airloads and Acoustics assosiated with Blade-Vortex Interaction*, Ph.D. thesis, University of Glasgow, Glasgow, Scotland, 2010.

[36] Jha, A., "Rolls-Royce Brings Propeller Engines Back in Vogue," *The Guardian*, October 2008.

[37] Butterworth-Hayes, P., "Open Rotor Research Revs Up," *Aerospace America*, March 2010, pp. 38–52.

[38] Jameson, A., "Analysis of Wing Slipstream Flow Interactions," Tech. rep., NASA, 1969.

[39] Miranda, L. and Brennan, J., "Aerodynamic Effects of Wingtip-Mounted Propellers and Turbines," *AIAA Applied Aerodynamics Conference*, San Diego, CA, June 1986.

[40] Cho, J. and Cho, J., "Quasi-Steady Aerodynamic Analysis of PropellerWing Interaction," *International Journal for Numerical Methods in Fluids*, Vol. 30, No. 8, 1999, pp. 1027–1042.

[41] Lötstedt, P., "Accuracy of a Propeller Model in inviscid Flow," *Journal of Aircraft*, Vol. 32, No. 6, 1995, pp. 1312–1321.

[42] Stuermer, A., "Unsteady Euler and Navier-Stokes Simulations of Propellers with the Unstructured DLR TAU-Code," *New Results in Numerical and Experimental Fluid Mechanics*, Vol. 5, 2006, pp. 145–151.

[43] Roosenboom, E., Strmer, A., and Schrder, A., "Advanced Experimental and Numerical Validation and Analysis of Propeller Slipstream Flows," *Journal of Aircraft*, Vol. 47, No. 1, JanuaryFebruary 2010, pp. 284–291.

[44] Samuelsson, I., "Low speed propeller slipstream aerodynamic effects, AGARD, A Selection of Experimental Test Cases for the Validation of CFD Codes, Volume 2," Tech. rep., Aeronautical Research Inst. of Sweden, Bromma. Flygtekniska Foersoeksanstalten, 1994.

[45] Samuelsson, I., "Low speed wind tunnel investigation of propeller slipstream aerodynamic effects on different nacelle/wing combinations. Part 1," Tech. rep., Aeronautical Research Inst. of Sweden, Stockholm. Aerodynamics Dept., 1987.

[46] Samuelsson, I., "Low speed wind tunnel investigation of propeller slipstream aerodynamic effects on different nacelle/wing combinations. Part 2," Tech. rep., Aeronautical Research Inst. of Sweden, Stockholm. Dept. of Aerodynamics., 1990.

[47] Kroo, I., "Propeller-Wing Integration for Minimum Induced Loss," *Journal of Aircraft*, Vol. 23, No. 7, July 1986, pp. 561–565.

[48] Veldhuis, L. L. M. and Heyma, P. M., "Aerodynamic Optimisation of Wings in Multi-Engined Tractor Propeller Arrangements," *Aircraft Design*, Vol. 3, No. 3, 2000, pp. 129–149.

[49] Chiocchia, G. and Pignataro, S., "On the induced drag reduction due to propeller-wing interaction," *Aeronautical Journal*, Vol. 99, No. 988, October 1995, pp. 328–336.

[50] Duraisamy, K., *Studies in Tip Vortex Formation, Evolution and Control*, Ph.D. thesis, University of Maryland, College Park, MD, February 2005.

[51] Duraisamy, K., Ramasamy, M., Baeder, J., and Leishman, G., "High Resolution Computational and Experimental Study of Hovering Rotor Tip Vortex Formation," *AIAA Journal*, Vol. 45, No. 11, 2007, pp. 2593–2602.

[52] Duraisamy, K. and Baeder, J., "High Resolution Wake Capturing Methodology for Hovering Rotors," *Journal of the American Helicopter Society*, Vol. 52, No. 2, 2007, pp. 110–122.

[53] Duraisamy, K. and Brown, R., "Aerodynamic Response of a Hovering Rotor to Ramp Changes in Pitch Input," *Proceedings of the American Helicopter Society 64th Annual Forum*, Montreal, Canada, 2008.

[54] Vinokur, M., "An analysis of finite-difference and finite-volume formulations of conservation laws," *Journal of Computational Physics*, Vol. 81, No. 1, 1989, pp. 1–52.

[55] Ilie, M., "Numerical study of helicopter blade-vortex mechanism of interaction using large-eddy simulation," *Computers and Structures*, Vol. 87, No. 11–12, 2009, pp. 758–768.

[56] Leer, B. V., "Towards the ultimate conservative difference scheme. V. A second-order sequel to Godunov's method," *Journal of Computational Physics*, Vol. 32, 1979, pp. 101–136.

[57] Roe, P., "Approximate Riemann Solvers, Parameter Vectors and Difference Schemes," *Journal of Computational Physics*, Vol. 43, No. 2, 1981, pp. 357–372.

[58] Toro, E. F., *Riemann Solvers and Numerical Methods for Fluid Dynamics: A Practical Introduction*, Springer-Verlag, 1997.

[59] Shu, C.-W., "Essentially Non-Oscillatory and Weighted Essentially Non-Oscillatory Schemes for Hyperbolic Conservation Laws," *Lecture Notes in Mathematics*, Vol. 1697, 1998, pp. 325–432.

[60] Jiang, G. and Shu, C.-W., "Efficient implementation of weighted ENO schemes," *Journal of Computational Physics*, Vol. 126, No. 1, 1996, pp. 202–228.

[61] Harten, A., Engquist, B., Osher, S., and Chakravarthy, S., "Uniformly high order acurate essentially non-oscillatory schemes, III," *Journal of Computational Physics*, Vol. 131, No. 2, 1987, pp. 3–47.

[62] Shu, C.-W. and Osher, S., "Efficient implementation of essentially non-oscillatory shock capturing schemes," *Journal of Computational Physics*, Vol. 77, No. 2, 1988, pp. 439–471.

[63] Hirsch, C., *Numerical Computation of Internal and External Flows, Volume 2, Computational Methods for Inviscid and Viscous Flows*, Wiley Publishers, 1990.

[64] Pulliam, T., "Time Accuracy and the use of Implicit Methods," *11th AIAA Computational Fluid Dynamics Conference*, Orlando, FL, 1993.

[65] Jameson, A., "Time Dependent Calculations Using Multigrid, with Applications to Unsteady Flows Past Airfoils and Wings," *AIAA Paper 91-1596*, 1991.

[66] Melson, N. D., Sanetrik, M. D., and Atkins, H. L., "Time-accurate Navier-Stokes calculations with multigrid acceleration," *11th AIAA Computational Fluid Dynamics Conference*, Orlando, FL, July 1993.

[67] Rumsey, C., Sanetrik, M., Biedron, R., Melson, N., and Parlette, E., "Efficiency and accuracy of time-accurate turbulent Navier-Stokes computations," *Computers and Fluids*, Vol. 25, No. 2, 1996, pp. 217–236.

[68] Yoon, S. and Jameson, A., "Lower-Upper Symmetric-Gauss-Seidel Method for the Euler and Navier-Stokes Equations," *AIAA Journal*, Vol. 26, No. 9, 1988, pp. 1025–1026.

[69] Steger, J., Dougherty, F., and Benek, J., "A Chimera Grid Scheme," *Advances in Grid Generation*, Vol. 5, 1983, pp. 59–69.

[70] Benek, J., Steger, J., Dougherty, F., and Buning, P., "Chimera: A grid-embedding technique," Tech. Rep. NASA-TM-89246, NASA Ames Research Center, Moffett Field, CA., 1986.

[71] Lighthill, M., "On Sound Generated Aerodynamically I; General Theory," *Proceedings of The Royal Society*, Vol. 211, No. 1107, March 1952, pp. 564–587.

[72] Ffowcs Williams, J. and Hawkings, D., "Sound Generation by Turbulence and Surfaces in Arbitrary Motion," *Philosophical Transactions of the Royal Society of London*, Vol. 264, 1969, pp. 321–342.

[73] Hawkings, D. and Lowson, M., "Theory of open supersonic rotor noise," *Journal of Sound and Vibration*, Vol. 36, No. 1, 1974, pp. 1–20.

[74] Farassat, F. and Succi, G. P., "The Prediction of Helicopter Rotor Discrete Frequency Noise," *Vertica*, Vol. 7, No. 4, 1982, pp. 309–320.

[75] Farassat, F. and Succi, G. P., "A review of propeller discrete frequency noise prediction technology with emphasis on two current methods for time domain calculations," *Journal of Sound and Vibration*, Vol. 71, No. 3, 1980, pp. 399–419.

[76] Schmitz, F., "Aeroacoustics of Flight Vehicles: Theory and Practice, Volume 1: Noise Sources," Tech. Rep. 90-3052, NASA, August 1991.

[77] Singh, R., *Transonic Effects on Aerodynamics and Acoustics of Blade-Vortex Interaction*, Ph.D. thesis, University of Maryland, College Park, MD, 1999.

[78] Caradonna, F., Kitaplioglu, C., McCluer, M., Baeder, J., Leishman, J. G., Berezin, C., Visintainer, J., Bridgeman, J., Burley, C., Epstein, R., Lyrintzis, A., Koutsavdis, E., Rahier, G., Delrieux, Y., Rule, J., and Bliss, D., "Methods for the Prediction of BladeVortex Interaction Noise," *Journal of the American Helicopter Society*, Vol. 45, No. 4, October 2000, pp. 303–317.

[79] Bailey, S. and Tavoularis, S., "Measurements of the Velocity Field of a Wing-Tip Vortex, Wandering in Grid Turbulence," *Journal of Fluid Mechanics*, Vol. 601, 2007, pp. 281–315.

[80] Lamb, H., *Hydrodynamics*, Cambridge University Press,, 1932.

[81] Squire, H., "The Growth of a Vortex in Turbulent Flow," *Aeronautical Quarterly*, Vol. 16, 1965.

[82] Ramasamy, M. and Leishman, J., "A Generalized Model for Transitional Blade Tip Vortices," *Journal of the American Helicopter Society*, Vol. 51, No. 1, 2006, pp. 92–103.

[83] Kitaplioglu, C., Caradonna, F., and Burley, C., "Parallel Blade-Vortex Interactions: An Experimental Study and Comparisons With Computations," *Journal of the American Helicopter Society*, Vol. 42, 1997, pp. 272–281.

[84] Singh, R. and Baeder, J., "Generalized moving gust response using CFD with application to airfoil-vortex interaction," *AIAA Applied Aerodynamics Conference*, Atlanta, GA, June 1997.

[85] Batchelor, G., "Axial Flow in Trailing Line Vortices," *Journal of Fluid Mechanics*, Vol. 20, 1964, pp. 645–658.

[86] Spalart, P., "Airplane Trailing Vortices," *Annual Review of Fluid Mechanics*, Vol. 30, No. 1, 1998, pp. 107–138.

[87] Anderson, E. and Lawton, T., "Correlation Between Vortex Strength and Axial Velocity in a Trailing Vortex," *Journal of Aircraft*, Vol. 40, No. 4, 2003, pp. 699–704.

[88] Johnston, R. and Sullivan, J., "Unsteady Wing Surface Pressures in the Wake of a Propeller," *Journal of Aircraft*, Vol. 30, No. 5, 1993, pp. 644–651.

[89] Marshall, J., "Vortex Cutting by a Blade, Part 1: General Theory and a Simple Solution," *AIAA Journal*, Vol. 32, No. 6, 1994, pp. 1145–1150.

[90] Marshall, J. and Yalamanchili, R., "Vortex Cutting by a Blade. Part II: Computations of Vortex Response," *AIAA Journal*, Vol. 32, No. 7, 1994, pp. 1428–1436.

[91] Veldhuis, L. L. M. and Nebiolo, S., "A Propeller-Integration Study Comparing Experimental Data with Numerical Flow Solutions Based on the Navier-Stokes Equations," *International Congress of Aeronautical Sciences*, Harrogate, United Kingdom, August 2000.

[92] Farassat, F., Padula, S., and Dunn, M., "Advanced turboprop noise prediction based on recent theoretical results," *Journal of Sound and Vibration*, Vol. 119, No. 1, 1987, pp. 53–79.

[93] Adams, B., Bohnhoff, W., Dalbey, K., Eddy, J., Eldred, M., Gay, D., Haskell, K., Hough, P., and Swiler, L., "DAKOTA, A Multilevel Parallel Object-Oriented Framework for Design Optimization, Parameter Estimation, Uncertainty Quantification, and Sensitivity Analysis: Version 5.0 User's Manual," Tech. Rep. SAND2010-2184, Sandia, December 2010.

[94] Veldhuis, L., "Optimization of Tractor PropellerWing Configurations," *Proceedings of the Institution of Mechanical Engineers, Part G: Journal of Aerospace Engineering*, Vol. 209, 1995, pp. 215–226.

[95] Miley, S. J., Howard, R. M., and Holmes, B. J., "Wing laminar boundary layer in the presence of a propeller slipstream," *Journal of Aircraft*, Vol. 25, 1988, pp. 606–611.

[96] LeVeque, R., "High-Resolution Conservative Algorithms for Advection in Incompressible Flow," *SIAM Journal on Numerical Analysis*, Vol. 33, No. 2, 1996, pp. 627–665.